SLAC-PUB-71
January 1965

DESIGN AND FABRICATION OF THE ACCELERATING STRUCTURE FOR THE STANFORD TWO-MILE ACCELERATOR*

R. P. Borghi, A. L. Eldredge, G. A. Loew and R. B. Neal

(To be published in Advances in Microwaves)

*Work supported by U. S. Atomic Energy Commission

I. INTRODUCTION

A. Historical Review

In April, 1957, Stanford University proposed the construction of an electron linear accelerator approximately two miles long designed to produce an electron beam of high intensity in the energy range from 10 to 40 BeV for purposes of particle-physics research. This accelerator was authorized in September, 1961 and is now being constructed on a site on Stanford land. Stanford is carrying out this work under a prime contract with the U. S. Atomic Energy Commission. The estimated total construction cost of this accelerator is $114 million, and the construction schedule calls for completion by July 1, 1966.

The purpose of this article is to discuss the design and fabrication of one of the principal components of the two-mile accelerator, the disk-loaded waveguide which serves as the accelerating structure.

The design of the two-mile accelerator is a logical extension of the accelerator development that began at Stanford University in 1947.(1) Up to the present date, the largest of the Stanford accelerators is the 300-foot-long Mark III.(2) The Mark III is a 30-section machine which has been producing high-energy electrons for physics research since 1952. The Stanford Mark IV accelerator was a two-section machine powered by two klystron amplifiers. The Mark IV was used from 1955 to 1964, primarily as a vehicle for development and testing of accelerator components. In December 1963, the Mark III was rebuilt. Its 30 constant-impedance accelerating sections were replaced by 30 constant-gradient sections fabricated at the Stanford Linear Accelerator Center. This modification

resulted in an increase in energy capability in the Mark III from 1 BeV to approximately 1.2 BeV.

B. General Description

Before discussing the detailed design of the accelerating structure, it may be helpful to give a brief general description of the two-mile accelerator. A general view of the accelerator and target area is shown in Fig. 1.

The accelerator and its related equipment will be situated in two parallel housings. The accelerator proper will be located in an underground concrete housing, 11-feet wide and 10-feet high. The klystrons, modulators, vacuum pumps, and other auxiliary equipment will be located in an above-ground gallery, 30-feet wide and 16-feet high. The accelerator housing can be entered only when the electron beam is turned off, but the klystron gallery can be continuously occupied. The two housings will be separated by 25 feet of earth which will serve as radiation shielding. There will be a 27-inch-diameter transverse pipe between the housings every 20 feet, each containing one connecting waveguide and other utilities.

The accelerator proper will consist of a disk-loaded cylindrical waveguide supplied with microwave power at a frequency of 2856 Mc/sec. The accelerator will be made in sections approximately ten-feet long, and each of these sections will be independently fed with power through a suitable S-band waveguide and waveguide-to-accelerator coupler. A total of 960 ten-foot sections will comprise the entire accelerator.

The accelerator will be supplied with power by 240 klystron amplifiers, each capable of producing up to 24 megawatts of peak power at 360 pulses per second and 2.5 microseconds pulse length. The power output from each klystron will be divided four ways and will be used to supply power to four successive ten-foot sections, as shown in Fig. 2. With this initial complement of tubes, each operating at the conservative level of 6 megawatts, the accelerator will be able to supply an average electron current of 15 microamperes at an energy of 10 BeV. The energy can be increased to 20 BeV and the current to 30 microamperes by increasing the power output from each klystron to 24 megawatts. Operation with this complement of 240 tubes is referred to as Stage I, the operation called for under present authorization.

Provisions have been made to permit later increase in the number of tubes connected to the accelerator to a maximum of 960, in which case each klystron will feed a single 10-foot accelerator section. This condition of operation is referred to as Stage II. With 960 klystrons each producing 24 megawatts of peak power, an electron energy of about 40 BeV should be obtained.

II. SELECTION OF CHARACTERISTIC PARAMETERS

A. Choice of Operating Frequency

Since almost all of the basic accelerator parameters have frequency dependence, it is first essential to study the implications of using the various frequency bands and to choose an operating frequency. It is not possible to make the choice of frequency by purely analytical methods; the final selection requires the application of engineering judgment and reference to previous experience.

As a guide to the choice of frequency, the frequency dependence of the principal machine parameters is listed in Table I. This table is based upon direct scaling of the modular dimensions of the accelerating structure. This assumption has been adopted to simplify the comparison. In a practical accelerator it is likely that certain compromises would be advisable which would change Table I in certain details but not in its general implications.

The energy of electrons from a linear accelerator with negligible beam loading is given by

$$V = K \left(P_T L r_o\right)^{\frac{1}{2}} \tag{1}$$

where P_T is the total input rf power, L is the total length, r_o is the shunt impedance per unit length, and K is a constant whose value depends upon the net rf attenuation in each independently fed accelerator section. Since r_o varies as $f^{\frac{1}{2}}$, the rf power required to produce a given final energy in a fixed length is proportional to $f^{-\frac{1}{2}}$. Thus, considerations of power economy indicate that the operating frequency should be as high as possible. Other advantages of the higher frequencies are the reduced filling time, which varies as $f^{-\frac{3}{2}}$, and reduced energy storage, which varies as f^{-2}. A shorter filling time is advantageous since electrons can be accelerated during a larger fraction of the available rf pulse length. The use of the higher frequencies also results in greater maximum field strength (as limited by breakdown) and larger relative frequency and dimensional tolerances.

From Table I it can be seen that the maximum frequency which can be used is limited by the available aperture for the beam and the reduced beam-current capability. Another factor against the use of very high frequencies is the increased number of power sources and feeds required. The increased cost required for the additional rf systems, modulators, and controls, and the increased operational difficulties tend to reduce the advantages arising from the decreased power consumption at higher frequencies.

An important consideration not taken into account in Table I is the degree of conservatism involved in the choice of frequency band. While linear electron accelerators have been constructed and operated at L-, S-, and X-bands, the largest amount of experience is available at S-band. In fact, to this date all accelerators of this type having energies above 100 MeV have operated at S-band.

To illustrate the scaling laws given in Table I more specifically, design data for a 10-BeV accelerator 10,000 feet long are given in Table II. Three cases are tabulated corresponding to operating at L-, S-, and X-bands. The specific values in Table II are based on relations and criteria which are developed later in this section. We shall not comment individually upon each item in Table II, but it may be worthwhile to emphasize the following features:

(a) An important aspect of the design of the two-mile accelerator is the possibility at some suitable future date of increasing the beam energy from the initial range of 10 to 20 BeV to the higher range of 20 to 40 BeV. For reasons of economy, and to avoid prolonged machine shutdown, it is desirable to accomplish the energy expansion by increasing

the rf power rather than by increasing the accelerator length. According to Table II, the L-band structure with a fixed length of 10,000 feet cannot be expanded above about 38.4 BeV without experiencing breakdown difficulties.

(b) The average rf power requirements are in the ratio 4.1:1.0:0.4 for the L-, S-, and X-band machines, respectively.

(c) The maximum peak beam currents and beam powers are in the ratios of 1.7:1.0:0.6 for the L-, S-, and X-band machines, respectively.

(d) The aperture available for the beam in the X-band machine (0.255 inch) is small enough to cause concern about beam transmission, accelerator alignment, etc.

(e) The X-band accelerator ranks highest in terms of maximum expanded energy capability, but the higher energies require X-band sources of higher peak power than are presently available. For example, operation at 40 BeV would require 4988 sources each producing 2.5 megawatts of peak rf power.

(f) Expansion of the L-band accelerator to 40 BeV would require that each of the 185 feed points be supplied with 200 megawatts of peak power. This is much higher than the power output obtained from a single L-band source to date and could thus require parallel operation of sources at each feed.

(g) Expansion of the S-band machine to 40-BeV would require 22.2 megawatts at each of the 960 feed points. Power outputs above this level have already been obtained from single S-band sources.

(h) The relative frequency and dimensional tolerances favor the use of the higher frequencies. Relative tolerances are probably more

significant than absolute tolerances, since the former are a better measure of the difficulties involved in designing stable frequency sources and in critical machining operations.

(i) The average power dissipated per unit area of accelerator surface is not significantly different in the three designs because the increased wall area at low frequency tends to compensate for the higher power required, and vice versa. However, the average temperature difference across the accelerator wall, which is a measure of the degree of detuning of the structure, is highest at L-band and lowest at X-band.

It would be possible to compare accelerator designs at the various frequencies in further detail. The designs we have chosen for illustrative purposes were based upon direct scaling of the modular dimensions of the present S-band accelerator structure. An improved design at a particular frequency from the standpoint of over-all economy or performance might result from deviating from the scaling laws we have used. For example, the L-band design might be improved by decreasing the feed interval and using a larger number of sources, and by increasing the rf and beam pulse lengths while decreasing the pulse repetition rate. However, this would not affect the total peak power requirement or the maximum field-strength capability. Similar alterations might be made at S- and X-bands to improve certain characteristics of these designs. However, we do not believe that such changes would appreciably modify the general conclusion we have reached: the S-band accelerator is the optimum choice for the two-mile accelerator for reasons which are implicit in the scaling laws of Table I and the illustrative examples of Table II.

B. Product of RF Power and Accelerator Length

The energy of electrons from a linear accelerator with negligible beam-loading was given by Eq. (1). To estimate the power-length product of the two-mile accelerator, we take r_o = 53 megohms/meter; moreover, we anticipate the results of Section II.H below and use the value, K = 0.82. The minimum objective is an accelerator which will produce electrons having an energy of 10 BeV under conditions of 10 percent beam loading. The no-load energy must therefore be 11.11 BeV. To obtain a realistic estimate, we assume that 10 percent of the rf power is dissipated in the rf transmission lines between the power sources and the accelerator, and further that 5.2 percent of the accelerator length is used for auxiliary in-line devices and does not contribute to the acceleration process.

Substituting the above assumptions into Eq. (1) we obtain

$$P_T L = 4.06 \times 10^{14} \text{ watt-cm}$$

$$= 1.33 \times 10^{7} \text{ Mw-ft}$$

Thus the product of the total rf power and the accelerator length must be 1.33×10^7 Mw-ft in order to obtain an electron-beam energy of 10 BeV with 10 percent beam loading.

C. Selection of Accelerator Length

Once the rf-power accelerator-length product has been determined, these two quantities must be determined individually. The following factors influence these selections:

1. Maximum Electric Gradient

As discussed in Section I, the design objective is a linear electron accelerator initially capable of producing energies of 10 BeV, with an ultimate capability of 40 BeV energy by addition of rf power without increase of accelerator length. This objective requires that the length of the machine must be chosen so as to permit the maximum ultimate gradient. The maximum average electric gradient obtained in an operating S-band linear accelerator to date is approximately 4.5 MeV/ft. Using this figure, we find that a length of approximately 10,000 feet is required to satisfy the ultimate energy objective.

2. Ecomonic Considerations

The total cost of the accelerator program may be divided into three parts:

(a) costs (C_P) which are proportional to the total connected rf power;

(b) costs (C_L) which are proportional to the total accelerator length; and

(c) fixed costs (C_F) which include research costs and administrative costs, among others.

To be meaningful, these costs must be based on a time period that includes the construction time plus a period judged to represent the useful life of the machine. We have used a period of 10 years of useful life in cost studies. From the fact that rf power and accelerator length have equal weight in the equation for electron energy, it is easy to show that the greatest over-all economy results when $C_P = C_L$. Otherwise, the total cost is given by

$$C = \frac{1}{2}\left[\left(\frac{C_P}{C_L}\right)^{\frac{1}{2}} + \left(\frac{C_L}{C_P}\right)^{\frac{1}{2}}\right] C_{(P,L)_{min}} + C_F \qquad (2)$$

where $C_{(P,L)_{min}}$ is the minimum value of $C_P + C_L$ (i.e., where $C_P = C_L$). Our cost studies have shown that an accelerator length of 10,000 feet is very close to the optimum value to minimize the total project costs over the 6-year construction period and a 10-year period of operation.

3. Land Availability

There were several potential sites available on Stanford land which seemed suitable for the accelerator project location. An accelerator length of 10,000 feet (plus another 2500 feet, approximately, for research facilities) was possible at most of these sites but no greater length was available without expensive land-acquisition costs.

Thus the choice of an accelerator length of 10,000 feet satisfies the several conditions discussed above, viz., it permits operation at the ultimate expanded energy-gradient; it is near optimum from the standpoint of over-all economy; and such space is available on Stanford property. Therefore, we have made the selection

$$L = 10{,}000 \text{ feet}$$

which, using the power-length product determined in Section II.B leads to the following initial total connected rf power requirement

$$P_T = 1.33 \times 10^3 \text{ Mw}$$

It should be emphasized that this value of P_T is based upon a particular choice of operating mode ($2\pi/3$) and upon a particular attenuation parameter ($\tau = 0.57$). Their selection is discussed later in this section. The value of P_T would vary slightly if another mode or another value of τ were used.

D. Selection of Number of RF Power Sources and Feed Interval

It was established in Section II.C that a total rf peak power of 1330 megawatts must be supplied to a 10,000-foot accelerator in order to achieve an electron energy of 10 BeV with 10 percent beam loading. The next logical design decisions are the determination of the number of individual rf power sources and the spacing of the rf feeds along the accelerator length.

In general, it is more economical to obtain a large amount of microwave energy from a small number of high-power sources than from a large number of low-power sources. The basic reason for this fact is that the cost of a power source depends more strongly on the number and kind of operations involved in its fabrication and processing than upon its physical size and output rating. The cost of employment of the power sources in the accelerator system in terms of auxiliary equipment, instrumentation, controls, waveguide equipment, etc., also decreases as the total number of individual sources is reduced. Based upon laboratory and commercial experience with high-power klystron amplifiers, it seems reasonable to expect that S-band tubes can be constructed to have an average life of 2000 hours or more while producing 24 megawatts of peak rf power and 22 kilowatts of average rf power. Much higher peak power levels from single S-band tubes do not appear to be readily obtainable at this time. An electron beam energy of 10 BeV will be obtained by requiring only 6 megawatts of peak output per klystron. At this power level, average lifetimes exceeding 2000 hours should be easily achieved. For a total rf power of 1330 megawatts, 240 klystrons producing 6 megawatts each will be sufficient. Since these tubes will have a capability of 24

megawatts each, it will be possible to achieve electron energies up to 20 BeV with the initial complement of tubes. For operation at the Stage II level of 40 BeV, 960 tubes producing 24 megawatts each will be required.

We shall now discuss the selection of the feed spacing along the accelerator length. The limiting cases of feed spacing are (a) a single feed for the entire accelerator, and (b) individual feeds for each of the approximately 80,000 individual accelerator cavities. The first extreme is obviously infeasible because the full rf power could not be transmitted through the accelerator structure. The second extreme would be prohibitively expensive because of the multiplicity of waveguides and other microwave components and the necessary controls and instrumentation. As described in Section II.H, there is an optimum, or at least a preferred value, of the net rf attenuation between feed points. The choice of attenuation parameter is a compromise among many factors. The attenuation parameter can be adjusted to the desired value by properly choosing the diameter of the aperture in the disk-loaded accelerator structure and the length of the accelerator section. Increasing the aperture size increases the group velocity and decreases the attenuation per unit length. Thus a given attenuation parameter can be obtained by either a short accelerator section of high unit attenuation (small aperture), or by a long section of low unit attenuation (large aperture), or by a compromise involving medium length and medium aperture. The main factor in favor of close feed-spacing is that the shunt impedance r_o of the accelerator structure improves slowly as the group velocity is decreased. This is shown in Fig. 3 which applies specifically to the $2\pi/3$ mode, but the same general behavior is true for other modes.

Several considerations limit how closely the feeds should be spaced. These limiting considerations are as follows:

(a) Increased costs because of the larger number of components, controls, waveguides, couplers, rf loads, instruments, etc.

(b) The complexity of splitting the rf power from each source many times.

(c) The decreased aperture available for the electron beam as the group velocity is decreased.

(d) Increased operational difficulties because of the increased number of phasing adjustments, monitors, interlocks, etc.

In Stage I, 240 rf power sources supplying 6 to 24 megawatts each will be used, as noted above. With equal spacing, these sources will be located at 40-foot intervals along the accelerator length. In Stage II (40 BeV maximum), with 960 rf sources each supplying 6 to 24 megawatts, it would not be safe (for reasons of rf breakdown) to feed the combined power outputs of two or more tubes into an accelerator section. Therefore, at least one feed every 40 feet is required in Stage I and at least one feed every 10 feet in Stage II. However, the shunt impedance is reduced by about 15 percent in going from a 10-foot to a 40-foot feed interval, so that the electron energy would be about 7.5 percent less for the same total rf power input.

For reasons discussed in the previous paragraph, a feed interval of 10 feet has been chosen for the two-mile accelerator. This means that during Stage I operation, with 240 rf-power sources, the power output from each klystron must be divided four ways so as to supply four successive accelerator feeds. The modular arrangement of klystrons, waveguides, and accelerator sections in Stage I is shown in Fig. 2. With

this arrangement, the number of klystrons can readily be increased to 480. However, to convert to Stage II operation with 960 rf sources, it will be necessary to double the number of connecting waveguides shown in the figure. The number of required feeds remains unchanged.

E. Choice of RF Pulse Length and Repetition Rate

For physics-research purposes it is generally desirable to have the electron-beam duty cycle (which is defined as the product of pulse repetition rate and beam pulse length) as high as possible. The practical upper limit of duty cycle is determined by economic considerations. The rf duty cycle must be greater than the beam duty cycle because a certain time is required to fill the accelerator with rf energy prior to injection of the beam. For the case where the electron beam is injected at a time after the start of the rf pulse equal to one filling time, the ratio of beam-to-rf duty cycles is given by

$$\frac{D_b}{D_{rf}} = 1 - \frac{t_F}{t_{rf}} \tag{3}$$

where t_F is the accelerator filling time, and t_{rf} is the rf pulse length. For example, with $t_F = 0.83$ μsec (the value for $\tau = 0.57$ with the $2\pi/3$ mode) and $t_{rf} = 2.5$ μsec, the maximum duty cycle ratio as given by Eq. (3) is 0.67. This may be compared with the value of 0.5 for the original one-BeV Stanford Mark III accelerator (see Section I.A). An important point to emphasize is that a given fractional change in rf duty cycle because of increasing rf pulse length permits an even larger fractional increase in the beam duty cycle. Thus increasing the rf pulse

length from 2.0 to 2.5 microseconds, an increase of 25 percent, allows a 43 percent increase in the beam duty cycle (for $t_F = 0.83$ μsec). The factors which place a practical limit on the maximum rf pulse length are the increasing costs of modulator components, such as the pulse transformers and the pulse-forming networks. On the basis of these considerations, we have adopted the value of 2.5 microseconds for the rf pulse length of the two-mile accelerator.

The maximum value of the pulse repetition rate is governed by three primary factors:

(a) The initial cost of power components increases with increasing pulse repetition rate because of their higher average power ratings.

(b) It is more difficult and expensive to design and construct high-power modulators at the higher repetition rates.

(c) The ac power operational costs for the accelerator power sources increase almost directly with pulse repetition rate.

A maximum repetition rate of 360 pulses per second has been adopted for the two-mile accelerator. This may be compared with the maximum rate of 60 pulses per second for the Stanford Mark III accelerator. The combination of higher repetition rate, longer rf pulse length, and shorter filling time allows a maximum beam duty cycle for the two-mile accelerator of about 0.0006, or about 10 times greater than that of the Mark III accelerator.

F. Selection of Operating Mode

The accelerator structure is a disk-loaded cylindrical waveguide of the form shown in Figs. 4(a) and 4(b). (The alternative configurations in Fig. 4(c) are discussed in Section III.B below.) The efficiency of the structure as an accelerator of electrons is measured by a quantity called the shunt impedance per unit length. This quantity, which we have already introduced in the previous discussion and designated by the symbol r_o, may be defined as the square of the energy gained (in electron volts) by an electron per unit length of accelerator structure for unit rf power dissipation in this same length. We have defined shunt impedance in terms of gain in particle energy to emphasize that it is not simply the magnitude of the electric field in the accelerator structure which determines the electron energy gain per unit length; rather, it is the amplitude of the Fourier component of the axial field which travels at the electron velocity. The fundamental component is commonly used for acceleration of electrons.

The exact value of shunt impedance for a particular configuration of accelerator structure cannot be represented in simple form but can be measured to good accuracy by microwave techniques. An approximate equation for r_o which is suitable for studying the effects of varying the cavity dimensions is

$$r_o = 968 \left(\frac{\beta_w}{\delta}\right) \frac{(1 - \eta)^2}{n + 2.61\, \beta_w (1 - \eta)} \left(\frac{\sin D/2}{D/2}\right)^2 \qquad (4)$$

where

β_w is the phase velocity in the structure divided by c,

δ is the skin depth,

η is the fraction of the length of the structure which is occupied by disks, i.e., $\eta = t/d = tn/\lambda$,

n is the number of disks per guide wavelength, and

D is the transit time in radians required for the electron to pass through the cavity gap, i.e., $D = (2\pi/n)(1-\eta)$.

Equation (4) can be derived by considering an array of simple "pill-box" cavities. This equation gives too high a value of r_o for two reasons: (a) the conductivity of the copper walls is never as high as the idealized value used in calculating the numerical value (968) in the equation; (b) no account is taken of the effect of the disk apertures. Nevertheless, the relative variation of r_o with the spacing and thickness of the disks given by Eq. (4) has been confirmed by experimental measurements.

A graph of r_o versus n for f = 2856 Mc/sec based on Eq. (4) is shown in Fig. 5 for four values of disk thickness, t. Corresponding experimental values obtained from test cavity measurements are also shown. From Fig. 5 it is possible to draw some general conclusions. For negligible disk thicknesses ($t \approx 0$), the optimum number of disks per wavelength is approximately 3.5. As the disk thickness is increased, the optimum value of n decreases. The best value at t = 0.120 inch is about n = 3. It is about 2.7 for t = 0.230 inch, which is the chosen disk thickness. The value n = 3, corresponding to a phase shift of $2\pi/3$ radians per cavity, has been adopted for the two-mile accelerator.

In addition to the improvement in shunt impedance, the selection of the $2\pi/3$ mode results in fewer disks and improved vacuum conductance compared to the $\pi/2$ mode used with the earlier Stanford structures.

The basis for the results described above may be found upon further examination of Eq. (4). There are three competing factors:

(a) The shunt impedance of the individual cavities is improved by increasing the height of the cavities, i.e., the disk spacing.

(b) The fraction of the length available for the accelerating fields to act on the electrons is increased as the number of disks per wavelength is decreased or as the disk thickness is decreased.

(c) As the disk spacing is decreased, the electron transit time is decreased correspondingly, and the average or "effective" field strength acting on the electron is increased as $(\sin D/2)/(D/2)$. Thus, considerations (a) and (b) favor small n and small t, while consideration (c) favors large n and large t. As t increases, the fractional space occupied by the disks increases so that r_o peaks at a lower value of n.

An expression similar to Eq. (4) may be given for the Q of an accelerator structure:

$$\frac{Q\delta}{\lambda_o} = \frac{\beta_w(1-\eta)}{n + 2.61\,\beta_w\,(1-\eta)} \qquad (5)$$

where the symbols have the same meaning as before. A plot of Q versus n is given in Fig. 6. Some measured values of Q are also shown in the same figure.

The quantity Q was measured in each case by taking two cavity lengths in the ratio of 2:1 in order to cancel out the effect of the end-wall losses as shown in Section III.E.6 below. The values of Q are seen to decrease from around 17,000 at $n = 2$ to about 13,000 at $n = 3$ and 10,000 at $n = 4$.

A number of experimental curves for $n = 2$, 3, and 4 are given in Figs. 7 and 8. The data for these curves were based on disks with unrounded or "square" boundaries. For a given aperture diameter, rounding of the boundary has the effect of increasing the group velocity and decreasing the shunt impedance by about 5 to 10 percent.

Another observation, which is illustrated in Fig. 8, is that the group velocity decreases with increasing disk thickness at a given value of n (except $n = 2$). This indicates that it may be quite misleading to compare the various cases on the basis of the same aperture diameter ($2a$). A better comparison might be made on the basis of the same value of group velocity, which would thereby insure that the filling times for an accelerator section of fixed length were equal in all cases. Alternately, the comparison might be made on the basis of equal values of the product $v_g Q$, which would give equal values of rf attenuation per unit length in all cases. Adjusting $2a$ to give equal values of v_g would reduce r_o more severely in the thick-disk cases and would thus favor the adoption of thin disks. The limiting factor in reducing disk thickness is the increasing danger of arcing at the disk aperture boundary.

G. Constant-Impedance vs Constant-Gradient Structures

When an accelerator of uniform modular dimensions (constant impedance) is fed with rf power at one end, there is an exponential decay of power and electric field strength with axial distance from the input end. This means that the average axial electric field is less than the peak axial field in the structure. On the other hand, it is possible to design a structure of non-uniform modular dimensions in which the axial fields will remain constant over the entire length. Such a structure will be referred to as a constant-gradient structure.

The ratio of peak-to-average axial electric field strength is unity in the constant-gradient structure, while in the constant-impedance structure it is given by

$$\frac{E_o \ell}{V_o} = \frac{\tau}{1 - e^{-\tau}} \qquad (6)$$

where $\tau = \frac{\omega t_F}{2Q}$ is the rf attenuation parameter. (The parameter τ has been called $I\ell$ in several previous reports, where I is the rf attenuation in nepers per unit length, and ℓ is the length of the accelerator section. The dependence of τ upon filling time t_F emphasizes the importance of comparing the constant-gradient and constant-impedance structures at the same value of τ for each. For equal τ, the two structures will have the same filling time, the same stored energies, and the same ratios of input to output rf powers (3).) The ratios of peak-to-average axial electric field strength are shown vs τ in Fig. 9. Thus it is clear that the constant-gradient (c.g.) structure

can produce higher electron energies than an optimized constant-impedance (c.i.) structure when both are operating at the breakdown limit of electric-field strength. As indicated in Fig. 9 the relative advantage of the c.g. accelerator in achieving high gradients without breakdown depends upon the value of τ. Curves of field strength vs axial distance z for the two types of structure are shown in Fig. 10 for $\tau = 0.57$.

In addition to the advantage of reduced ratio of peak-to-average field strengths, the constant-gradient structure has several other advantages over the constant-impedance structure:

(a) The power dissipated per unit length in the c.g. accelerator is constant over the entire length of the structure. In contrast, the ratio of power loss at the input end to that at the output end of a constant-impedance structure may be as high as 12.4 to 1. (This magnitude corresponds to a value of the rf attenuation constant $\tau = 1.26$ nepers, which gives maximum no-load energy in the constant-impedance accelerator structure.) A plot of the power-loss ratios for the two structures is shown in Fig. 11.

(b) The c.g. structure gives a slightly higher no-load beam energy than the c.i. structure and somewhat lower beam-loading derivative (-dV/di). Thus, the c.g. structure has greater relative energy advantage in the loaded case than in the unloaded case. The no-load energies for the two structures are shown in Fig. 12 and the beam-loading derivatives in Fig. 13.

(c) The c.g. structure has a higher maximum conversion efficiency (ratio of maximum electron-beam power to input rf power) and a higher corresponding maximum peak beam current than the c.i. structure. Curves of the maximum conversion efficiency, η_{max}, and the corresponding maximum beam current, $i_{\eta_{max}}$, are shown in Fig. 14.

(d) The c.g. accelerator is less frequency-sensitive than the c.i. accelerator, as shown in Fig. 15.

The factors discussed above depend upon τ, as shown in Figs. 9-15. To illustrate these factors numerically, the characteristics of the two structures are shown in Table III, based upon the parameters of the two-mile accelerator.

(e) The c.g. structure is less subject to transient effects than the c.i. structure. Because of the band-pass filter characteristics of an accelerator structure, an impressed rf wave envelope of finite rise time results in amplitude and phase oscillations of the traveling wave. (Calculations of these phenomena, pointed out and made in Ref. (4), have been confirmed by experimental results at Stanford and elsewhere.) These oscillations can be understood if one considers the symmetrical side-bands $\pm \Delta f$ of the carrier frequency (2856 Mc/sec in this case) which make up the rise time of the rf wave. For an operating mode which is close to the middle of the Brillouin diagram, the small side-band vectors rotate around the tip of the carrier vector in opposite directions but by approximately equal angles. The resulting effect as a function of time and as one travels along the structure is predominantly amplitude modulation since the sum of the two vectors remains approximately collinear with the carrier but varies in amplitude. As the operating mode gets closer to the edge of the pass-band, as in the $2\pi/3$ case, both amplitude and phase modulation become apparent. It has been calculated, both at Stanford and elsewhere, that these modulation effects result in an increase of at most 0.5% in the width of the energy spectrum

of the output electron beam. The increase can be further decreased by not triggering all the klystrons at the same time, thereby causing the "peaks" and "valleys" to be "washed" out over a large number of sections. Experiments at Stanford have shown (Fig. 16) that the transient effects are more quickly damped in the c.g. structure than in the c.i. structure.

Certain precautions should be taken, however, when interpreting the pulse shapes of Fig. 16. These pulses are obtained at the outputs of the sections and do not exactly correspond to what the electrons see as they travel down the pipe. Experiments done at Stanford by probing the field through small coupling holes drilled along the sections show that the evolution of the pulse shapes as a function of length is more complicated in the c.g. structure. Interpretation of the results is further complicated by another fact: In addition to the side-bands caused by the rise time of the pulse, there is a frequency modulation effect. This frequency modulation is due to the acceleration, during rise-time, of the bunched electrons in the klystron used to amplify the rf power from the master oscillator. At turn-on, the frequency can in fact be several megacycles higher than when the flat top of the modulator pulse is reached. This initial energy, which travels down the accelerator pipe at a higher frequency, reaches an increasingly narrower pass-band structure. (See Section III.B below.) Before being attenuated, this energy travels at a group velocity which is much lower than the corresponding group velocity at 2856 Mc/sec. When the pulse shape is examined in the middle of the section, the wiggles do not die out, i.e., the filling time is at least 2.5 microseconds long. Finally, towards the coupler end, the higher

frequency energy gets attenuated or reflected and the pulse looks more and more like the simple output pulse shown in Fig. 16. Because of the presence of the higher frequencies, the frequency of the ripples is about twice as high at the input as at the output.

Although this effect is probably unimportant, experiments have shown that a 50% reduction in ripple amplitude can be obtained if a diode modulator at low power, preceding the klystron, is used for rf turn-on. This result can be understood by the reduction in frequency modulation obtained with the p-i-n diode as compared with the klystron alone.

(f) Experiments done at Stanford and elsewhere (5) have shown that the c.g. structure is less troubled by "beam break-up" (also called "pulse shortening") phenomena (6) which are prevalent with the c.i. structure under heavy beam loading conditions. It is now well known that "beam break-up" is caused by excitation by the beam of a backward wave in the TM_{11}-like mode. The radially deflecting properties of this mode have been under study at Stanford (7), (8) since 1959 and are being put to use in various high energy physics laboratories for rf separators (9), bunch analyzers and beam position monitors (10). A complete bibliography can be found in Reference (11).

The mechanism of beam break-up can be understood as follows. Consider a TM_{11}-like wave traveling at a velocity slightly lower than the electrons, which causes these to slip ahead by π in their travel along the accelerator section. In the first half, on-axis electrons find themselves in a strong transverse deflecting region. Depending on their phase, they are deflected either up or down. As they get deflected, they also slip ahead in phase, and in the second half of the section, they find

themselves in a longitudinal decelerating field to which they give up energy. If the current is sufficiently large, the process can start on noise and the TM_{11}-like field grows exponentially.

From this model, it can be seen that beam break-up is less likely in the non-uniform c.g. structure than in the uniform c.i. structure. Figure 17 shows ω-β diagrams for the fundamental TM_{01} mode at the midpoint of a 10-foot c.g. section and for the TM_{11}-like mode at the input, midpoint and output. Note that the $v_p = c$ line intersects each of the higher mode curves at a different frequency, thus making the build-up of the TM_{11}-like mode more difficult.

Typically, various laboratories have reported that for a three-meter long S-band (2856 Mc/sec) constant-impedance accelerator, a beam of about 300 milliamperes sets up a TM_{11}-like wave which in about one microsecond breaks up the beam. At Stanford, it has been found that the process can be triggered in a constant-impedance section with a current of 70 milliamperes by injecting about 800 watts of power at 4326 Mc/sec backwards into the output of the accelerator. The same result could not be achieved with an equal amount of power injected into a constant-gradient structure. From an experiment (12) done at Hughes Aircraft, Fullerton, California, it appears that it takes a beam of 600 milliamperes to cause break-up in three microseconds in a constant-gradient structure about five feet long. Such high currents are not expected in the two-mile accelerator.

The advantages of the constant-gradient accelerator discussed above must be weighed against two disadvantages:

(1) The non-uniform modular dimensions of the cavities in the constant-gradient structure will be more expensive to construct and to test. An economic comparison of the two structures shows that fabrication of the c.g. structure will cost approximately 10% more per unit length than the c.i. structure.

(2) There has been less operational experience with the constant-gradient structure compared with that of the uniform structure.

We have concluded that the advantages of the c.g. structure given above outweigh the relatively small cost differential which its use entails. The c.g. structure has thus been adopted for the two-mile accelerator. High-power tests under way since the spring of 1962 and actual beam tests made with sections installed in the Mark IV and Mark III accelerators (see Section I.A), have confirmed theoretically predicted performance.

H. Choice of Attenuation Parameter

The attenuation parameter is defined as the net attenuation in nepers in an accelerator section caused solely by resistive wall losses. It is equal to the product of the voltage attenuation per unit length and the length of the accelerator section. We have designated this product by the symbol τ (see above). As stated previously, $\tau = \omega t_F/2Q$, where ω is 2π times the operating frequency, t_F is the filling time, and Q is the loss factor in the rf structure. As will be evident in the following discussion, the value of τ influences the performance in many ways, and therefore the proper choice of this parameter is quite important in the design of the two-mile accelerator.

The total energy gain V_T in a constant-gradient accelerator of total length L and shunt impedance r is given (3) by

$$V_T = (1 - e^{-2\tau})^{\frac{1}{2}} \left(P_T L r_o\right)^{\frac{1}{2}} - \frac{i r_o L}{2} \left(1 - \frac{2\tau e^{-2\tau}}{1 - e^{-2\tau}}\right) \qquad (7)$$

where P_T is the total input rf power, i is peak beam current, and r_o is the shunt impedance per unit length.

The first term on the right in Eq. (7) is the no-load energy (i.e., the electron energy at negligible current), and the second term gives the reduction in energy caused by beam loading. The reduction of energy is linear with increase in beam current, as shown in Fig. 18. In plotting these curves it is assumed that the electrons are situated at the peak of the traveling wave.

In the discussion which follows we shall consider the effect of different values of τ upon the constant-gradient accelerator performance. The various accelerator characteristics are shown numerically in Table IV for these values of τ.

1. Beam-loading characteristics

Beam-loading curves for the various values of τ under consideration are shown in Fig. 18. The terminal point on each curve is the beam current resulting in maximum transfer of rf power to the beam. We note that the slope $(-dV/di)$ of the beam-loading curves decreases in magnitude as τ decreases. Since electrons with energies from V_{To} to V_{Ti} emerge from the accelerator during the transient period, lower values of τ are preferred to reduce the energy spread.

2. Maximum conversion efficiency

The maximum conversion efficiency of rf power to beam power is given (3) by

$$\eta_{max} = \frac{1}{2}\left[\frac{(1 - e^{-2\tau})^2}{(1 - e^{-2\tau}) - 2\tau e^{-2\tau}}\right] \tag{8}$$

Maximum conversion efficiency occurs when the beam current reaches the value (3)

$$i_{\eta_{max}} = \left(\frac{P_T}{r_o L}\right)^{\frac{1}{2}}\left[\frac{(1 - e^{-2\tau})^{\frac{3}{2}}}{(1 - e^{-2\tau}) - 2\tau e^{-2\tau}}\right] \tag{9}$$

in which case the beam energy is equal to one-half of the no-load energy.

3. Energy loss and power induced when beam passes through sections not supplied with rf power

When one of the klystron rf power sources becomes defective, it is desirable to be able to continue operation of the accelerator while the klystron is being changed. The amount $(\Delta V)_e$ by which the electron beam energy is reduced by excitation of an idle accelerator section of length ℓ and the induced power P_e in this section are given (3) by

$$(\Delta V)_e = \frac{i r_o \ell}{2}\left(1 - \frac{2\tau e^{-2\tau}}{1 - e^{-2\tau}}\right) \tag{10}$$

$$P_e = i^2 r_o \ell \left(\frac{\tau^2}{e^{2\tau} - 1}\right)$$

The energy loss increases as τ increases, as shown in Table IV. Since each rf source supplies four accelerator sections during Stage I operation,

the total energy loss given by Eq. (10) must be multiplied by four. This loss is, of course, in addition to the loss of beam energy that would normally be contributed by the four sections (about 40 MeV when the total energy is 10 BeV).

4. Group velocity

In the constant-gradient accelerator, the group velocity decreases linearly with distance along the accelerator section. It is given (3) by

$$v_g = \frac{\omega \ell}{Q} \left[\frac{1 - (z/\ell)\,(1 - e^{-2\tau})}{1 - e^{-2\tau}} \right] \tag{11}$$

5. Filling time

A small filling time is desirable to allow the maximum available portion of the rf pulse length for the acceleration of electrons. The filling time is given (3) by

$$t_F = \frac{2Q}{\omega}\,\tau \tag{12}$$

Values of filling time for the various cases are given in Table IV.

6. Frequency sensitivity

The fractional beam-energy loss from a fractional frequency shift $\delta f/f$ is given (3) by

$$\frac{\delta V_o}{V_o} = \left(Q\frac{\delta f}{f}\right)^2 \left[\frac{2\tau e^{-2\tau}\,(\tau + 1)}{1 - e^{-2\tau}} - 1 \right] \tag{13}$$

Values of $\delta V_o/V_o$ are shown in Table IV for $\delta f = 0.1$ Mc/sec.

7. Conclusions

From Table IV it is clear that there are several advantages to using a reduced attenuation parameter τ. Except for the reduction in beam energy, the general statement can be made that the use of a low value of τ results in improvement of all of the factors measuring the performance of the accelerator. Moreover, the percentage improvement of each of these factors resulting from a given reduction in τ usually exceeds the percentage loss in beam energy. If it were not for the paramount importance of high beam energy in particle-physics research, the adoption of a very low value of τ would clearly be indicated. It has not seemed reasonable to us to make the selection on a strict analytical basis. We have instead made the choice of τ on the basis of broad considerations, including reference to such tabulations as shown in Table IV, the prospective requirements of physics research, and previous accelerator experience. We have chosen the value of $\tau = 0.57$ for the sections of the two-mile accelerator.

(The original basis for $\tau = 0.57$ was that this particular value resulted in a no-load energy in the constant-impedance accelerator which is 10% less than the maximum no-load energy which can be obtained (occurring at $\tau = 1.26$). This was judged to be the maximum penalty in energy which one could afford to pay to obtain the advantages of low τ discussed in the text. The same qualitative reasoning holds for the constant-gradient accelerator structure, and thus we have not seen fit to change the value of τ selected earlier.)

III. EMPIRICAL DESIGN OF THE ACCELERATOR STRUCTURE

A. Choice of the Disk-Loaded Waveguide

The previous sections of this article have been concerned with the general determination of accelerator parameters. This section describes the procedures used to design empirically an accelerator structure that satisfies the above parameters.

The disk-loaded waveguide is not the only slow-wave structure capable of accelerating electrons. In fact, other structures (see Fig. 19) such as the grid-loaded ("Jungle Gym") waveguide yield shunt impedances about twice that of the disk-loaded waveguide. But in every case we have examined where a large improvement in shunt impedance (r) is obtained, the bandwidth and resulting group velocity are at least ten times as high as desired. Efficient utilization of the available rf power under these conditions would have required its recirculation (feedback) or the use of extreme lengths between feeds. The former is undesirable, especially in a long multisection accelerator, because it results in undue operational complications; the latter requires that each accelerator section transmit an excessive amount of power. Several variations of structures 2 through 8 shown in Fig. 19 were devised which succeeded in reducing the group velocity to the desired values (in the range of 0.01 c), but these measures also caused the shunt impedance to be reduced until no advantage remained; moreover, they resulted in increased cost of fabrication. For these reasons, use of the disk-loaded waveguide appeared preferable for the two-mile accelerator.

B. Definition and Discussion of Dimensions

The modular dimensions of the disk-loaded waveguide which can be adjusted to achieve the intended parameters are illustrated in Fig. 4. Figure 4(a) shows the cylindrical guide diameter 2b, the disk-hole diameter 2a, the disk-edge radius ρ, and the land in the disk aperture s. Figure 4(c) shows further variations of the disk-loaded waveguide using so-called "conical" or "anti-conical" disks. The conical disk was rejected because of its comparatively low r/Q. The anti-conical disk was dismissed because of machining difficulties, although it has a five percent higher r/Q than the corresponding flat disk structure with $t = t_1 = 0.230$ inch.

As indicated in Section II.F, a 10 percent improvement in shunt impedance can be gained by adopting the $2\pi/3$ mode rather than the $\pi/2$ mode. Figure 20 illustrates the respective traveling-wave field configurations at an instant in time over two wavelengths (the zero and π "standing-wave modes" are also illustrated for reference). These patterns are deformed as they slide down the waveguide but reappear in the same configuration, shifted by one cavity, at an instant $\delta t = \Phi/2\pi f$ later, where Φ is the phase shift per cavity at the frequency f. For standard accelerator sections, the objective is to obtain a phase velocity equal to the velocity of light. Thus, specifying the operating mode and frequency (or free-space wavelength) fixes the distance between disk center lines at $d = \Phi c/\omega$.

After this choice, only four dimensions remain to be specified: 2b, 2a, ρ and t. The lower cut-off frequency of the disk-loaded waveguide, or "zero-mode" frequency, is strongly dependent upon the waveguide

diameter 2b, whereas the bandwidth and thus the group velocity depend primarily on the ratio a/b at given values of ρ and t. This point is illustrated by the three ω-β (Brillouin) diagrams shown in Fig. 21. It is important to verify that the disk aperture edge has been properly formed, through some technique such as that utilizing a steel ball [Fig. 4(b)] or a more sophisticated contour plotter. Errors in the ball height h or the land s cause significant errors in the resonant frequency of test sections and hence in the resulting phase and group velocities. This fact is easily understandable because the electric field intensity is relatively strong at the disk edge. The choice of ρ can be quite arbitrary from the rf point of view as long as the tolerances are respected and electric breakdown does not result.

The choice of the disk thickness t, as discussed in Section II, involves a compromise between the use of thin disks to increase the shunt impedance and thick disks to reduce the danger of electrical breakdown and to improve heat-transfer characteristics.

C. Evolution of Stanford Designs

Prior to 1960, all Stanford accelerators were designed to operate in the $\pi/2$ mode. Starting in 1960, the first $2\pi/3$ mode structures were tested on the 20-foot Mark IV accelerator (Section I.A). Until 1962, all Stanford accelerators had constant-impedance structures. In April 1962, the first constant-gradient structure was installed on the Mark IV accelerator. As noted in Section I.A, SLAC type constant-gradient structures were installed on the Mark III accelerator in December 1963, replacing the earlier $\pi/2$ structures.

Table V shows the respective characteristics of constant-impedance structures operating in the $\pi/2$ mode on the early Mark III accelerator and in the $2\pi/3$ mode on the Mark IV accelerator.

D. Constant-Gradient Structure Dimensions

As discussed in Section II, the two-mile accelerator is of the constant-gradient type, propagating in the $2\pi/3$ mode. The constant field is obtained by tapering the cross-sectional dimensions of the waveguide so as to produce the required linear decrease in group velocity. The constant-field condition results only if the shunt impedance and the Q of the cavities remain constant over the length of the section in spite of the cross-sectional variation of the structure. In practice, for a group velocity variation such as that chosen for the Stanford design, the shunt impedance r_o (corrected for the fundamental space harmonic) increases by a small percentage over a ten-foot section, thereby yielding a structure with a gradual input-to-output-field increase of five percent. This result is actually desirable because the effect of beam loading will tend to depress the rising field characteristic by an amount depending on the beam current.

Two constant-gradient structures were designed, one for thick disks ($t = 0.230$ inch), the other for thinner disks ($t = 0.120$ inch). Their performances were compared and the thicker disk design was chosen. The thinner disk design was dismissed because of lower mechanical strength and, as mentioned earlier, because of the higher probability of electrical breakdown at the disk aperture. Figures 22 and 23 show the respective variations of 2b, 2a, v_g/c, and r_o as a function of cavity number

along a 10-foot section. Cavities 0 and 85 are coupler cavities. It is seen that whereas 2b varies by less than 2 percent, 2a is reduced at the output by 30 percent from its input value to satisfy the group-velocity variation.

For reasons of economy, a constant-gradient design can be approximated by adjusting the dimensions in steps, each step consisting of several identical cavities. However, for the two-mile Stanford accelerator, the cost of the slow-wave structure represents only a small percentage of the total cost, and the small increase incurred by varying the dimensions cavity by cavity is well justified to achieve a very smooth field gradient with virtually no reflections.

E. Cold Tests and Corrections to Achieve the Empirical Design

1. Objectives and validity of cold tests

A theoretical treatment sufficiently accurate to permit calculation of the dimensions of the constant-gradient designs shown in Figs. 22 and 23 does not exist. Consequently these dimensions had to be determined experimentally from cold tests. To achieve an accurate design, a fair number of pairs of 2b and 2a values had to be determined, each set of values being obtained from a different resonant test cell. About ten different test cells were used for each of the constant-gradient designs. For each test cell, the following quantities were measured: the phase velocity v_p, the group velocity v_g, r/Q, Q, and the fundamental space harmonic amplitude $a_o^2/\Sigma a_n^2$. It is not the objective of this article to describe in great detail each of these microwave measurements. A comprehensive treatment of this subject can, for example, be found in References (2), (13), and (14). However, a brief comment will be made on each of these measurements

to outline the techniques used and to point out some of the necessary precautions. A discussion of the corrections applied to the experimental results will then be given.

Results of cold tests on short test cells are valid if the reflection symmetries of the structure are carefully taken into account. Shorting plates must be located only in planes to which the electric-field vector is normal and in such a way that the standing wave "trapped" between them is an exact representation of the instantaneous traveling wave one wishes to study. The dotted lines in Fig. 20 show such planes. For observation of the $2\pi/3$ mode, sets of three or six identical cavities are used, covering one or two full wavelengths. These cavities are made of carefully machined copper or brass cups and rings, half rings being used at the end to meet the correct boundary conditions.

When measurements are being made, it is essential that the cavities be stacked and aligned very carefully, preferably by means of a concentric jacket, and that good electrical contact be obtained through a uniformly applied pressure.

2. Measurement of phase velocity v_p

Figure 24 shows a typical Brillouin diagram with the phase velocity $v_p = c$ for a $2\pi/3$ phase shift per cavity at $f = 2856$ Mc/sec. The disk spacing is fixed at $\lambda/3 = (c \times 10^{-6})/(3 \times 2856)$cm. With three or six cavities of the type shown, four or seven resonant frequencies respectively representing $n\pi/3(0 \leq n \leq 3)$ or $n\pi/6(0 \leq n \leq 6)$ phase shift per cavity can occur; these points can be recorded to draw the ω-β diagram. With a moderate amount of experience, three rounds of machining

correction of the diameter 2b are sufficient to approach the operating frequency (2856 Mc/sec) within less than 1 Mc/sec at the $2\pi/3$ resonance. The remaining correction is done by mathematical extrapolation. In this manner one insures that the resonant frequency for the $2\pi/3$ mode will be 2856 Mc/sec, and operation at this frequency will result in propagation of a traveling wave in a structure of the same modular dimensions at $v_p = c$.

3. Measurement of group velocity v_g

The condition $v_p = c$ can be obtained for various pairs of 2b and 2a values. Each pair yields a different ω-β diagram and hence a different group velocity. This fact was illustrated in Fig. 21. Figure 25 shows the two cavity stacks for the extreme cases, the first and the last cavities of the constant-gradient section. The differences in 2a for $v_g/c = 0.0204$ and $v_g/c = 0.0065$ should be noted. To obtain the group velocity, one can graphically take the slope of the ω-β diagram or, for better accuracy, use the measured resonance frequencies in connection with a Stirling or Fourier approximation formula.(15)

4. Measurement of r/Q

The ratio of shunt impedance per unit length to Q is best measured by axially perturbing the test cell with a thin dielectric rod, and by measuring the resonant frequency perturbation Δf. Using Slater's perturbation formula (14, 16) the value of $(r/Q)_T$ (where the index T denotes the sum of all space-harmonic components) is given by

$$\left(\frac{r}{Q}\right)_T = \frac{240c}{(\epsilon - 1)A} \frac{\Delta f}{f^2} \qquad (14)$$

where ϵ is the dielectric constant of the rod (for sapphire $\epsilon \approx 10$), and A is its cross section. It is desirable to calibrate the dielectric rod in a simple TM_{010} cavity, for which r/Q can be calculated.

5. Measurement of the space-harmonic amplitude

Since only the fundamental space-harmonic propagates at $v_p = c$, it alone gives a net energy gain to the electrons. Thus, to obtain the effective $(r/Q)_o$, it is necessary to obtain the amplitude of the fundamental. The figure of merit by which to multiply $(r/Q)_T$ to obtain $(r/Q)_o$ is $a_o^2/\Sigma a_n^2$, the ratio of the square of the fundamental harmonic amplitude divided by the sum of the squares of all harmonic amplitudes. This ratio can be obtained by noting the frequency perturbation caused by a short electric bead drawn along the axis of the resonant test cell. The field E_c at a given axial position in the cavity is related to the frequency perturbation Δf caused by a bead located at that position by

$$E_c^2 = k\Delta f \tag{15}$$

where k is a constant depending on the characteristics of the bead. For best accuracy, the following precautions should be taken:

(a) The bead should be no longer than 2 to 3 millimeters to give good resolution.

(b) Six rather than three cavities should be used so that an entire half-wavelength can be probed without letting the bead approach the end plates, where its image increases the actual perturbation.

(c) It is preferable to measure the perturbed frequency by adjusting frequency to locate the new peak of the response curve rather than by observing power response as a function of bead position

at constant frequency. This technique avoids the difficulties (17), (18), (19) which arise from simultaneous changes in the resonant frequency and the coupling coefficients of the cavity.

(d) Before plotting the whole field pattern, one should insure, by using the method recommended in (c) above for a few points symmetrical with respect to points of reflection symmetry, that the field is symmetrical. If it is not, the adjustment of small tuning plungers at the top of the test cell will enable symmetry to be established. These plungers compensate for the asymmetry created by slight differences in insertion of the input and output coupling loops.

After the field pattern has been obtained, one can divide it into N intervals (typically N = 21) and carry out a Fourier analysis to obtain the figure of merit, which is given by

$$\frac{a_o^2}{\Sigma a_n^2} = \left(\frac{2}{N}\right) \frac{\left[\sum_{m=0}^{m=N} E_{cN} \cos \frac{m\pi}{N}\right]^2}{\sum_{m=0}^{m=N} E_{cN}^2} \qquad (16)$$

The denominator is simply the area under the Δf curve. The numerator is obtained by extracting the square root of the Δf curve and using physical reasoning to determine the sign of the electric field at each point.

6. Measurement of Q

To obtain the value of Q is the most delicate of these measurements

because it depends on the state of the metal surface and on good contact between cavities, conditions which are hard to achieve and to maintain. It is preferable to take the measurements immediately after electropolishing the cavities. Using very weak coupling, one successively obtains the Q's of three-cavity (Q_3) and six-cavity (Q_6) sets by the half-power point technique:

$$Q = \frac{f}{\Delta f} \tag{17}$$

where f is the resonant frequency and Δf is the frequency variation between half-power points. Although these Q's contain the losses caused by the end plates, it is simple to show (14) that end-plate effects can be eliminated through use of the following expression:

$$Q = \frac{Q_3 Q_6}{2Q_3 - Q_6} \tag{18}$$

The Q measurement requires the following precautions:

(a) The signal generator should not exhibit spurious outputs.

(b) The input power must be carefully monitored.

(c) To eliminate errors due to uncertainties in crystal law behavior at varying power levels or indicator calibrations, it is preferable to work at a constant crystal power level. This can be achieved by using a precision attenuator which is adjusted from 3 db to 0 db as the resonant frequency and the half-power frequencies are sought.

A check of the Q measurement can be obtained by measuring the attenuation of an accelerator section after final assembly.

7. Corrections and use of computers

In order to build a constant-gradient section with fixed t, d, and ρ dimensions, only 2b and 2a must be determined. These depend only on v_p and v_g, and their relationship with these parameters must be determined accurately. The quantities $(r/Q)_o$ and Q need not be known as precisely, because to a first approximation they do not enter into the design.

Measurements should be carried out in an environment having accurately controlled temperature and humidity. Further, machining test cavities to attain the exact design frequency is not practical, and 2b must be corrected for the residual Δf. It is usually sufficient to base the correction on the simple relation

$$\frac{\Delta 2b}{\Delta f} \approx - \frac{2b}{f} = -0.0011 \text{ inch/Mc (at 2856 Mc/sec)} \qquad (19)$$

Another correction is required to arrive at a certain operating frequency for a given copper temperature which differs from the room temperature at which the tests are being performed. In addition, most cold tests are done in air, and a correction must be applied to obtain the dielectric of air, which is a function of the ambient humidity and temperature (see Adam's Nomograph in any engineering handbook). These problems are not very critical for short test-cell measurements, but they become important during matching and tuning operations (Section III.F). For copper, the following rules of thumb can be applied at 2856 Mc/sec:

$$\frac{\Delta f}{\Delta T} = -0.100 \text{ Mc}/2^{\circ}\text{C} \qquad (20)$$

For a passage from air at 80°F and 40 percent humidity to vacuum, the frequency increase is about 300 parts in one million.

Having applied these corrections, the data can be smoothed by plotting the points, or alternately, by computer techniques. Using a fourth- or sixth-order polynomial, a method minimizing least-square deviations from the experimental points can be used to yield the required combinations of v_g and (2b, 2a) to produce the constant-gradient design.

F. Basic Considerations in Matching and Tuning an Accelerator Section

If the process of machining parts and fabricating an accelerator structure could be carried out with perfect accuracy, a section such as the one shown in Fig. 26 should be ready for installation and use immediately after fabrication.

In practice, however, it is difficult to control the process of manfacturing to this extent; moreover, it does not appear economically desirable to try to do so. By relaxing the tolerances on either of the techniques described later in Section IV, it is possible to reduce the cost of the accelerator considerably. The imperfections can be corrected through the process of tuning and matching as described below for a relatively small incremental cost.

The process of tuning an accelerator section (also see section IV) consists of applying an external mechanical pressure which imparts a permanent deformation to the inside wall of any cavity whose phase shift differs from the design value. A maximum phase excursion of $\pm$ 2.5° has been imposed on the 10-foot sections of the two-mile machine.

The process of matching the couplers of an accelerator section consists of adjusting the dimensions of the input and output coupling irises (see

Fig. 26) so as to insure a low standing-wave ratio at the input and output of the structure. An upper VSWR limit of 1.05 has been set as the matching requirement for all couplers. The main technical difficulty stems from the fact that the processes of tuning and matching are inter-related; the shape of the coupling iris determines both the coupling to and the phase shift of the first cavity.

A complete description of the theory and operations involved in tuning and matching an accelerator section is beyond the scope of this paper (2), (13), (14), (20), (21), (22). Only a few of the general principles and relevant precautions are given below.

Although the simplest mode to tune and match is the $\pi/2$, any sub-multiple of 2π, such as the $2\pi/3$ mode, can be dealt with without undue difficulty.

Figure 27 illustrates the principle of the nodal-shift technique utilized in tuning. A copper plunger, progressively pulled through the structure (shown in cutaway section in the figure), detunes successive cavities and thereby causes the standing-wave pattern to shift. If the coupler is perfectly matched and all cavities have 120° of phase shift ($2\pi/3$ mode), pulling the plunger away from the coupler causes the plotted null points to rotate clockwise by 240° on the Smith chart for each cavity length through which the plunger is moved. Starting from the reference point of 0°, obtained by detuning the coupler cavity (and hence representing the plane of the iris), the points move clockwise as shown in Fig. 27 from 0° to 120°, from 120° to 240°, from 240° to 0°, and so on. For the first cavities, the VSWR is infinite and the points are on the rim of the chart. Further down the section, the VSWR decreases because of the increasing

net attenuation between the input of the section and the short. Thus, the plotted points move toward the center of the chart along the three radii, shown as dashed lines in Fig. 27. With the coupler perfectly matched but the cavities not exactly tuned, the points move erratically toward the center, as shown by the heavy lines. However, the center of the circle passing through three consecutive points still coincides with the center of the chart. When a systematic phase-shift error exists, because of an inaccurate choice of frequency, the points spiral in toward the center, clockwise if the phase-shift is too large (frequency too high), or counterclockwise if it is too small (frequency too low). If the coupler is mismatched (see Fig. 28), the circle passing through the three points is no longer concentric with the rim of the chart. It now has two "centers," a geometrical center and a "Smith center." Neither coincides with the center of the chart. The Smith center is the point that would be obtained if the perfectly reflecting plunger were replaced by a perfectly matched load. It can be determined mathematically (13), (14) from geometric considerations. The matchpoint (C) will lie on the extension of the straight line from the center of the Smith chart (O) to the geometric center of the circle (M). Its VSWR (σ at the matchpoint) is determined by $\sqrt{\sigma_{max}/\sigma_{min}}$ if the circle encompasses the center of the chart, and by $\sqrt{\sigma_{max}\sigma_{min}}$ if it does not. Matching the coupler consists of bringing point C as close as possible to point O. This is achieved by adjusting the coupling iris. Filing or squeezing affects the coupling, but they also affect the phase shift of the coupling cavity. Bending the iris in or out can compensate for this change. For the location of point C shown in Fig. 28, the actions indicated must be taken (bending the iris inward and filing to

increase the iris opening). In general, the combination of bending and filing is required to achieve a good match.

The process of tuning is illustrated in Fig. 29 for a short experimental section of accelerator pipe. The tuning tool here is applied to the third cavity. It consists of a demountable collar with two or three radially adjustable screws having rounded ends. By driving the screws into the wall of the accelerator, a gentle protrusion on the inside wall of the cavity can be created. To preserve cylindrical symmetry, it is best to obtain the desired phase shift with two or more dimples uniformly distributed around the circumference. Errors $\Delta(2b)$ in the dimension 2b create phase shifts $\Delta\varphi$ given by

$$|\Delta\varphi| = \frac{2\pi}{3} \frac{c}{v_g} k \frac{\Delta(2b)}{f} \qquad (21)$$

where $k \approx 1.1$ Mc/0.001 inch. For example, an error of 1° corresponding to a $\Delta(2b)$ of 0.0002 inch can easily be eliminated. In fact, it is advisable with a multisection accelerator to make all cavities slightly oversize to begin with, because the lowest frequency to which a cavity can be tuned with this technique is determined by the smallest cavity in the assembly, and all cavities must be tuned to the same frequency.

Because field lines can extend over three disks in the $2\pi/3$ mode configuration, the tuning of the first cavities and the matching strongly interact. It has been pointed out (23) that this property can cause serious difficulties. If the coupler is not well matched, tuning the first cavities by bringing the points to the proper positions on the Smith chart can actually cause the following effect: Successive cavities will have built-in cyclic phase errors $\Delta\varphi_1$, $\Delta\varphi_2$, $\Delta\varphi_3$ which compensate for the

reflection caused by the coupler. Since the VSWR for the nodal shift in the first cavities is infinite, the matchpoint C is indistinguishable from the center O of the Smith chart, and the structure appears to be tuned and matched. In reality, a double or triple periodicity can be built into the section, which causes passband splitting. It has been predicted (23) that the split would occur at approximately the $\pi/2$ frequency for a $2\pi/3$ section.

Precautions can be taken to avoid this possible ambiguity. One remedy consists of using a resistive plunger which even in the first cavities allows the position of the matchpoint C to be identified. Another remedy consists of achieving the match by successive approximation, e.g., tuning and matching very carefully with the reactive plunger alternately in the first three cavities and, say, cavities 9, 10 and 11. At the latter points, there is enough loss to permit determination of the VSWR of the matchpoint C with good accuracy. This result can also be achieved (24) by separately pre-matching the couplers with a perfect three-cavity assembly before final brazing of the section. A particular technique to pre-match the coupler without a perfect three-cavity assembly has also been worked out (25) for particular use with a structure operating in the $2\pi/3$ mode. In this technique it is necessary to know the frequency at which each cavity has $\pi/2$ phase shift. This method is useful in preventing any incorrect matching which could cause the incorrect tuning mentioned above.

A few more remarks may be pertinent:

(a) The matching and tuning operation must be performed in a carefully temperature-controlled, dry room. Sections should be allowed to stabilize thermally for several hours. Ideally, the tuning operation

should be done with the section filled with a dry atmosphere.

(b) The detuning plunger should be light and clean in order to prevent damage or contamination of the disk edges. Notches should be provided so that the plunger always rests in the same relative position, or dwell point, around which small motions do not disturb the null. When tuning a constant-gradient section, where the 2a dimension changes as a function of length, the largest possible plunger compatible with the smallest 2a dimension should be used. It has been verified that, in this manner, the dwell condition can be achieved in all cavities.

(c) In the $2\pi/3$ mode it has been found that moving the plunger slowly (less than a full cavity) away from the coupler causes the null on the slotted line to move toward the generator by one-half the phase shift introduced. This surprising effect is attributable to the manner in which the plunger detunes the cavity and not to any actual phase reversal. When the plunger finally moves into the dwell point in the next cavity, the null appears in the correct place.

(d) The two-mile accelerator sections will be provided with output couplers and loads to prevent a reflected wave from appearing at the klystron amplifiers. These couplers must be tuned in the manner described in conjunction with the input couplers, preferably by switching over the whole experimental setup to the output coupler.

(e) When a section has been matched and tuned, three final rf checks are advisable: (1) The global match can be checked with a continuously movable short in the rectangular waveguide beyond the output coupler (14). This measurement involves observing the image of two intersecting diameters on the Smith chart, transformed through the complete section including the two couplers. This image of the "iconocenter" must fall at

the center of the chart. (2) The global match can be checked with a matched load at the output or input ends. (3) The attenuation can be measured globally for the entire section by direct substitution techniques, or for a part of the section by measuring the change in reflection coefficient as a function of plunger position.

Finally, it is often of interest to obtain a complete traveling-wave field plot for the entire accelerator section. This plot can be obtained by drawing a small dielectric or metallic bead along the axis of a disk-loaded waveguide structure which is excited at one end by a signal generator and matched at the other end with a load. The relative field amplitude is obtained by measuring either the reflection coefficient caused by the reflected wave from the bead, or the phase shift across the section caused by the forward-scattered wave from the bead. The phase of the field can be measured by noting the phase of the reflection coefficient of the reflected wave.

It is interesting to note that if one wants to recheck the relative amplitude of the fundamental space harmonic $\left(a_o^2/\Sigma a_n^2\right)$ by this method, both electric field amplitude and phase are needed, as shown by the derivation below. The total field is given by the expression

$$E_z(z,t) = \sum_{n=-\infty}^{n=+\infty} a_n(r)e^{j(\omega t-\beta_n z)} \tag{22}$$

Integrating over the length of one cavity, one obtains

$$a_n = \frac{1}{d}\int_{-d/2}^{+d/2} E_z(z)e^{j\beta_n z}dz \tag{23}$$

Notice, however, that E_z in this expression is a complex quantity of the form $|E_z(z)|e^{-j\theta(z)}$ where the plots of $|E_z(z)|$ and $\theta(z)$ are given by the perturbation measurements. Choosing the origin in the middle of a cavity and observing symmetry, it is then possible to obtain a_n and hence $a_o^2/\Sigma a_n^2$ by evaluating the integral

$$a_n = \frac{2}{d} \int_0^{d/2} |E_z(z)| \cos [\beta_n z - \theta(z)]dz \qquad (24)$$

Generally, it is sufficient to calculate only three or four terms to obtain 1% accuracy.

It is also interesting to note why the traveling-wave measurement requires the measurement of both θ and $E_z(z)$ whereas the standing-wave measurement described in Section III.E.5 can be made with $E_c(z)$ alone. The reason is that in the cavity measurement, there are two waves traveling in opposite directions:

$$E_c(z,t) = \sum_{n=-\infty}^{n=+\infty} a_n e^{j(\omega t-\beta_n z)} + a_n e^{j(\omega t+\beta_n z)} \qquad (25)$$

$$= \sum_{-\infty}^{+\infty} 2a_n \cos \beta_n z e^{j\omega t}$$

Hence, a_n is given by:

$$a_n = \frac{2}{\lambda} \int_0^{\lambda/2} E_c(z) \cos \beta_n z dz \qquad (26)$$

where the quantity $E_c(z)$ is either positive or negative but contains no phase.

Field plots of entire prototype sections have been carried out and have been helpful in obtaining a final smooth variation of the dimensions 2a and 2b.

G. Corrections of Dimensions of Prototype Section

Final modifications in the dimensions of the disk apertures 2a (and accompanying changes in the cavity diameters 2b) can be made using data from completed 10-foot sections.(26) The technique consists of comparing the measured field variation and attenuation in a section with the field variation and attenuation required for a constant gradient structure, taking into account the effect of beam loading. The original objective was to arrive at a constant gradient with 10% beam loading. It was found, however, that this required too small a beam aperture. A minimum disk aperture of 0.750 inch was set, with the resulting structure having a constant gradient at about 5% loading.

For specified values of attenuation, fractional beam loading, and input power, and with known average shunt impedance of the structure, the ideal attenuation along the structure is given (27) by

$$A_n = \frac{1}{2} \frac{1}{\frac{P_o}{(\delta P)_{Tn}} - n} \left\{ \frac{r_n i^2}{2(\delta P)_{Tn}} + 1 - \left[\left(\frac{r_n i^2}{2(\delta P)_{Tn}} \right)^2 + \frac{r_n i}{(\delta P)_{Tn}} \right]^{\frac{1}{2}} \right\} \qquad (27)$$

where

A_n = Loss due to dissipation in n^{th} cavity (nepers)

P_o = Specified input power

$(\delta P)_{Tn}$ = Power lost to beam and circuit in n^{th} cavity

r_n = Shunt impedance of n^{th} cavity (assumed constant)

i = Average beam current during pulse

Additionally, the average beam current during the pulse and the power lost to the beam and the circuit are obtained (28) from

$$i = (\text{Fractional Beam Loading}) \left\{ 2 \frac{\left(P_o \sum_{n=o}^{N-1} r_n \right)^{\frac{1}{2}} (1-e^{-2\tau})^{\frac{1}{2}}}{\sum_{n=o}^{N-1} r_n \left(1 - \frac{2\tau e^{-2\tau}}{1-e^{-2\tau}} \right)} \right\} \tag{28}$$

and

$$(\delta P)_{Tn} = (\delta P)_{Bn} + \frac{(\delta P)^2_{Bn}}{i^2 r_n} \tag{29}$$

where $(\delta P)_{Bn}$, the energy absorbed by the beam in the n^{th} cavity, is

$$(\delta P)_{Bn} = \frac{i}{N} \left\{ \left(P_o \sum_{n=o}^{N-1} r_n \right)^{\frac{1}{2}} (1-e^{-2\tau})^{\frac{1}{2}} \frac{i \sum_{n=o}^{N-1} r_n}{2} \left(1 - \frac{2\tau e^{-2\tau}}{1-e^{-2\tau}} \right) \right\} \tag{30}$$

τ = Total attenuation through the structure (nepers) without beam loading.

N = Total number of cavities in structure.

The power dissipated in the circuit is given by the term

$$\frac{(\delta P)^2_{Bn}}{i^2 r_n} \tag{31}$$

The desired values of circuit attenuation as represented by the A_n obtained from Eq. (27) are compared with values of A_n obtained from measurements of the relative field strength along the accelerator section and its total attenuation. These measured values (denoted by primes) are obtained using:

$$A'_n = A_o \left(\frac{E_n}{E_o}\right)^2 e^{2 \sum_{n=o}^{n-1} A'_n} \tag{32}$$

where

E_n/E_o = the relative field strength in the n^{th} cavity.

A_o is the loss in nepers in the first cavity due to rf dissipation. For use here it is determined from the total attenuation measurement and data from the relative field strength plot and is given by

$$A_o = \frac{1-e^{-2\tau}}{2 \sum_{n=o}^{N-1} \left(\frac{E_n}{E_o}\right)^2} \tag{33}$$

The differences between the measured and required values of A_n in conjunction with group velocity measurements are used to obtain corrections for the aperture diameter.

$$\Delta(2a)_n = \frac{\left(\frac{v_g}{c}\right)'_n \left[\frac{A'_n}{A_n} - 1\right]}{\left.\frac{\partial \left(\frac{v_g}{c}\right)}{\partial (2a)}\right|_n} \tag{34}$$

2a = aperture diameter

v_g = group velocity

(primes denote measured values)

Changes in the disk aperture affect the phase velocity and are compensated by corresponding changes in cylinder diameter (2b) by

$$\Delta (2b) = \Delta (2a) \frac{\partial f/\partial(2a)}{\partial f/\partial(2b)} \tag{35}$$

The curves of 2a and 2b given in Fig. 22 for the thick disk case have been corrected in accordance with the procedure just described.

H. The Coupler Asymmetry Problem and the "baba-abab" Waveguide Configuration

The configuration of the waveguides feeding the accelerator, as illustrated in Fig. 2, has been chosen as the best possible remedy to the problem of coupler asymmetry which will be described in this section. This configuration follows the so-called "baba-abab" pattern, in which, looking downstream, an "a"-type waveguide feed comes from the left and a "b"-type feed comes from the right. Successive 40-foot girders alternate between the "baba" and the "abab" periodicity. How this fairly complicated configuration was arrived at is explained below:

In any normal accelerator cavity, the field configuration has cylindrical symmetry. However, the coupler cavity with its matching iris aperture is an exception. It has been known for a number of years that the longitudinal electric field in this cavity is slightly asymmetrical. Referring to Fig. 30(a), E_z is somewhat larger on the right side, i.e., close to the iris, than on the left side. It has also been understood (29), (30) that this transverse gradient of $|E_z|$ is equivalent to a magnetic field B_y which in turn subjects the electrons to a Lorentz force F_x.

A more recent examination of the E_z field by means of microwave perturbation measurements revealed that there are both amplitude and phase asymmetries in the transverse plane of the coupler. These measurements consisted of plotting both the amplitude and the phase of a wave reflected by a small longitudinal bead as a function of bead position in the coupler cavity. For an uncorrected cavity as shown in Fig. 30(a), the

amplitude asymmetry is of the order of 10% and the phase shift is of the order of 1.5° over the beam aperture.

To understand the effect of these asymmetries on the beam, one must examine the expression of the longitudinal electric field. Let the spatial variation of E_z be of the form

$$E_z = \left[E_{z,o} + \frac{\Delta E}{2a}\, x\right] e^{j \frac{\Delta\varphi}{2a} x} \tag{36}$$

where ΔE and $\Delta\varphi$ are the amplitude and phase variations in the x-direction over the aperture diameter 2a averaged from 0 to d, the cavity length. Then, to first order,

$$\frac{\partial E_z}{\partial x} = j \frac{\Delta\varphi}{2a} E_{z,o} e^{j \frac{\Delta\varphi}{2a} x} + \frac{\Delta E}{2a} e^{j \frac{\Delta\varphi}{2a} x} \tag{37}$$

From Maxwell's equations, B_y and hence the Lorentz force F_x are both in time quadrature with $\frac{\partial E_z}{\partial x}$. Referring to Fig. 30(b), the deflecting force F_x', caused by the phase asymmetry and proportional to $\frac{\Delta\varphi}{2a} E_{z,o}$, is in phase with the accelerating force F_z; it produces a net deflection on a bunch traveling on the crest of the wave. On the other hand, the force F_x'', caused by the amplitude asymmetry and proportional to $\frac{1}{2a}\left(\frac{\Delta E}{E_{z,o}}\right) E_{z,o}$, is in quadrature with the accelerating force F_z; its effect, as shown in an exaggerated form in Fig. 30(b), is to spread transversely a bunch travelling on the accelerating wavecrest. In practice, both of these effects occur simultaneously and are undesirable.

Using simple electrodynamics, it can be shown that the transverse momentum δp_x imparted to an electron traveling at an angle θ with respect

to the accelerating wavecrest through a coupler cavity of length d is given by:

$$\delta p_x = \frac{eE_{z,o}\lambda d}{4\pi ac}\left[\Delta\varphi \cos\theta + \frac{\Delta E}{E_{z,o}} \sin\theta\right] \qquad (38)$$

It has been shown (30) that unless $\frac{\Delta E}{E}$ can be kept smaller than 0.1% and $\Delta\varphi$ less than 0.06°, serious difficulties might arise in steering the beam over the two-mile length. In particular, steering of multiple beams of different energies through accelerator sections which are powered for one beam (and hence cause a deflection) and are unpowered for another (thus causing no deflection) would be extremely difficult and probably impossible without pulsed steering magnets. To remedy these difficulties, several measures have been taken:

(a) Offsetting the coupler cavity as shown in Fig. 30(c) has almost completely compensated for the amplitude asymmetry. The value of the offset was found through successive approximations using microwave perturbation measurements; for the input cavity it is 0.155 inch and for the output cavity, 0.080 inch. Within the accuracy of the measurements, the value of $\Delta E/E$ is thereby reduced to 0.1% or less.

(b) Attempts to compensate for the phase asymmetry inside the coupler cavity have not met with a simple solution. Experiments which intentionally used slightly misaligned cavities were not successful in reducing $\Delta\varphi$. The only practical solution would appear to be a symmetrically fed coupler cavity with two irises. However, such a solution would be expensive and fairly impractical since it would require an additional power splitter.

The "baba-abab" waveguide configuration shown in Fig. 2 is actually a

practical version of the double iris coupler where the symmetrical feeding is done on successive sections. Of all the alternative configurations, the "abba-abba" or "baab-baab" periodicities would in fact be the simplest because they re-establish a parallel and axial beam over a 40-foot length. In practice, because of waveguide flange interferences, these configurations could not be adopted and the "baba-abab" periodicity was chosen. Its only disadvantage is that over a 40-foot length, a beam entering on axis and parallel to it emerges parallel to the axis but with a net transverse displacement. The next 40-foot length produces the reverse effect and brings the beam back on axis. Hence this periodicity requires that klystrons be turned on and off in pairs so that over an 80-foot length the beam always remains on axis.

(c) Although it is not possible to compensate for the phase asymmetry, its effect can be reduced by causing the output coupler of a section to cancel part of the deflection created by the input coupler. Because the phase shift $\Delta\varphi$ appears to be in the direction of power flow, this reduction in net deflection can be obtained by having the input and output waveguide feeds on the same side. This remedy does not achieve total cancellation because the values of $\left(\frac{\Delta\varphi}{2a}\right)_{in}$ and $\left(\frac{\Delta\varphi}{2a}\right)_{out}$ differ by 30 to 40 percent in the constant-gradient structure.

IV. FABRICATION TECHNIQUES

A number of techniques of fabricating disk-loaded waveguide which meet the close tolerances necessary to establish the correct phase and group velocities have been explored at Stanford. Of the many methods considered, only three have been used to construct accelerator sections, namely, shrinking, electroforming, and brazing. While the shrinking method (2) was used at Stanford to construct the original 300-foot, 1-BeV accelerator (Mark III), it is now considered unsatisfactory when compared to the other two techniques.

Extensive work with electroforming and brazing has demonstrated that satisfactory disk-loaded waveguide sections can be made by either of these techniques. The specification for maximum phase shift excursions at any point along the axis of a 10-foot accelerator section is $\pm$ 2.5°. This corresponds to a mechanical tolerance of $\pm$ 0.00005 inch for 2b; $^{+\ 0.0002}_{-\ 0.0000}$ for 2a; $\pm$ 0.001 for d; $\pm$ 0.0002 for t; and $\pm$ 0.0005 for ρ (see Fig. 4). It is evident from these tolerances that special techniques must be utilized if they are to be achieved economically.

The most exacting of the tolerances is the $\pm$ 0.00005 inch required for the 2b dimension. This is achieved by machining the parts that go into the assembly to a tolerance of $^{+\ 0.0002\ \text{inch}}_{-\ 0.0000\ \text{inch}}$. It is not sufficient simply to air-condition the room in which these parts are made; it is also essential that a temperature-controlled cutting solution be flowed over the part during the time it is being machined. Hence, these parts are machined in an air-conditioned room and with a coolant oil which is controlled within a quarter of a degree Centigrade. After the assembly

is completed, the equivalent of the 0.00005-inch tolerance is achieved by making slight deformations in the wall of each cavity as described below. This procedure can be used with both the brazing and the electroforming methods of fabrication.

Satisfactory sections have been obtained with both the electroforming and brazing techniques. However, extensive studies have indicated that brazing is the preferable way of fabricating the 10,000 feet of disk-loaded waveguide. The preference for brazing arises primarily from the higher degree of flexibility inherent in this method; it requires only a few hours to complete a brazed assembly, whereas it takes nine days to complete an electroformed assembly. It is significant to note that for the large scale production required for a 10,000-foot accelerator, the cost of the electroforming technique is the same as the cost of the brazing technique within the accuracy of the cost estimates. Descriptions of both fabrication techniques follow.

Figure 31 shows an exploded view of the parts used for electroforming, together with a completed piece of disk-loaded waveguide made by this process. The first step in the electroforming method of fabrication is the assembly of a 10-foot array consisting of the copper disks and aluminum spacers shown in the figure. After the parts are assembled in a V-block, a mandrel is inserted through the holes and is used to hold the assembly together. The assembly work is carried out under water to assure that the hydrostatic pressure is equalized, hence reducing the probability of solution leakage. After assembly, the array is chemically cleaned and processed, and a thickness of 3/8 inch of copper is electroformed over it. Figure 32 shows the completed assembly in a copper sulfate electroforming bath. During this procedure, the mandrel is held

horizontally with the assembly half-submerged in the solution. During the plating, the assembly is rotated at approximately 30 rpm. An agate burnisher rides back and forth, continuously smoothing the surface of the plated copper. After the outer wall has been electroformed, the aluminum spacers are removed by etching in a sodium hydroxide solution. This procedure yields an all-copper disk-loaded waveguide fabricated to very close dimensions. A comparison of the crystalline structure of copper electroformed by this technique with that of OFHC copper produced by the usual mill fabricating procedure shows that the metallurgical properties are very similar. Electroformed copper as it comes from the bath has a surface finish of six micro-inches. Nine days are required to deposit the 3/8-inch wall thickness. Electroforming has been used to produce a number of 10-foot disk-loaded waveguide sections which have exhibited excellent characteristics.

The study of various brazing possibilities has led to the development of a new type of furnace. The essential features of this furnace are a moving ring burner which is fired by an oxygen-hydrogen flame, and a water-cooled chamber containing a reducing atmosphere in which the section can cool.

The essential features of the flame furnace are illustrated in Fig. 33. This illustration shows a 10-foot section nearing the completion of the brazing cycle. The procedure is carried out by first stacking the parts in the V-block which is shown at the right. The brazing alloy, which is a silver-copper eutectic melting at 783°C, is inserted at each joint in the form of thin washers. The stacking of the unit parts shown in Fig. 34 is carried

out while the V-block is at a 75° angle to the vertical. After the stacking is completed, the mandrel is inserted through the assembly and the end clamped by a spring-loaded mechanism. After the assembly is clamped, the V-block is tilted to the vertical position and the assembly is then transferred into the furnace by means of a jib crane. At the time the assembly is transferred to the furnace, the water-cooled cylinder D is in the fully raised position, and the assembly is attached to the metal tube E which serves to support the 10-foot section. The disk-loaded section then hangs as a free "plumb bob." Any swinging motion is damped by means of the water baffle assembly F. After the section is suspended, the split ring burner G is closed around the disk-loaded waveguide A. The burner is then raised to the uppermost end of the disk-loaded waveguide and the oxygen-hydrogen burner is ignited. When the melting point of the brazing alloy is reached, the ring burner together with the cylinder D is caused to move down the 10-foot section by means of lead screw sets H and J. Lead screw set J drives the cylinder, and lead screw set H drives the ring burner. Oxidation of the interior of the disk-loaded waveguide section is prevented by flowing a reducing gas through tube E. Reducing gas also flows into the cylinder D, providing a reducing atmosphere for the exterior of the section. A period of 25 to 30 minutes is required from the initiation of the heating cycle to its completion. The section is ready for removal from the furnace two and one-half hours after the heating cycle is finished.

Figure 35 shows the connection of the 10-foot assembly to its supporting tube and the "nose" plate which serves as a closure for the cylinder containing the reducing atmosphere in which the assembly is cooled. Figure 36 shows the furnace in operation with the flame on.

Input and output waveguides are made up as subassemblies. Each subassembly consists of the input or output waveguide, the end flange, and approximately eight inches of disk-loaded waveguide. These units are used in the stacking of a complete 10-foot section.

Figure 37 shows a view of the finished 10-foot accelerator section complete with the water cooling tubes which are attached by brazing in a separate furnace.

The required $\pm 2.5^{\circ}$ phase shift is achieved by a tuning operation which consists of indenting the walls of each cavity with four small dimples located at 90° about the axis. Figure 38 shows an overall view of the special tuning machine designed to tune the 10-foot accelerator sections while they are evacuated and at operating temperature. During the tuning procedure, the temperature is controlled to $\pm 0.1^{\circ}$F. The inside diameters of the cylinders comprising the cavity walls are machined oversize, leaving approximately a 10° phase margin in each cavity for tuning.

The tuning apparatus consists of the mechanism shown in Fig. 39 and a microwave bridge system shown in block diagram form in Fig. 40.(31) The bridge system consists of a commercially available phase measuring unit (Rantec Corporation, Calabasas, California) which compares the signal reflected by a calibrated reference branch with that of a test branch containing the accelerator section. This system utilizes the double side-band suppressed-carrier technique. This technique was selected over other possible methods because it provides the required accuracy of approximately 0.1° phase and is not sensitive to changes in attenuation of the test signal with respect to the reference signal. This insensitivity to changes in attenuation is important because the amplitude of the wave reflected

from the shorting plunger changes with the position of the plunger in the accelerator section. Additionally, a unit is required that gives a direct phase read-out, which permits the operator to monitor and control the amount of tuning required for each cavity. The mechanism by which the actual tuning is accomplished is illustrated in Fig. 39, and works in the following way. The movable carriage is indexed at the center of each cavity. Connected to the movable carriage is the shorting plunger. The plunger moves and indexes with the movable carriage by virtue of the steel tapes which couple to the rod that holds the expanding shorting plunger. The indentation of the cavities is accomplished by means of four hydraulically driven cylinders that push the 3/8-inch-diameter indenters into the wall of the cavity. The plunger driving rod is made of invar to insure dimensional stability in the location of the shorting plunger. Two O-ring seals allow the rod to move into and out of the evacuated section.

The tuning of the section begins with the installation of a 10-foot section in the machine, as shown in Fig. 38. The reference arm of the bridge circuit is then calibrated by means of a reference standard which consists of a precise, movable short that has three calibrating positions corresponding to the three Smith chart branches for the $\frac{2\pi}{3}$ disk spacing of the accelerator structure. After calibration by the reference branch, the tuning of the individual cavities can proceed.

For quality control purposes, additional low power measurements are made. The low power measurements are performed to check the phase of each cavity, the gradient along the axis, the match of each coupler, and the attenuation. Fig. 41 shows a typical phase plot made during the quality control check. Following this check, the sections are subjected to high

power output from a klystron (approximately 15 Mw peak and 15 kw average) primarily to release vacuum contaminants. In addition, the phase shift and attenuation are checked as a function of power level.

Figure 42 shows a 40-foot segment comprised of four of the sections. This is the fundamental module used in the construction of the machine. The sections are located on the 40-foot unit within an accuracy of 0.010-inch. The 24-inch-diameter girder on which they are mounted serves both as a support and as an evacuated "light pipe" through which light from a laser source at one end of the two-mile accelerator can be used to align the girders (and the attached accelerator sections) within an accuracy of ±0.040 inch.

ACKNOWLEDGMENT

The authors would like to thank those members of the Stanford Linear Accelerator Center staff who have contributed to the work reported here. In particular, they wish to acknowledge the contributions of O. Altenmueller, B. Kendall, A Kirshbaum, C. Kruse, J. Abraham, L. Cain, R. Chapton, M. Heinz, D. Jeong, A. Lisin, F. Patton, J. A. Pope, C. Rasmussen, D. Robertson, D. Rogers, K. Skarpaas, H. Soderstrom, and B. Stillman.

REFERENCES

1. Ginzton, E.L., Hansen, W.W., and Kennedy, W.R. A linear electron accelerator. Rev. Sci. Instr. 19, 89 (1948).

2. Chodorow, M., et al. Stanford high-energy linear electron accelerator (Mark III). Rev. Sci. Instr. 26, 134 (1955).

3. Neal, R.B. Theory of the constant gradient linear electron accelerator. ML Report No. 513 W.W. Hansen Laboratories of Physics, Stanford University, Stanford, California (1958); and Comparison of the constant gradient and uniform accelerator structures. M Report No. 259 (1961), Stanford Linear Accelerator Center, Stanford University, Stanford, California.

4. These phenomena were called to our attention by J. E. Leiss of the U.S. National Bureau of Standards (private communication). Calculations made by Leiss have been confirmed by experimental results at Stanford and elsewhere.

5. Kelliher, M.G. and Beadle, R. Pulse shortening in electron linear accelerators. Nature 187, 1099 (1960).

6. Crowley-Milling, M.C., Jarvis, T.R., Miller, C.W., and Saxon, G. Pulse shortening in electron linear accelerators. Nature 191, 483 (1961).

7. Linear electron accelerator studies. ML Report No. 581, W.W. Hansen Laboratories of Physics, Stanford University, Stanford, California (1959).

8. Wilson, P.B. A study of beam-blow-up in electron linacs. HEPL Report No. 297, Hansen Laboratories of Physics, Stanford University, Stanford, California (1963).

9. Altenmueller, O.H., Larsen, R.R., and Loew, G.A. Investigations of traveling-wave separators for the Stanford two-mile linear accelerator. Rev. Sci. Instr. 35, 438 (1964).

10. Altenmueller, O.H., Larsen, R.R., and Loew, G.A. Properties and applications of the TM_{11} mode in cylindrical disk-loaded waveguide. SLAC Internal Document, Stanford Linear Accelerator Center, Stanford University, Stanford, California (1964).

11. Altenmueller, O.H., Larsen, R.R., and Loew, G.A. Investigations of traveling-wave separators for the Stanford two-mile linear accelerator. SLAC Report No. 17, Stanford Linear Accelerator Center, Stanford University, Stanford, California (1963).

12. Kingsland, R. Hughes Aircraft Company, Fullerton, California (private communications).

13. Ginzton, E.L. "Microwave measurements." McGraw-Hill, New York, 1957

14. Gallagher, W.J. Measurement techniques for periodic structures. M Report No. 205, Stanford Linear Accelerator Center, Stanford University, Stanford, California (1960).

15. Robson, P.N. Fourier series representations of dispersion curves for circular corrugated waveguide used in traveling-wave linear accelerators. Report No. 5105, Metropolitan-Vickers Electrical Company, Ltd., Manchester, England (1956).

16. Ayers, W.R., Chu, E.L., and Gallagher, W.J. Measurements of interaction impedance in periodic circuits. ML Report No. 403, W.W. Hansen Laboratories of Physics, Stanford University, Stanford, Calif. (1957).

17. Linear electron accelerator studies and proposed two-mile accelerator project. M Report No. 246, Stanford Linear Accelerator Center, Stanford University, Stanford, California (1961).

18. Mallory, K.B. A source of error in the use of slope detection for perturbation measurements. IRE Trans. Microwave Theory Tech. MTT-10, 146 (1962).

19. Hirel, Renée. Space-harmonic content of the $2\pi/3$ accelerator structure. M Report No. 270, Stanford Linear Accelerator Center, Stanford University, Stanford, California (1961).

20. Deschamps, G.A. Determination of reflection coefficients and insertion loss of a wave-guide junction. J. Appl. Phys. 24, 1046 (1953).

21. Mallory, K.B. A comparison of the predicted and observed performances of a billion-volt electron accelerator. HEPL Report No. 46, W.W. Hansen Laboratories of Physics, Stanford University, Stanford, California (1955); p. 68 et seq.

22. Belbeoch, R. Problèmes poses par l'adaption du coupleur d'entree d'une structure en guide charge par des iris. Rapport LAL-13, Laboratoire de l'accelerateur lineaire, Orsay, France (1961).

23. Kyhl, R. (private communication).

24. Borghi, R. (private communication).

25. Westbrook, E. Microwave impedance matching of feed waveguides to the disk-loaded accelerator structure operating in the $2\pi/3$ mode. SLAC Internal Report, Stanford Linear Accelerator Center, Stanford University, Stanford, California (1963).

26. Borghi, R. and Jeong, D. Gradient corrections for the SLAC accelerating structure. SLAC Report No. 38, Stanford Linear Accelerator Center, Stanford University, Stanford, California (to be published).

27. Neal, R.B. Theory of the constant gradient linear electron accelerator. ML Report No. 513, W.W. Hansen Laboratories of Physics, Stanford University, Stanford, California (1958); p. 4, Eq. (3.6).

28. Neal, R.B. Comparison of the constant gradient and uniform accelerator structures. M Report No. 259, Stanford Linear Accelerator Center, Stanford University, Stanford, California (1961); p. 5, Eq. (7).

29. Helm, R.H. A note on coupler asymmetries in long linear accelerators. M Report No. 167, Stanford Linear Accelerator Center, Stanford University, Stanford, California (1960).

30. Helm, R.H. Effects of stray magnetic fields and rf coupler asymmetry in the two-mile accelerator with sector focusing. SLAC Report No. 20, Stanford Linear Accelerator Center, Stanford University, Stanford, California (1963).

31. Borghi, R., Patton, F., and Heinz, M. Phase velocity adjustment of the SLAC accelerating structure. SLAC Report No. 37, Stanford Linear Accelerator Center, Stanford University, Stanford, California (to be published).

LIST OF FIGURES

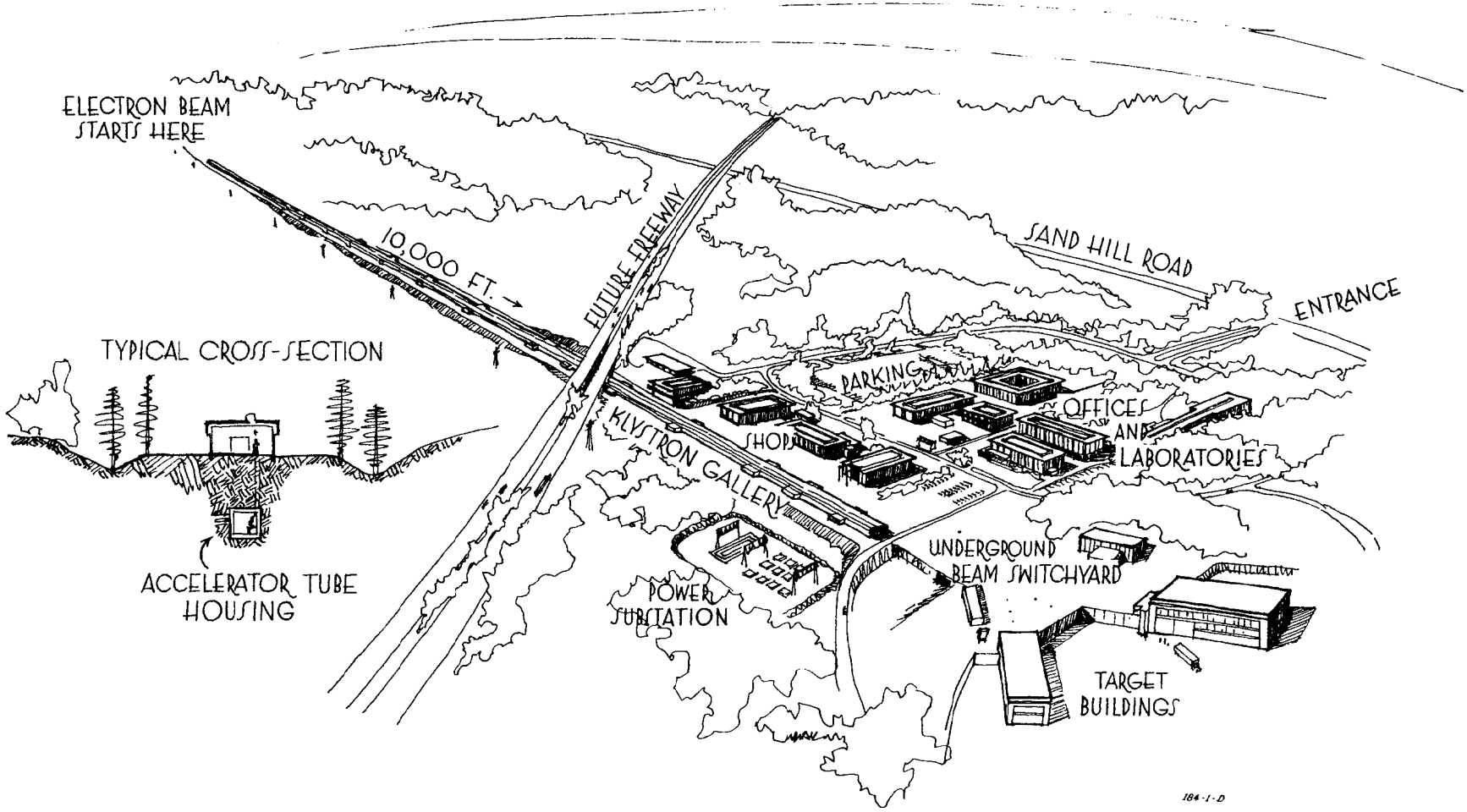
ELECTRON BEAM STARTS HERE
10,000 FT.
FUTURE FREEWAY
SAND HILL ROAD
ENTRANCE
TYPICAL CROSS-SECTION
PARKING
OFFICES AND LABORATORIES
SHOPS
KLYSTRON GALLERY
ACCELERATOR TUBE HOUSING
POWER SUBSTATION
UNDERGROUND BEAM SWITCHYARD
TARGET BUILDINGS
184-1-D

Figure 1

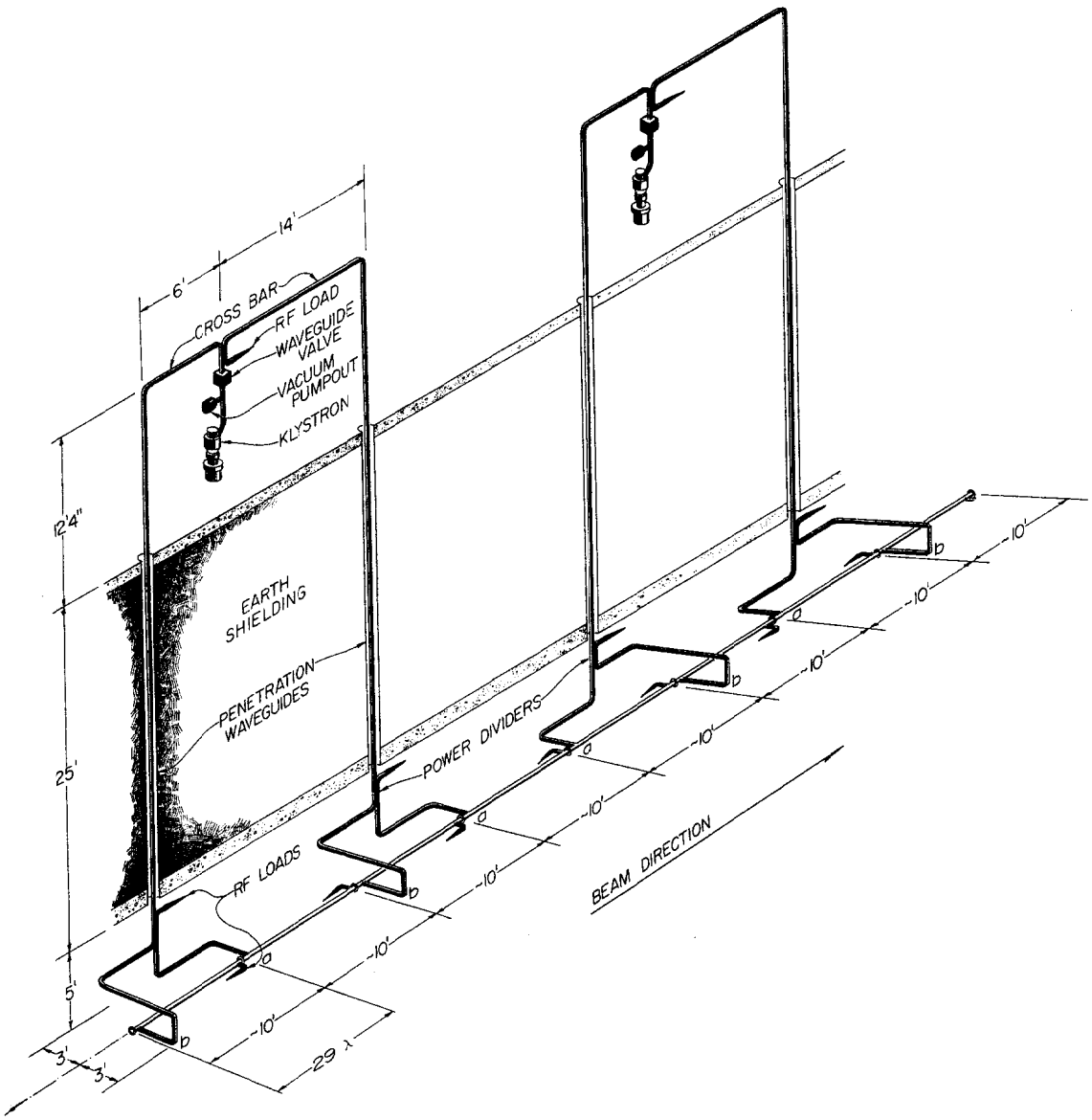
14'
6'
CROSS BAR
RF LOAD
WAVEGUIDE VALVE
VACUUM PUMPOUT
KLYSTRON
12'4"
EARTH SHIELDING
PENETRATION WAVEGUIDES
25'
POWER DIVIDERS
RF LOADS
5'
3'
3'
10'
10'
10'
10'
10'
10'
29 λ
BEAM DIRECTION
a
b

Figure 2

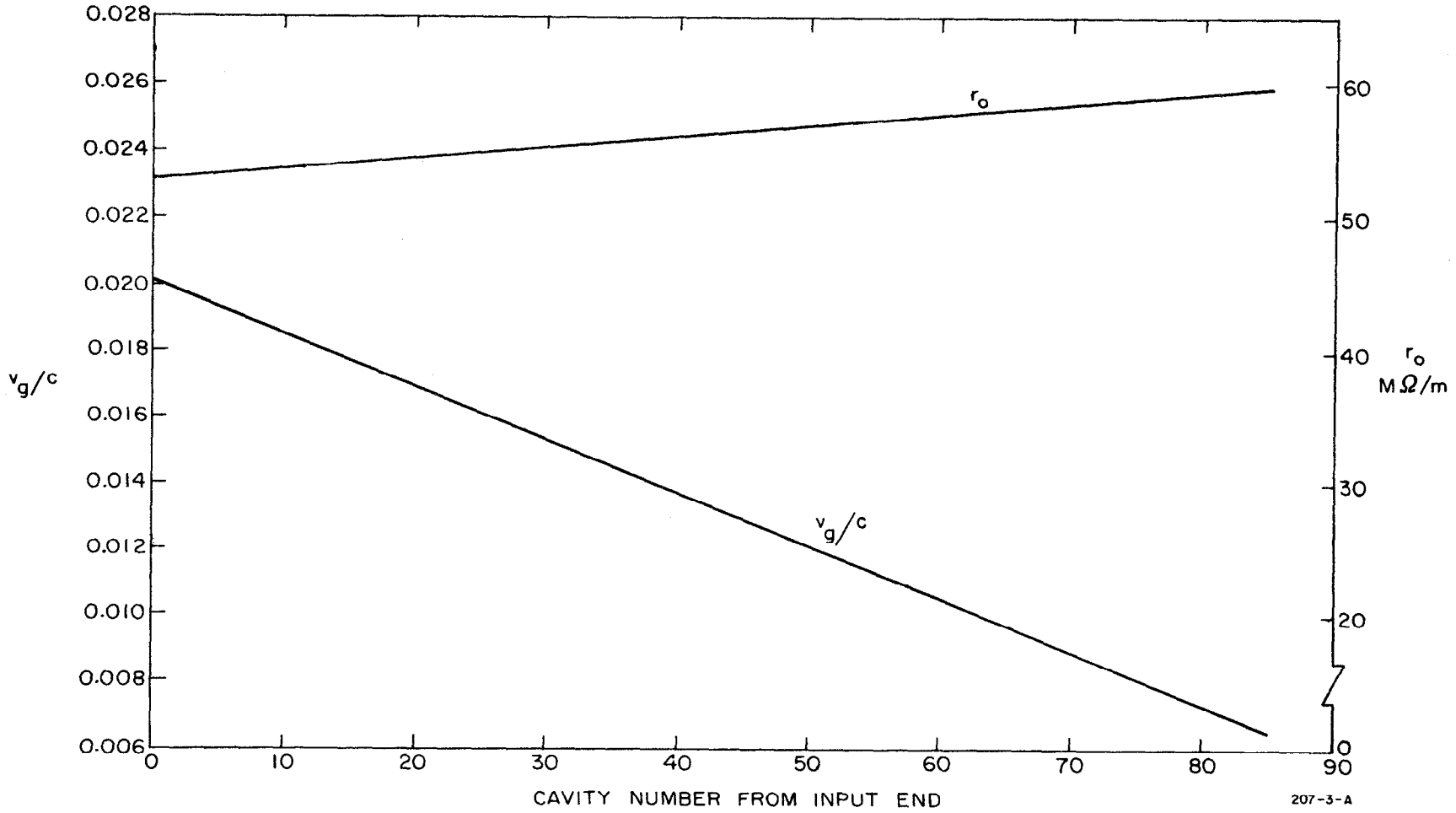
0.028
0.026
0.024
0.022
0.020
0.018
0.016
0.014
0.012
0.010
0.008
0.006
v_g/c
r_o
v_g/c
60
50
40
30
20
0
r_o
MΩ/m
0
10
20
30
40
50
60
70
80
90
CAVITY NUMBER FROM INPUT END
207-3-A

Figure 3

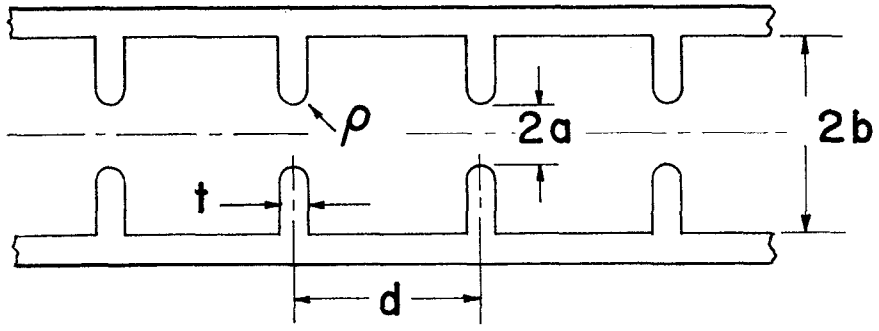

a) TWO UNIT CELLS

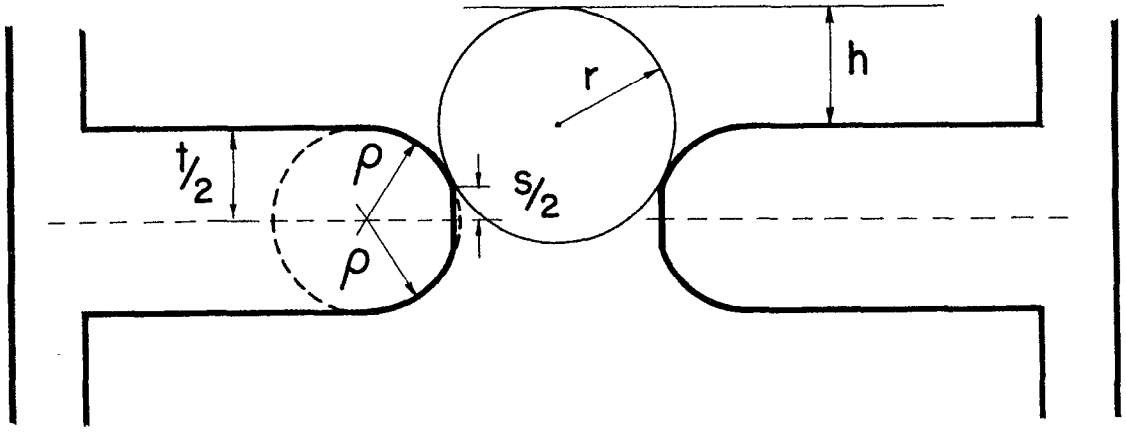

b) ILLUSTRATION OF DISK DIMENSIONS

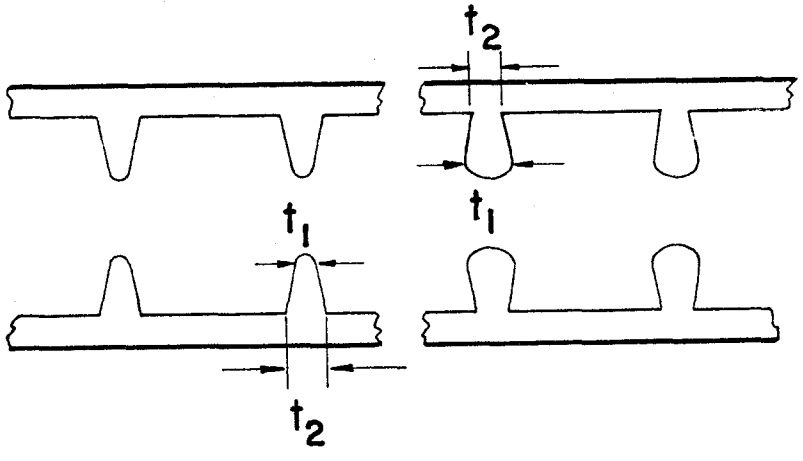

c) "CONICAL" AND "ANTICONICAL" DISKS

Figure 4

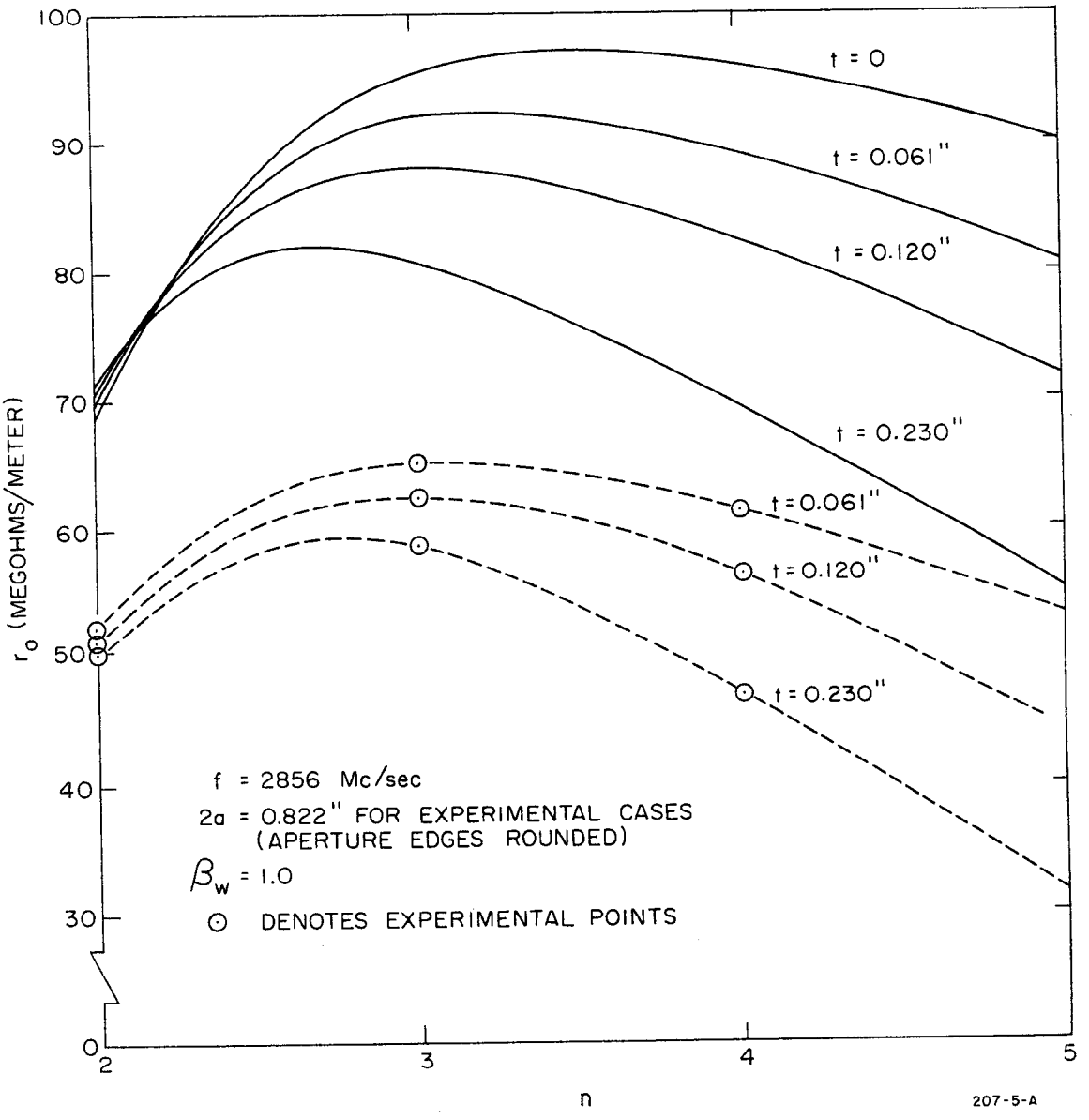
100
90
80
70
60
50
40
30
0
2
3
4
5
n
r_o (MEGOHMS/METER)
t = 0
t = 0.061"
t = 0.120"
t = 0.230"
t = 0.061"
t = 0.120"
t = 0.230"
f = 2856 Mc/sec
2a = 0.822" FOR EXPERIMENTAL CASES
(APERTURE EDGES ROUNDED)
β_w = 1.0
⊙ DENOTES EXPERIMENTAL POINTS
207-5-A

Figure 5

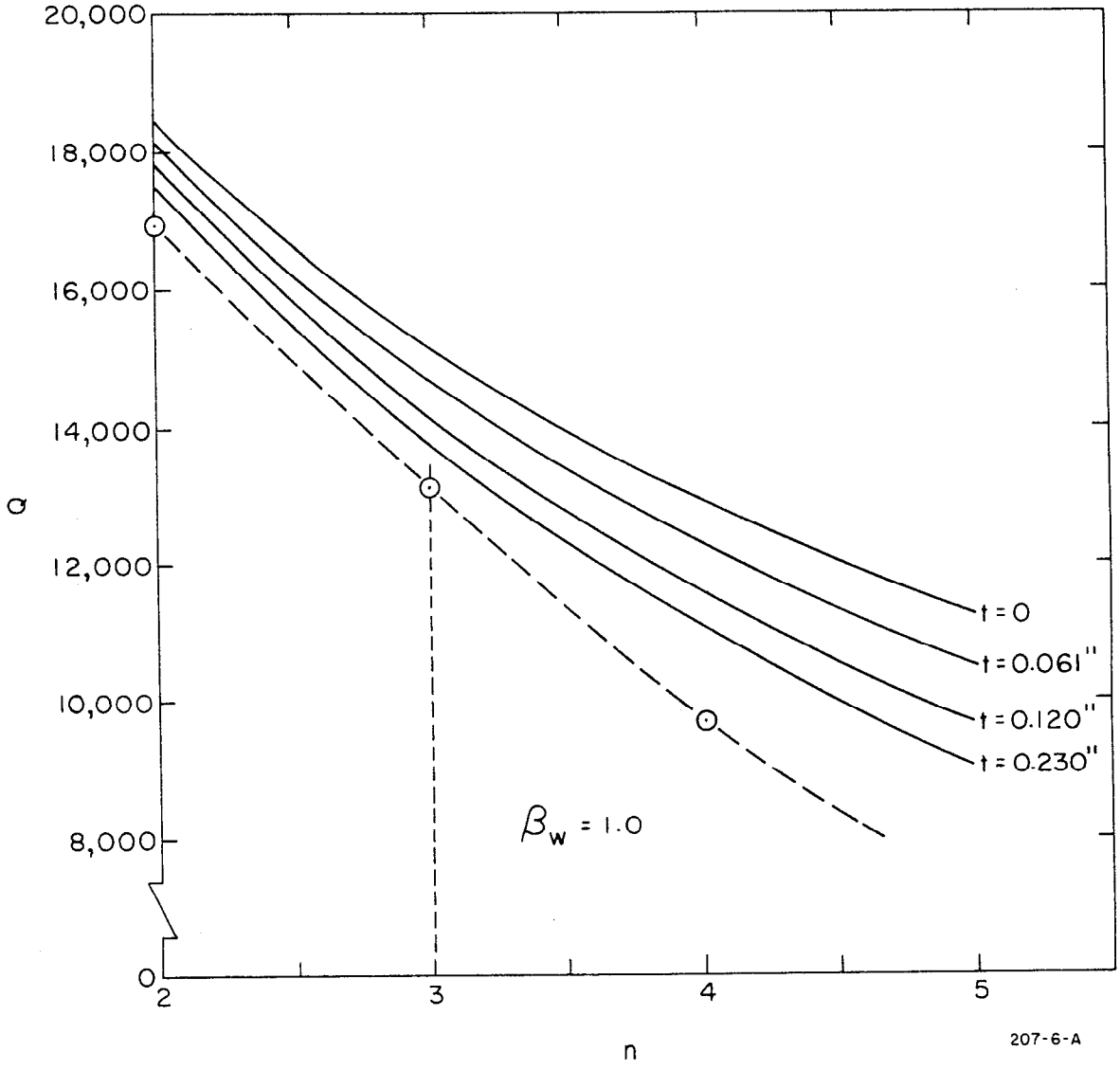
20,000
18,000
16,000
14,000
12,000
10,000
8,000
0
σ
2
3
4
5
n
t = 0
t = 0.061"
t = 0.120"
t = 0.230"
β_w = 1.0
207-6-A

Figure 6

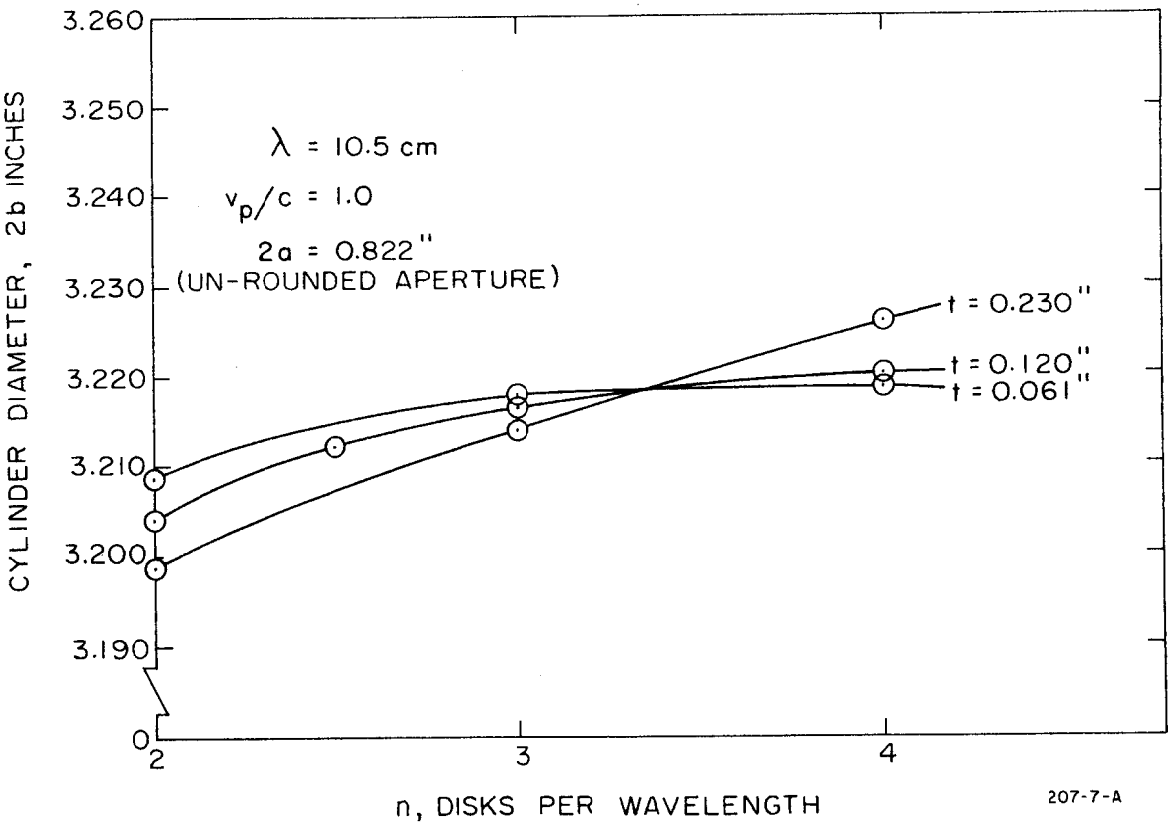
3.260
3.250
3.240
3.230
3.220
3.210
3.200
3.190
0
2
3
4
CYLINDER DIAMETER, 2b INCHES
n, DISKS PER WAVELENGTH
λ = 10.5 cm
v_p/c = 1.0
2a = 0.822"
(UN-ROUNDED APERTURE)
t = 0.230"
t = 0.120"
t = 0.061"
207-7-A

Figure 7

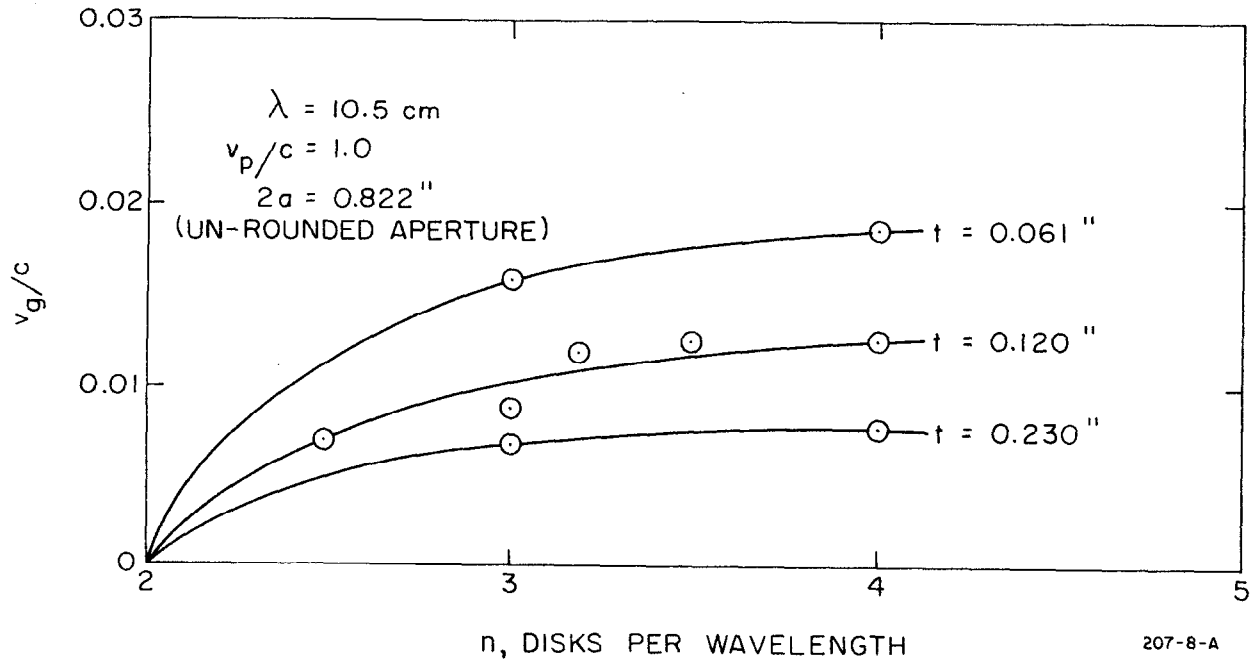
0.03
0.02
0.01
0
λ = 10.5 cm
v_p/c = 1.0
2a = 0.822"
(UN-ROUNDED APERTURE)
t = 0.061"
t = 0.120"
t = 0.230"
v_g/c
2
3
4
5
n, DISKS PER WAVELENGTH
207-8-A

Figure 8

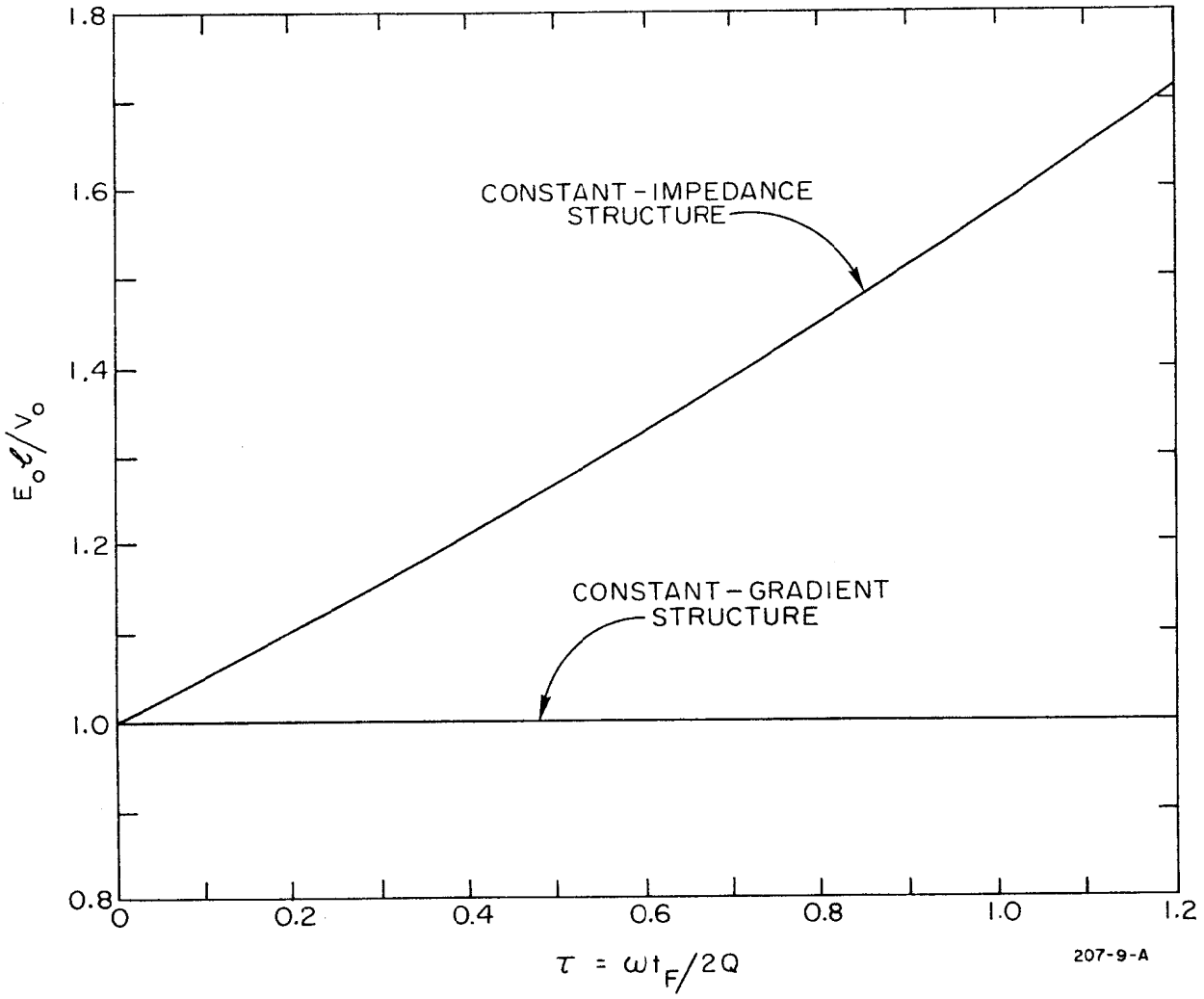
1.8
1.6
1.4
1.2
1.0
0.8
$E_o \ell / V_o$
CONSTANT-IMPEDANCE STRUCTURE
CONSTANT-GRADIENT STRUCTURE
0
0.2
0.4
0.6
0.8
1.0
1.2
$\tau = \omega t_F / 2Q$
207-9-A

Figure 9

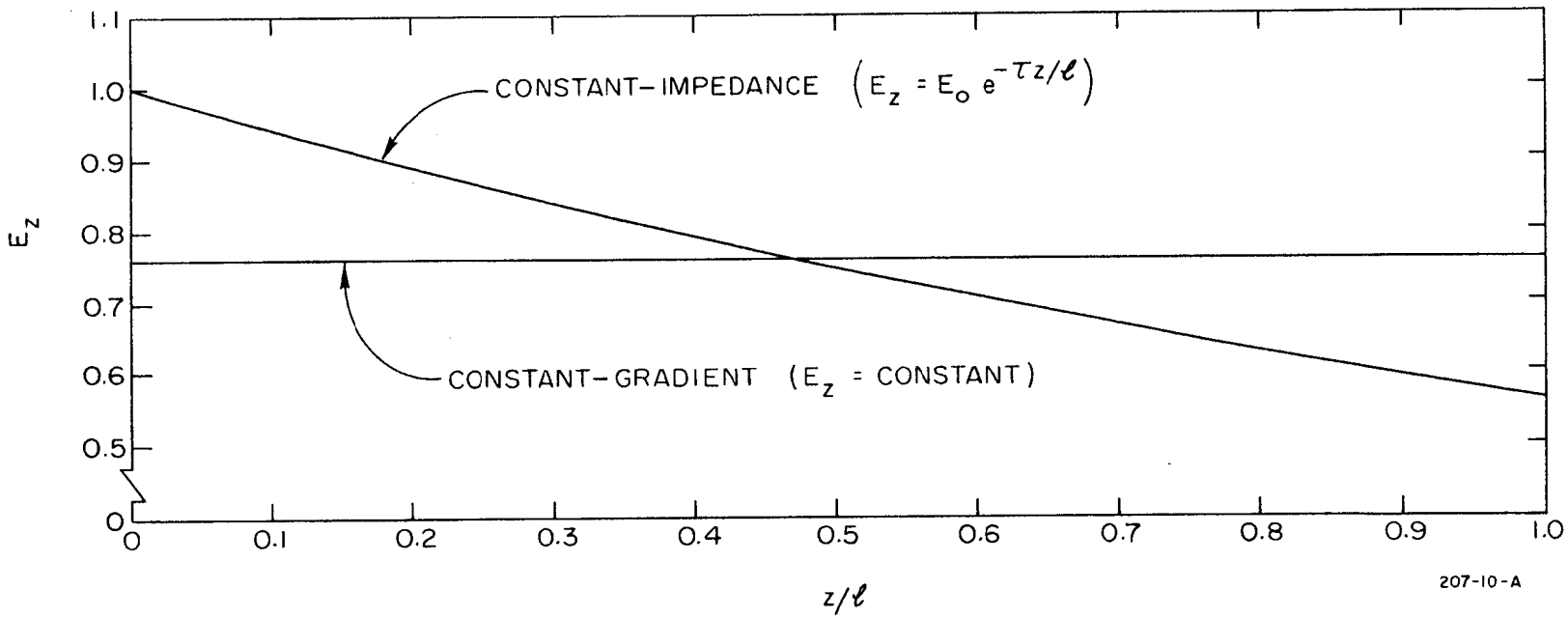
1.1
1.0
0.9
0.8
0.7
0.6
0.5
0
E_z
CONSTANT-IMPEDANCE $\left(E_z = E_o\, e^{-\tau z/\ell}\right)$
CONSTANT-GRADIENT (E_z = CONSTANT)
0
0.1
0.2
0.3
0.4
0.5
0.6
0.7
0.8
0.9
1.0
z/ℓ
207-10-A

Figure 10

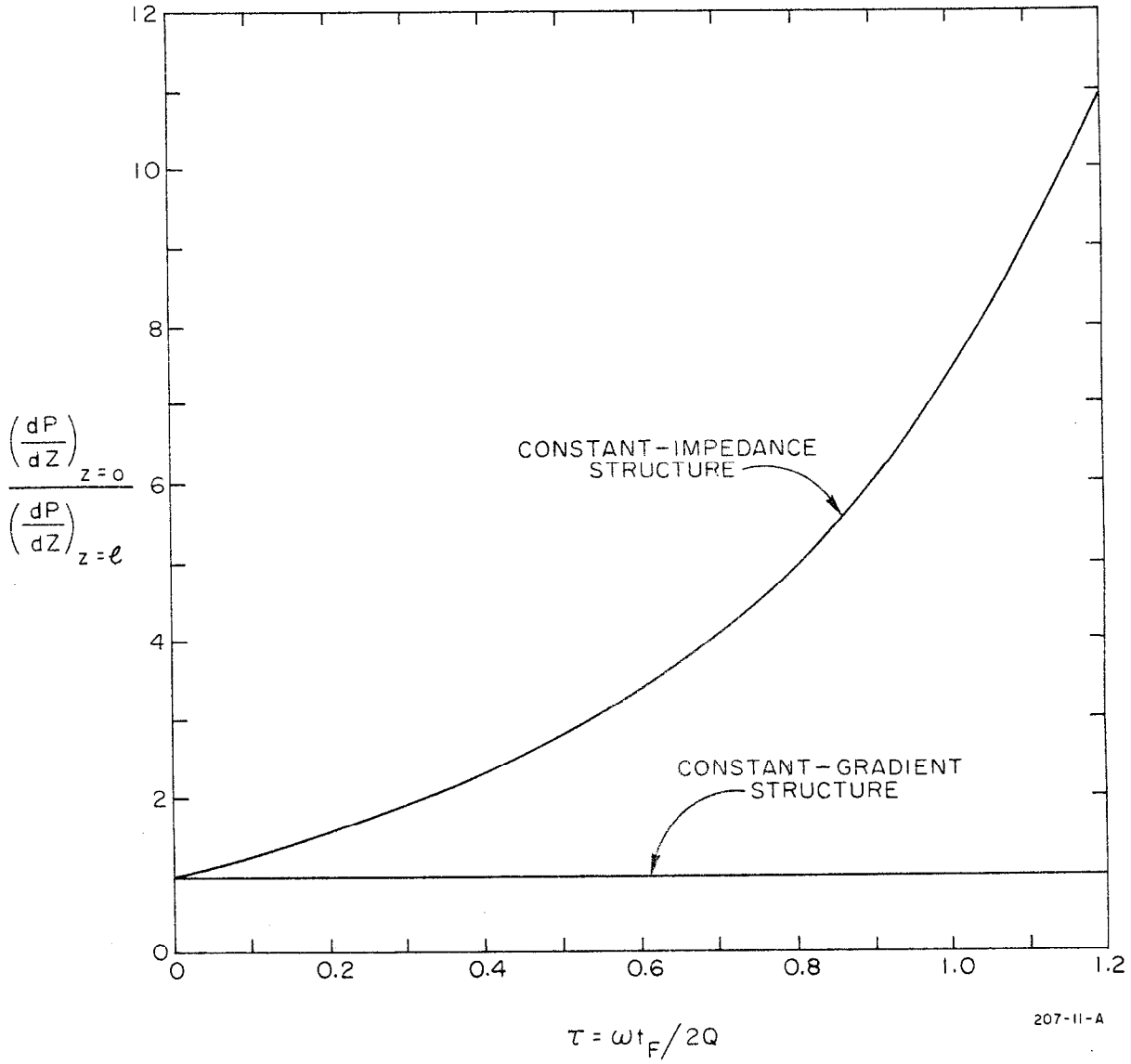
12
10
8
6
4
2
0
0
0.2
0.4
0.6
0.8
1.0
1.2
$\left(\frac{dP}{dZ}\right)_{z=0} \Big/ \left(\frac{dP}{dZ}\right)_{z=\ell}$
CONSTANT-IMPEDANCE STRUCTURE
CONSTANT-GRADIENT STRUCTURE
$\tau = \omega t_F / 2Q$
207-11-A

Figure 11

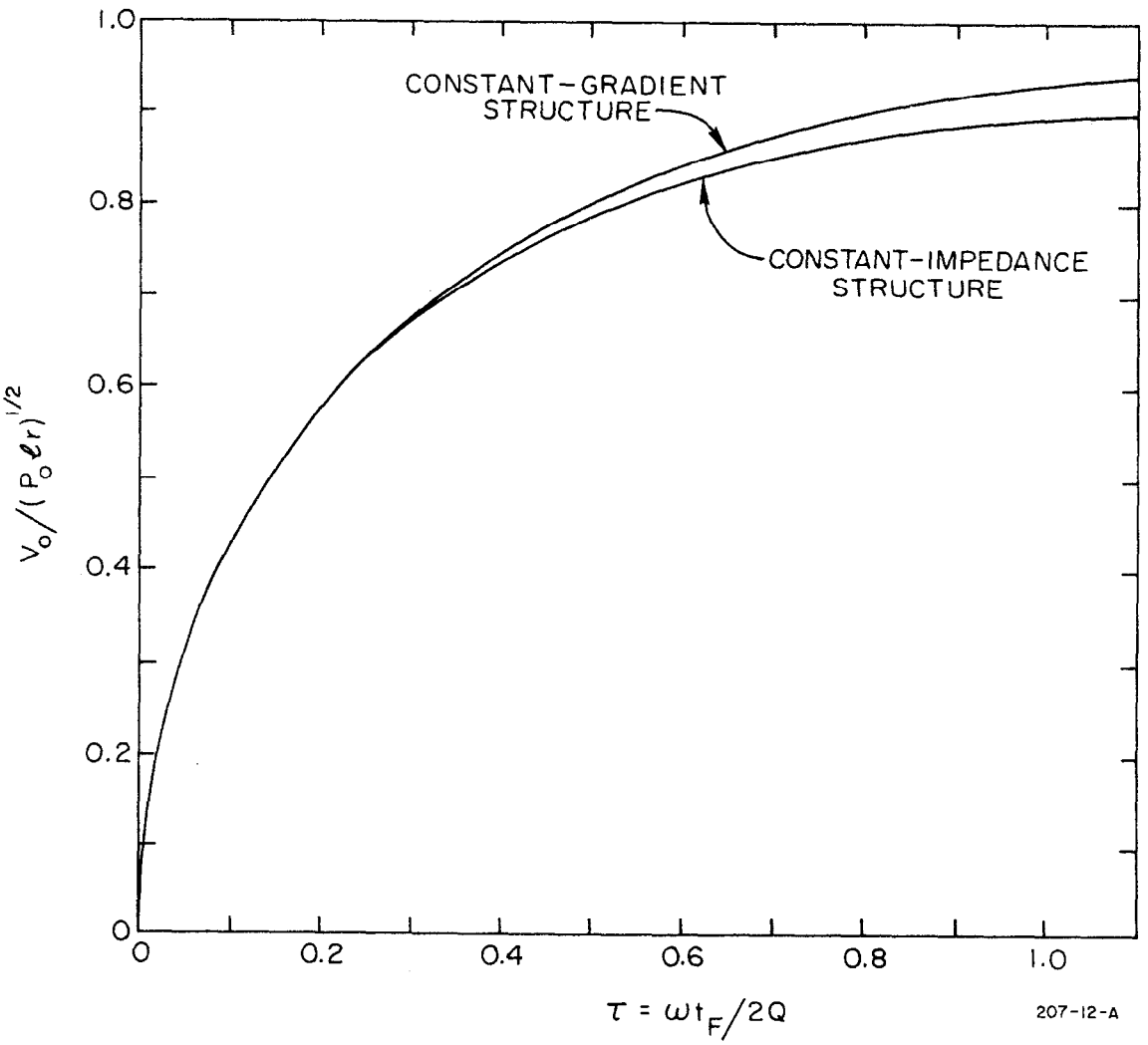
1.0
0.8
0.6
0.4
0.2
0
0
0.2
0.4
0.6
0.8
1.0
CONSTANT-GRADIENT STRUCTURE
CONSTANT-IMPEDANCE STRUCTURE
$V_o/(P_o \ell r)^{1/2}$
$\tau = \omega t_F/2Q$
207-12-A

Figure 12

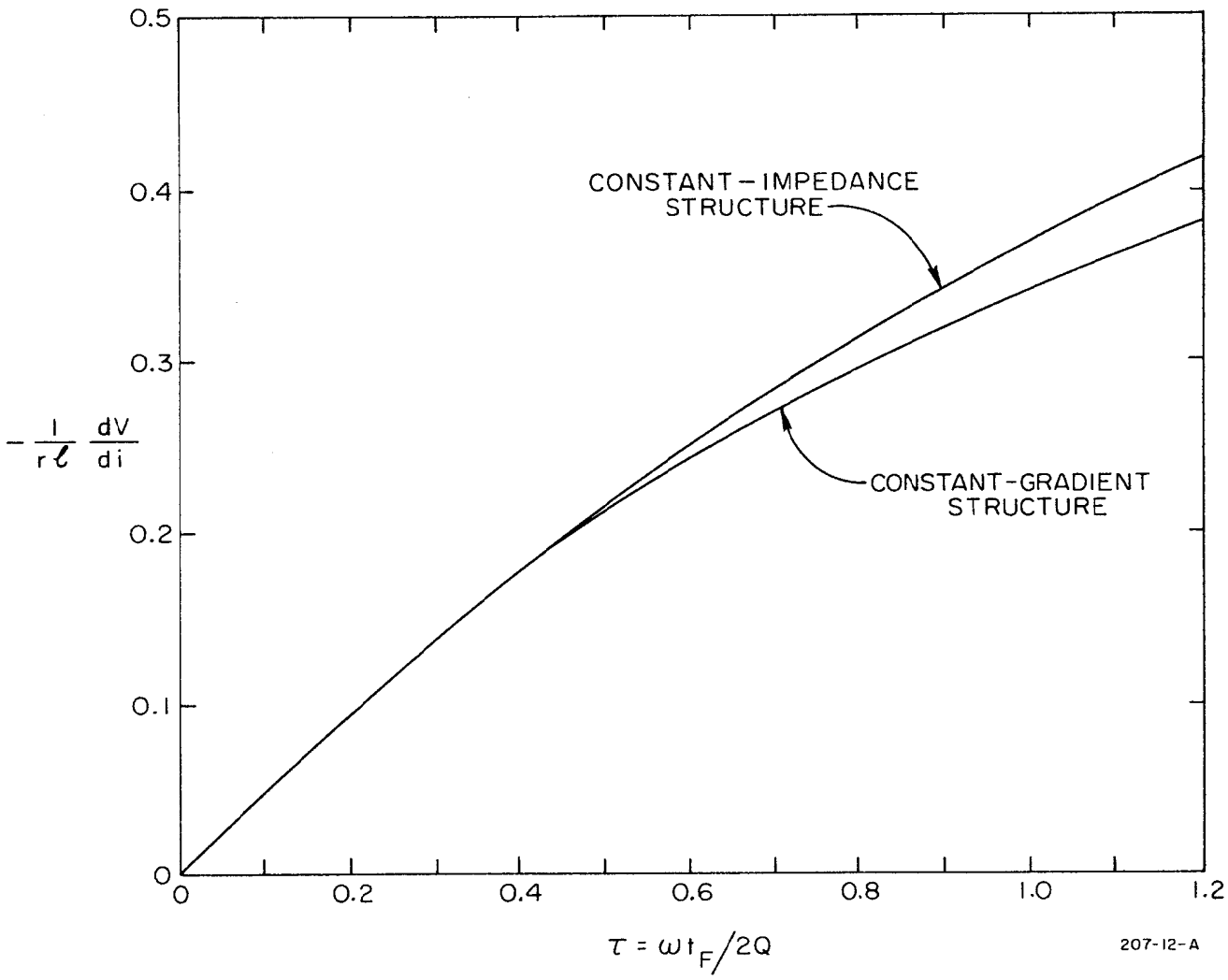
0.5
0.4
0.3
0.2
0.1
0
0
0.2
0.4
0.6
0.8
1.0
1.2
$-\frac{1}{r\ell}\frac{dV}{di}$
$\tau = \omega t_F/2Q$
CONSTANT-IMPEDANCE STRUCTURE
CONSTANT-GRADIENT STRUCTURE
207-12-A

Figure 13

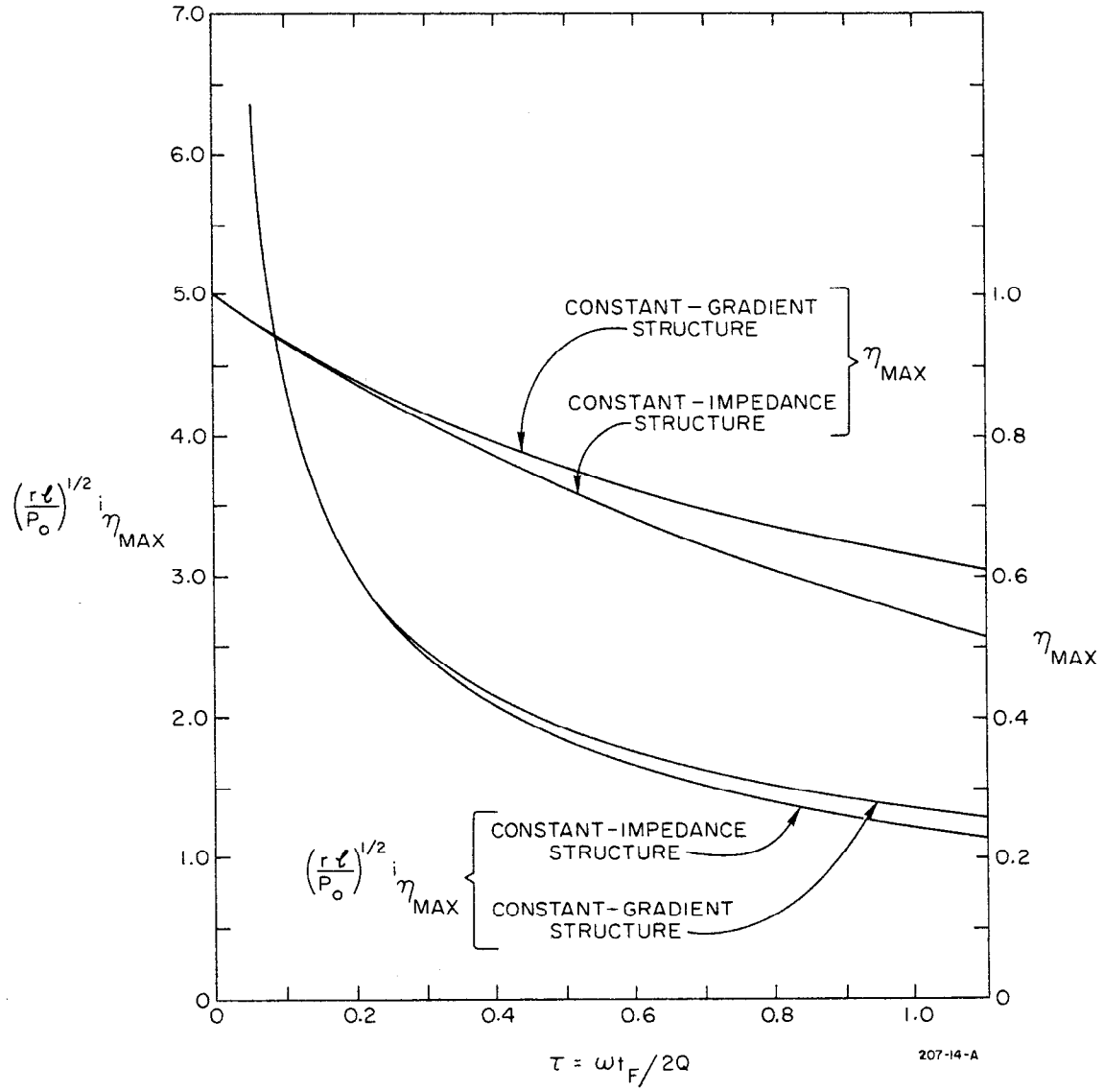
7.0
6.0
5.0
4.0
3.0
2.0
1.0
0
0
0.2
0.4
0.6
0.8
1.0
1.0
0.8
0.6
0.4
0.2
0
$\left(\frac{r\ell}{P_o}\right)^{1/2} i\eta_{MAX}$
η_{MAX}
CONSTANT – GRADIENT STRUCTURE
CONSTANT – IMPEDANCE STRUCTURE
η_{MAX}
$\left(\frac{r\ell}{P_o}\right)^{1/2} i\eta_{MAX}$
CONSTANT-IMPEDANCE STRUCTURE
CONSTANT-GRADIENT STRUCTURE
$\tau = \omega t_F/2Q$
207-14-A

Figure 14

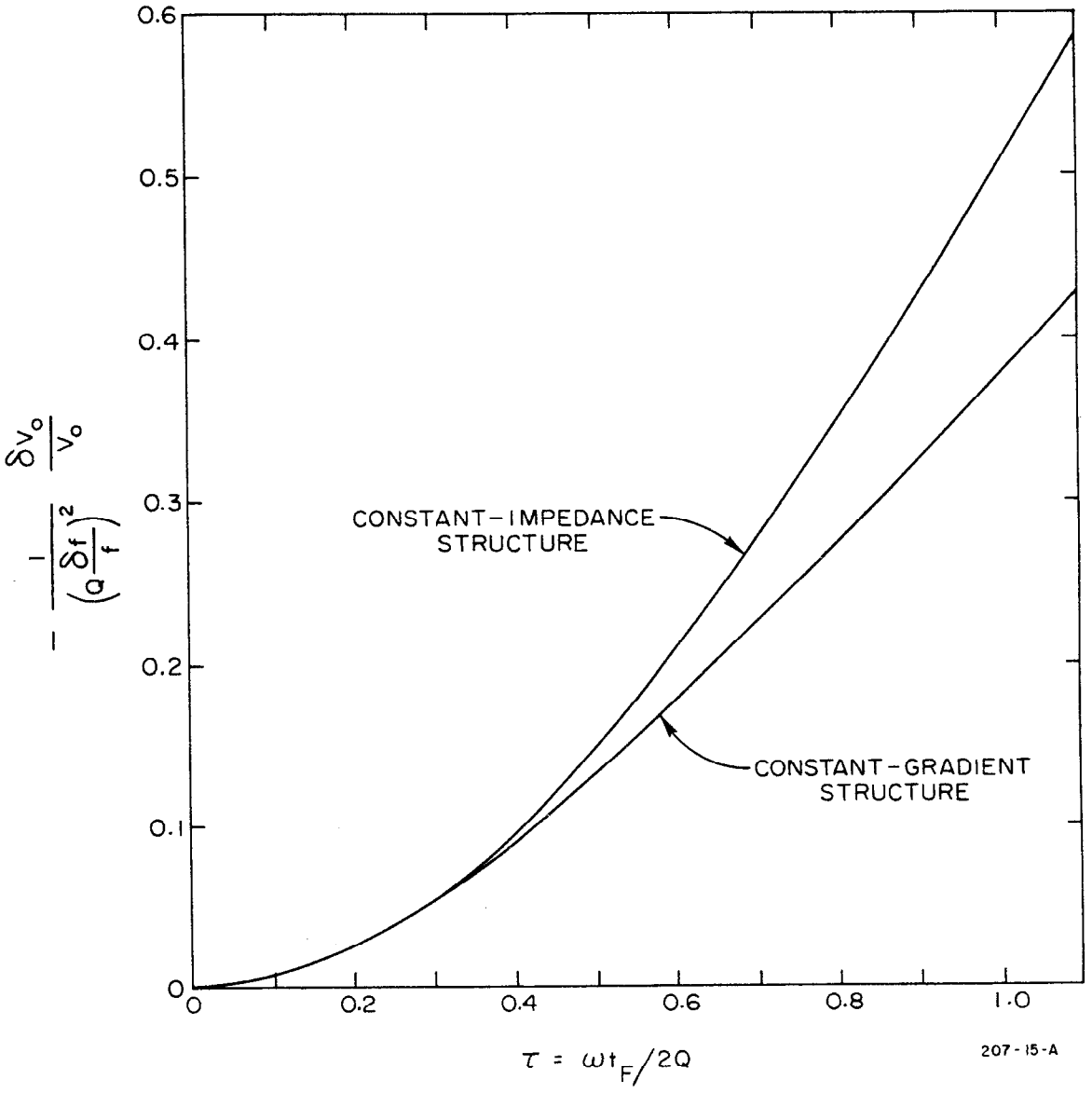
0.6
0.5
0.4
0.3
0.2
0.1
0
0
0.2
0.4
0.6
0.8
1.0
$\frac{\delta V_o}{V_o}$
$\frac{1}{1-\left(Q\frac{\delta f}{f}\right)^2}$
CONSTANT-IMPEDANCE STRUCTURE
CONSTANT-GRADIENT STRUCTURE
$\tau = \omega t_F/2Q$
207-15-A

Figure 15

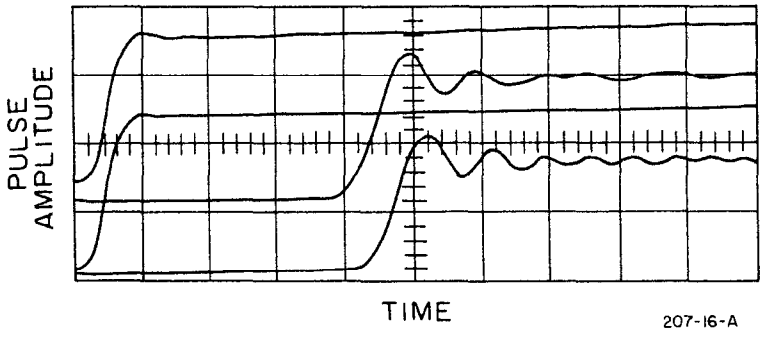

Figure 16

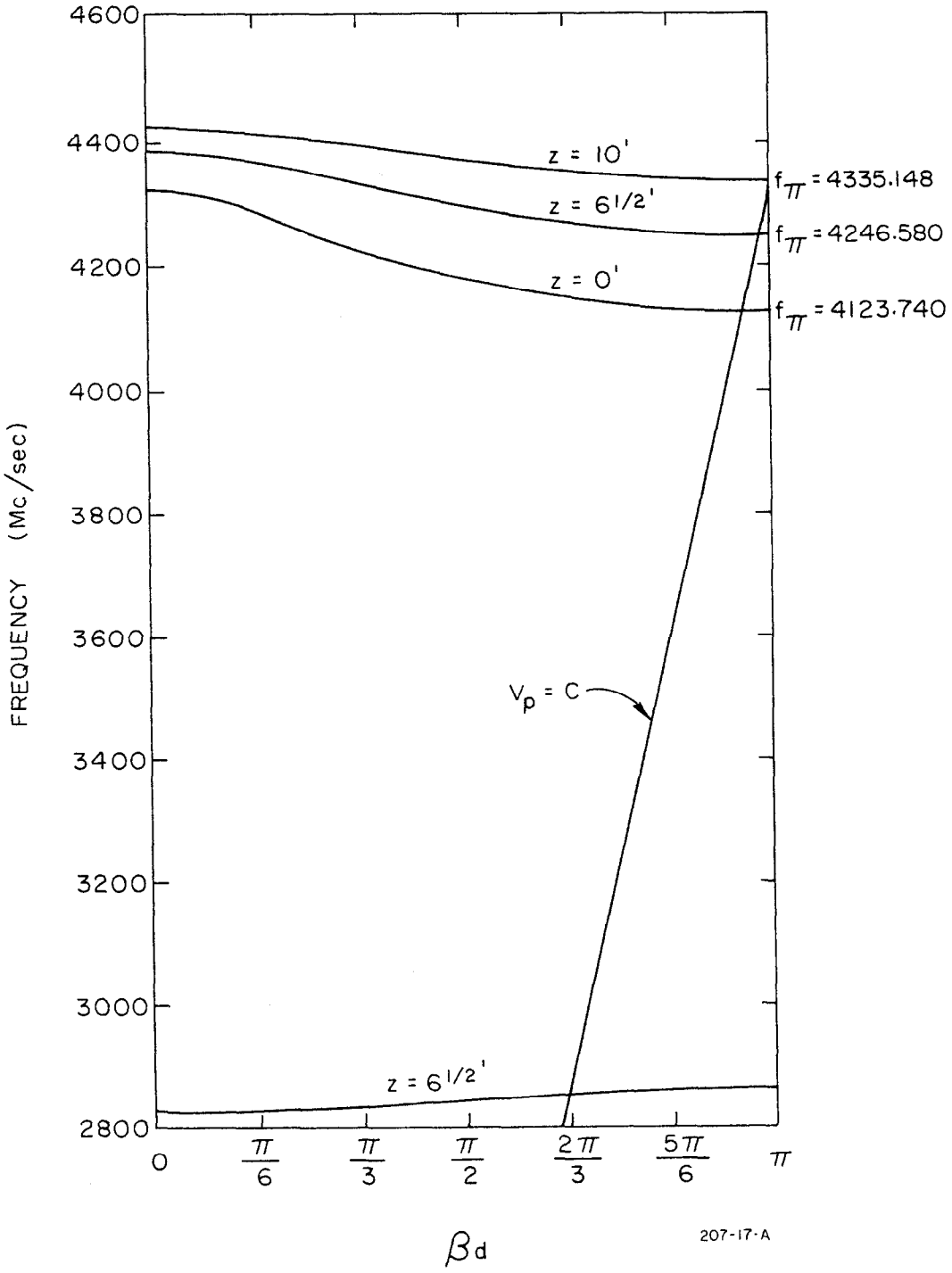
4600
4400
4200
4000
3800
3600
3400
3200
3000
2800
FREQUENCY (Mc/sec)
z = 10'
z = 6 1/2'
z = 0'
f_π = 4335.148
f_π = 4246.580
f_π = 4123.740
V_p = C
z = 6 1/2'
0
$\frac{\pi}{6}$
$\frac{\pi}{3}$
$\frac{\pi}{2}$
$\frac{2\pi}{3}$
$\frac{5\pi}{6}$
π
βd
207-17-A

Figure 17

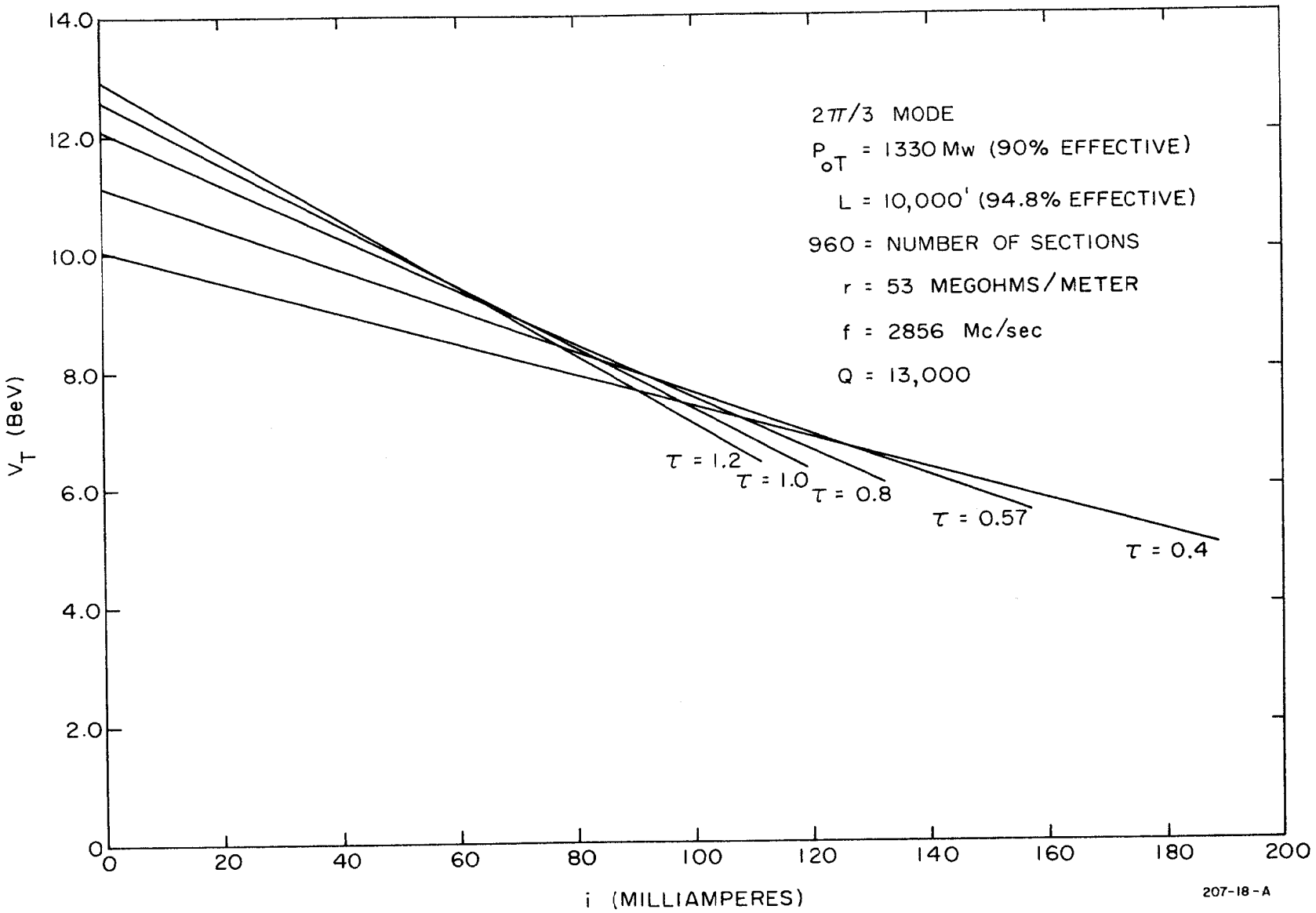
14.0
12.0
10.0
8.0
6.0
4.0
2.0
0
V_T (BeV)
0
20
40
60
80
100
120
140
160
180
200
i (MILLIAMPERES)
$2\pi/3$ MODE
P_{oT} = 1330 Mw (90% EFFECTIVE)
L = 10,000' (94.8% EFFECTIVE)
960 = NUMBER OF SECTIONS
r = 53 MEGOHMS/METER
f = 2856 Mc/sec
Q = 13,000
τ = 1.2
τ = 1.0
τ = 0.8
τ = 0.57
τ = 0.4
207-18-A

Figure 18

FORWARD-WAVE STRUCTURES

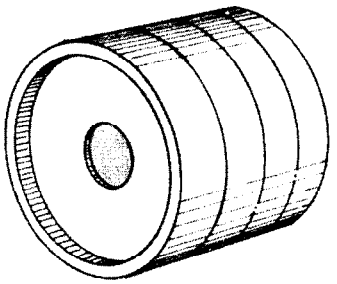

1. DISK-LOADED STRUCTURE

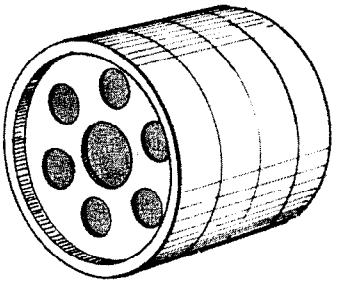

2. VENTILATED STRUCTURE

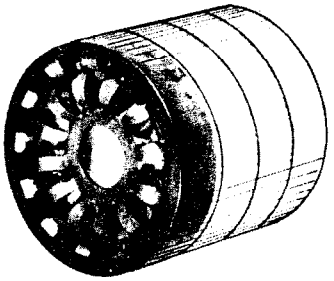

3. CENTIPEDE STRUCTURE

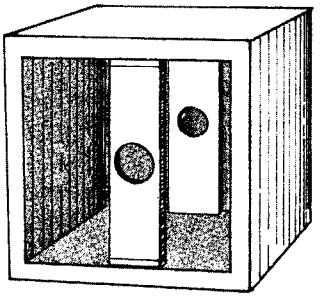

4. RECTANGULAR SLAB

BACKWARD-WAVE STRUCTURES

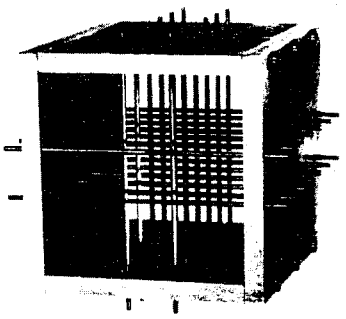

5. "JUNGLE GYM"

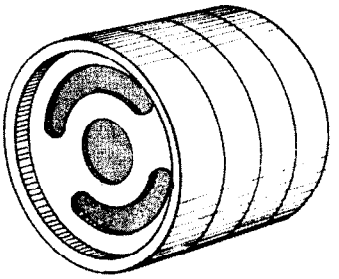

6. SLOTTED DISK STRUCTURE

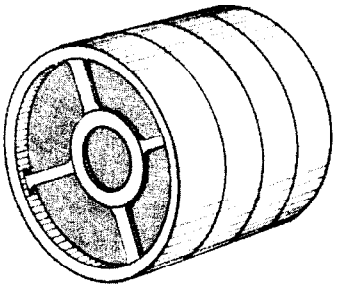

7. RING & BAR STRUCTURE

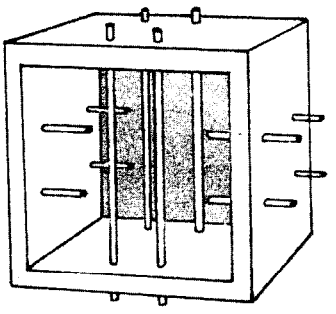

8. LOADED EASITRON

Figure 19

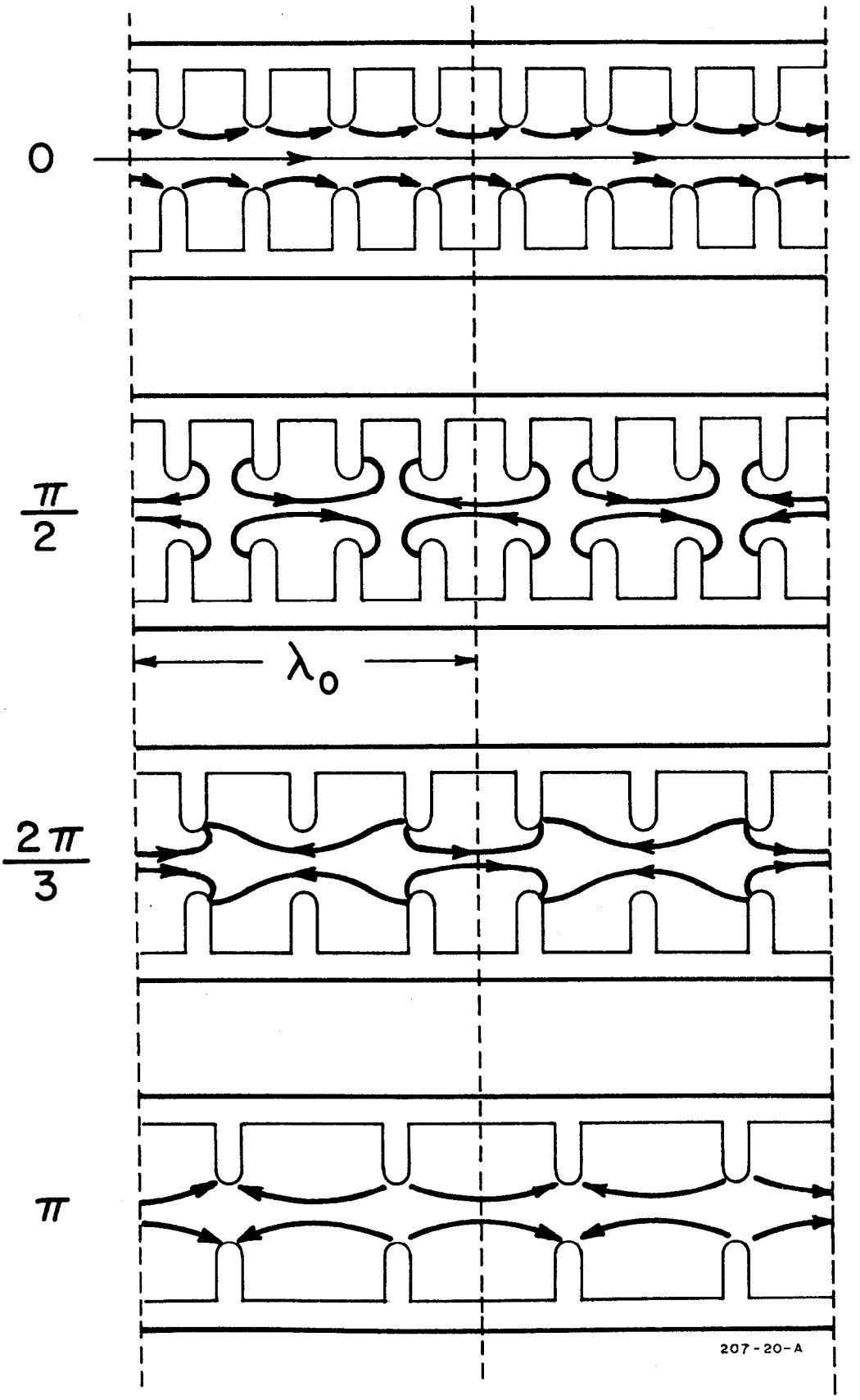

Figure 20

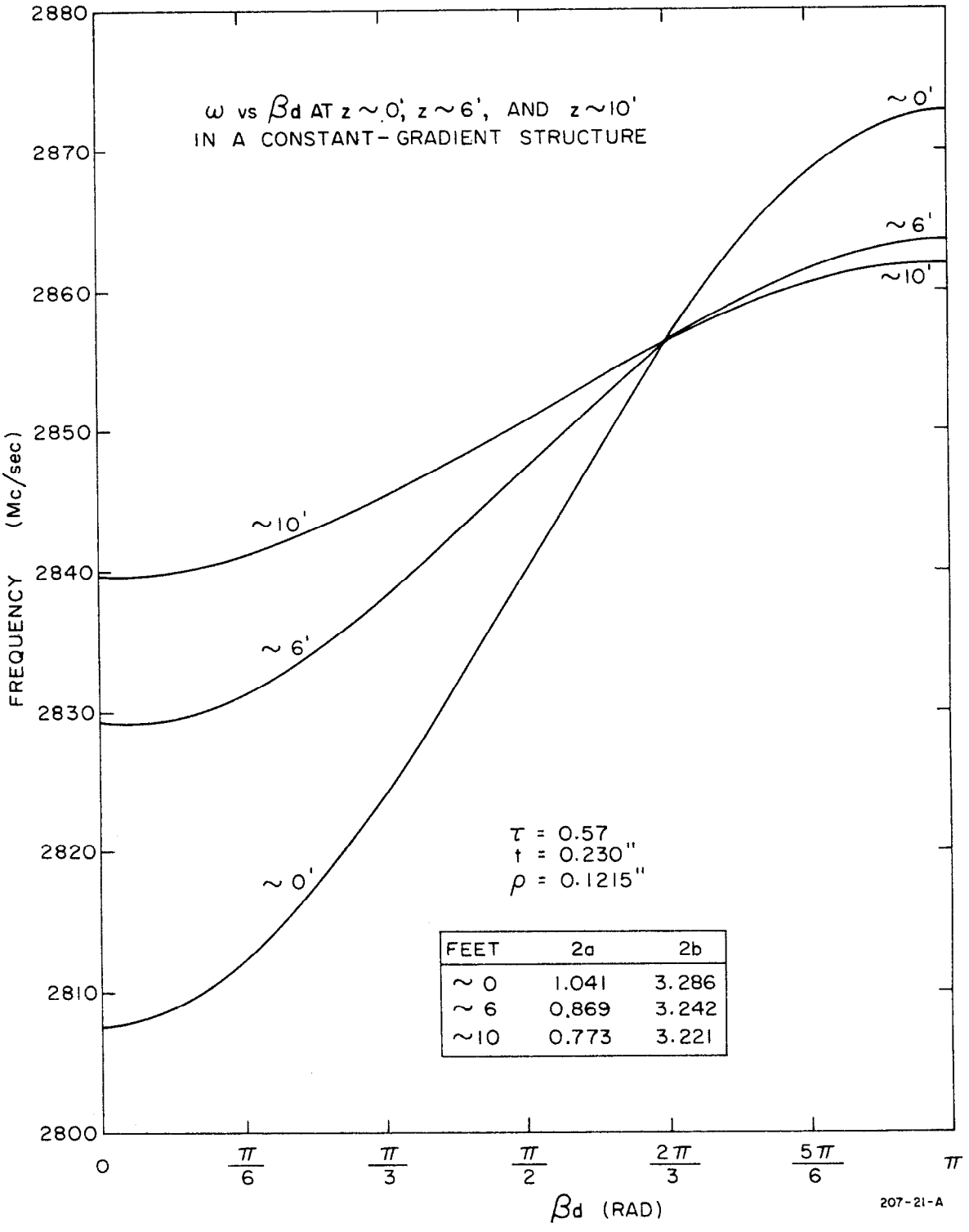
ω vs βd AT z ~ 0', z ~ 6', AND z ~ 10'
IN A CONSTANT-GRADIENT STRUCTURE
FREQUENCY (Mc/sec)
2880
2870
2860
2850
2840
2830
2820
2810
2800
~ 0'
~ 6'
~ 10'
~10'
~ 6'
~ 0'
τ = 0.57
t = 0.230"
ρ = 0.1215"
FEET 2a 2b
~ 0 1.041 3.286
~ 6 0.869 3.242
~10 0.773 3.221
0
π/6
π/3
π/2
2π/3
5π/6
π
βd (RAD)
207-21-A

Figure 21

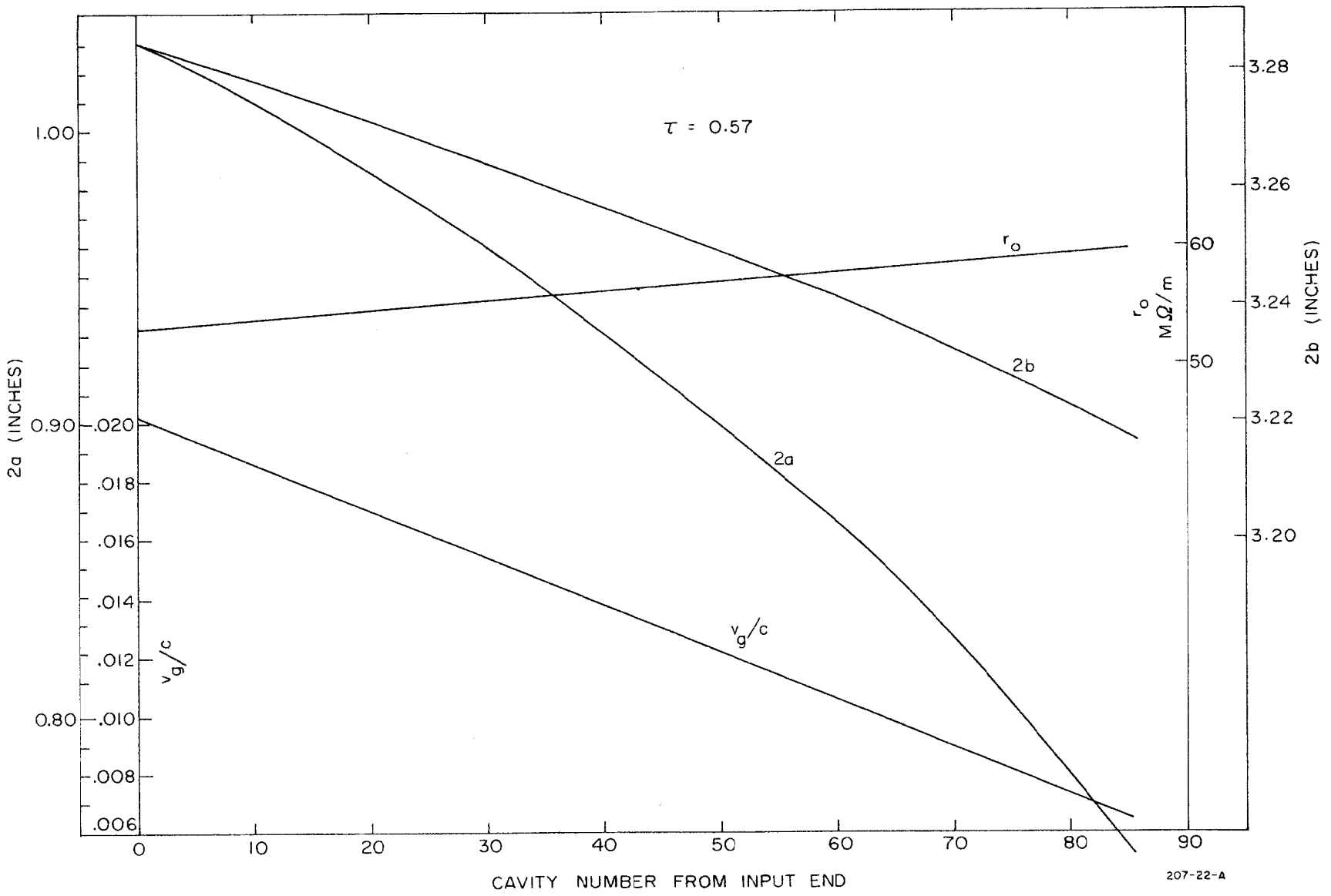
τ = 0.57
1.00
0.90
0.80
2a (INCHES)
.020
.018
.016
.014
.012
.010
.008
.006
v_g/c
r_o
2a
2b
r_o MΩ/m
60
50
3.28
3.26
3.24
3.22
3.20
2b (INCHES)
0
10
20
30
40
50
60
70
80
90
CAVITY NUMBER FROM INPUT END
207-22-A

Figure 22

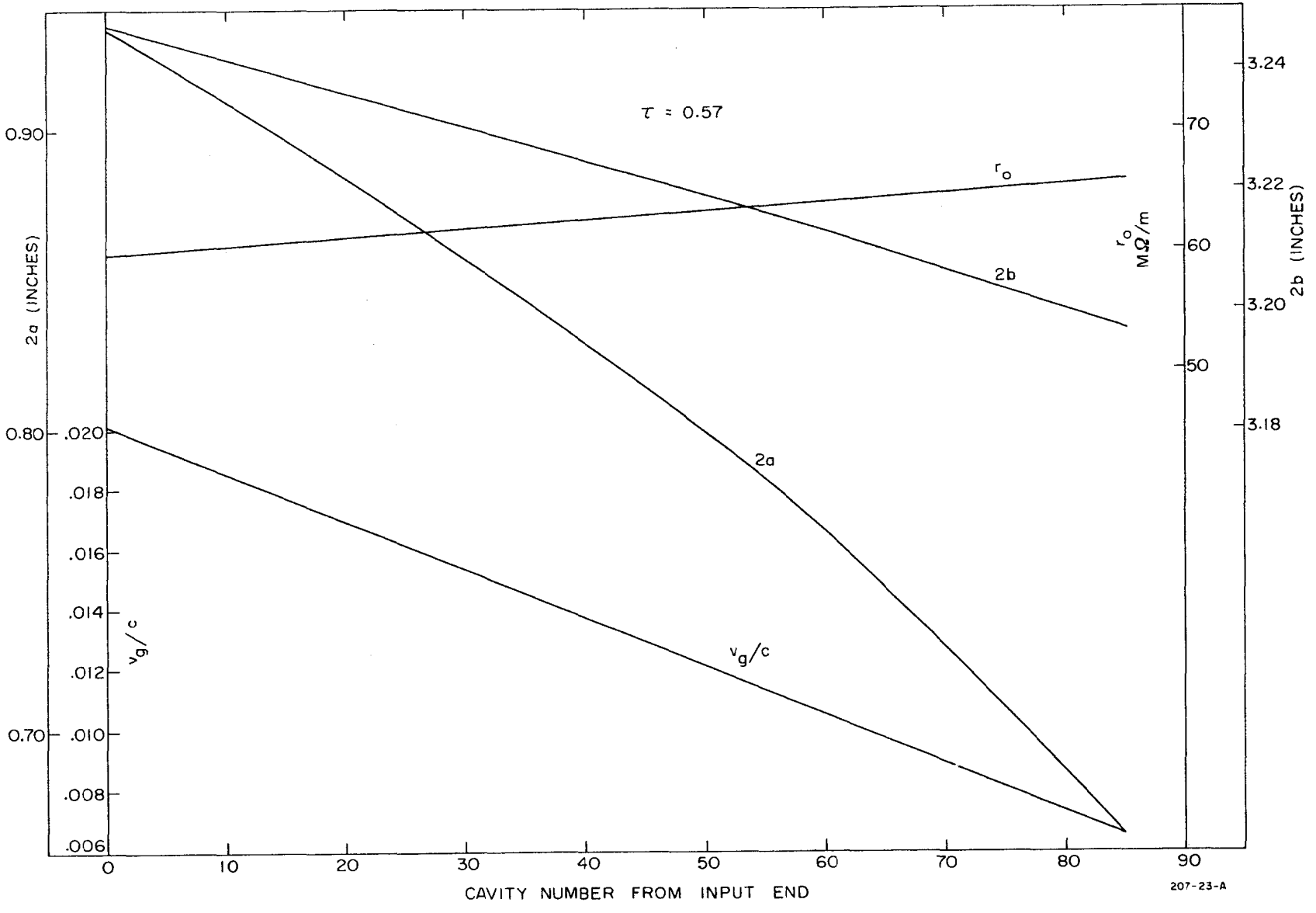
τ = 0.57
r_o
2b
2a
v_g/c
r_o MΩ/m
2a (INCHES)
2b (INCHES)
v_g/c
0.90
0.80
0.70
.020
.018
.016
.014
.012
.010
.008
.006
70
60
50
3.24
3.22
3.20
3.18
0
10
20
30
40
50
60
70
80
90
CAVITY NUMBER FROM INPUT END
207-23-A

Figure 23

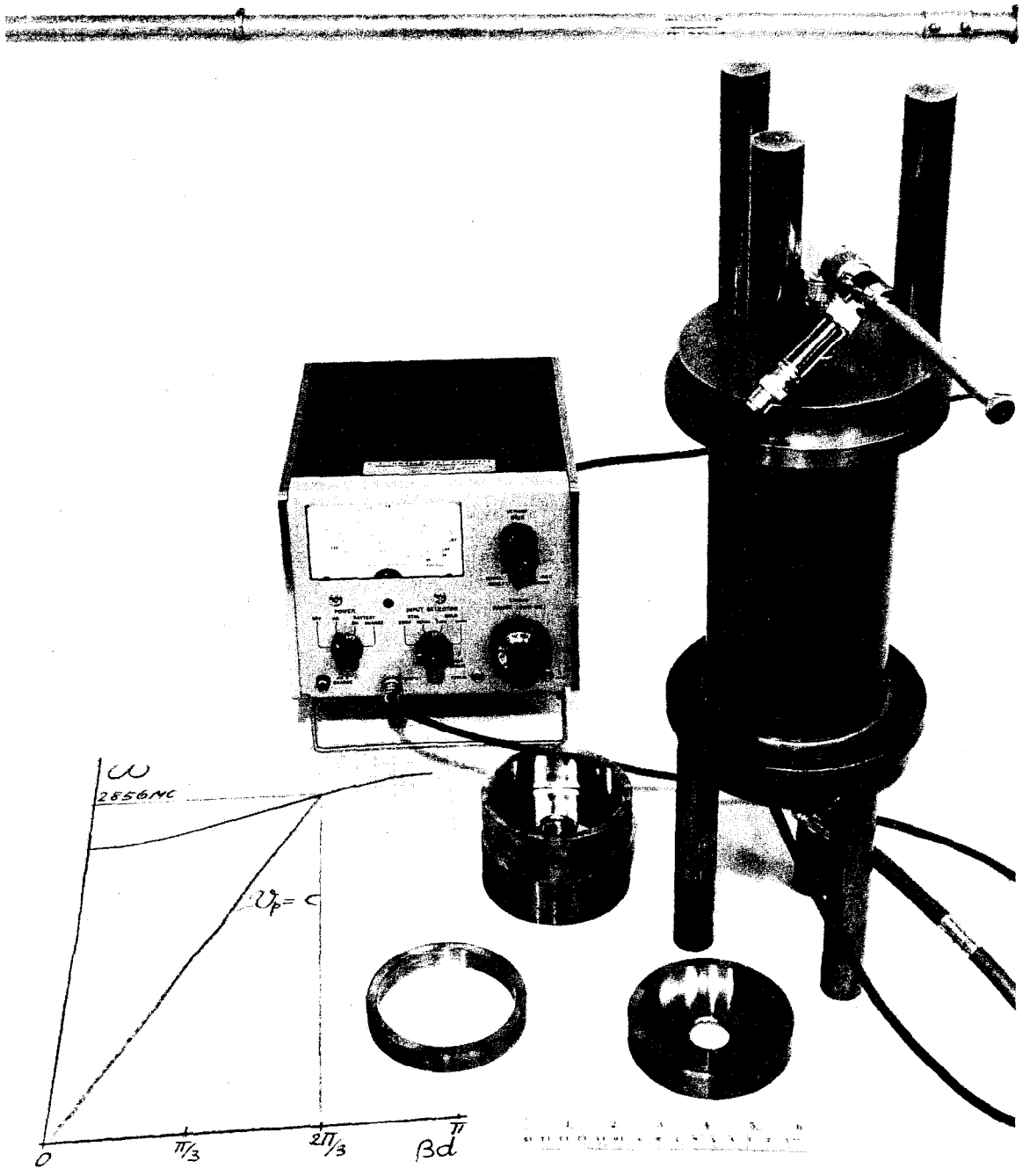

Figure 24

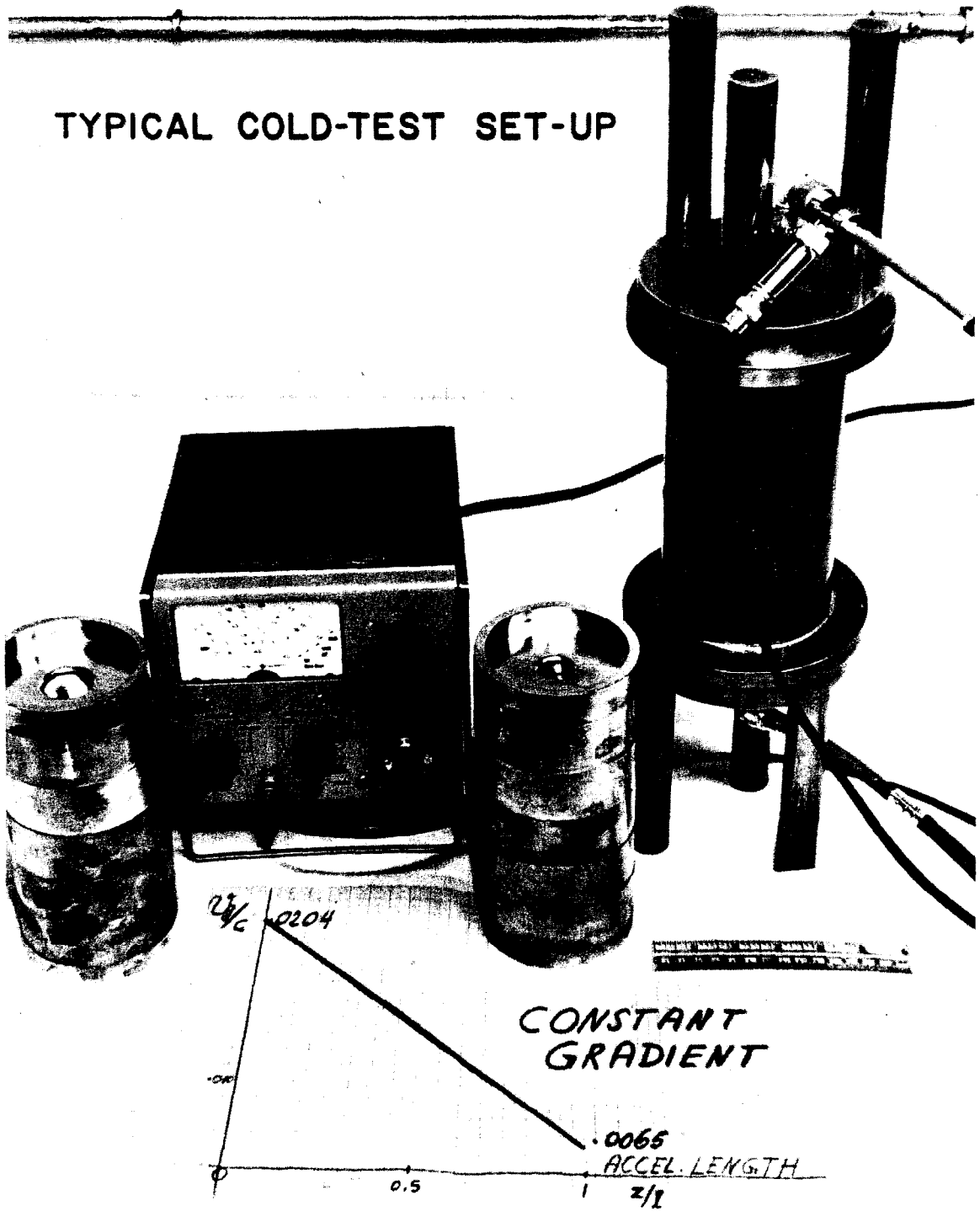
TYPICAL COLD-TEST SET-UP
$V_V/_C$
.0204
CONSTANT
GRADIENT
.0065
ACCEL. LENGTH
0.5
1
z/l

Figure 25

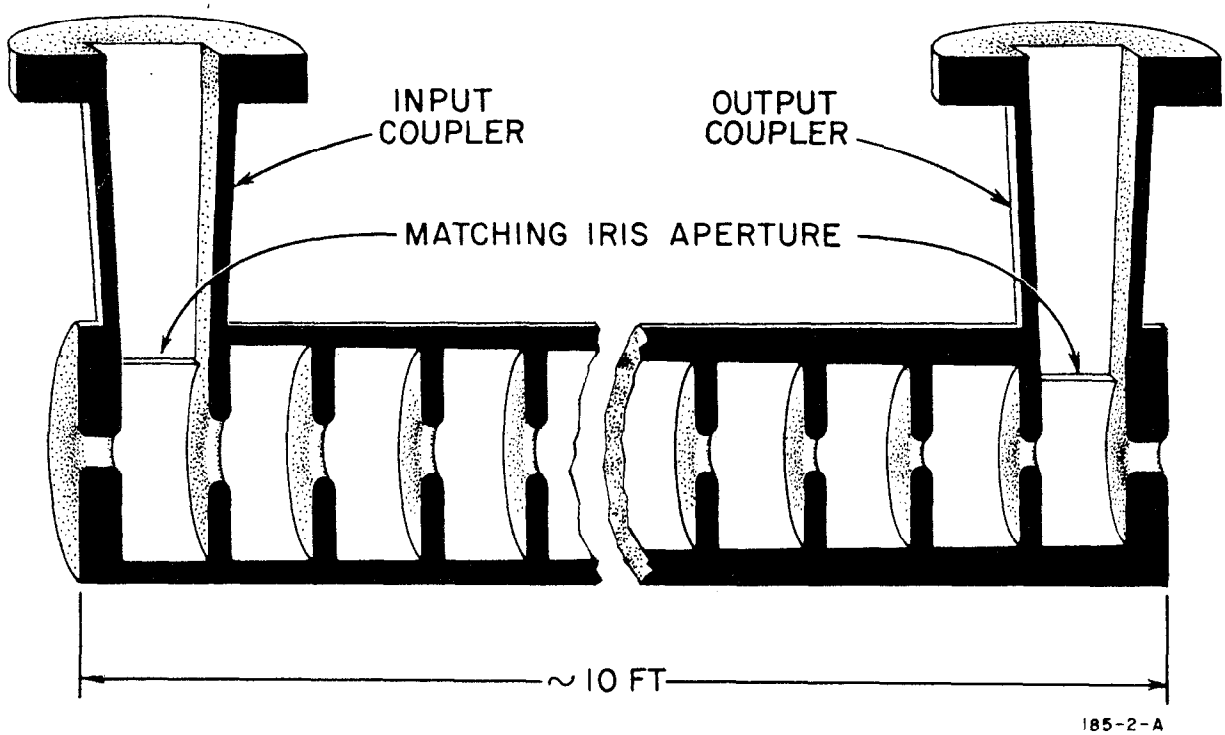

SKETCH OF A TEN-FOOT-LONG CONSTANT-GRADIENT ACCELERATOR STRUCTURE WITH INPUT AND OUTPUT COUPLERS. NOTICE SLIGHT TAPER IN MODULAR DIMENSIONS (DIAMETER OF INNER WALL)

Figure 26

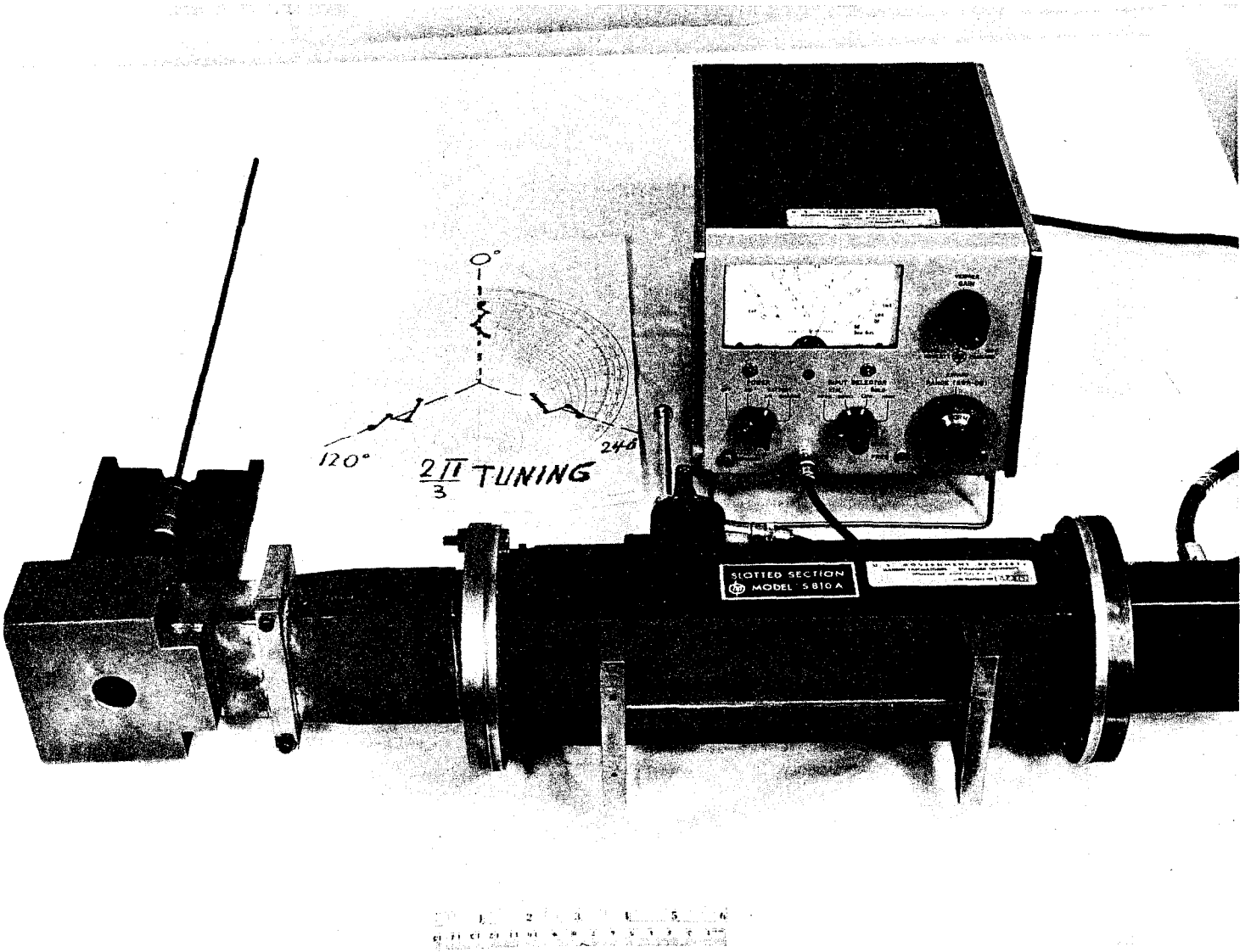

Figure 27

MATCHPOINT (C)

$$\sigma_{sc} = \frac{6.4}{1.9} = \underline{1.84}$$

$$\left(\frac{N-N_0}{\lambda_g}\right)_{sc} = \underline{.444}$$

MATCHPOINT (C) FROM THREE SUCCESSIVE SHORTING PLUNGER DATA.

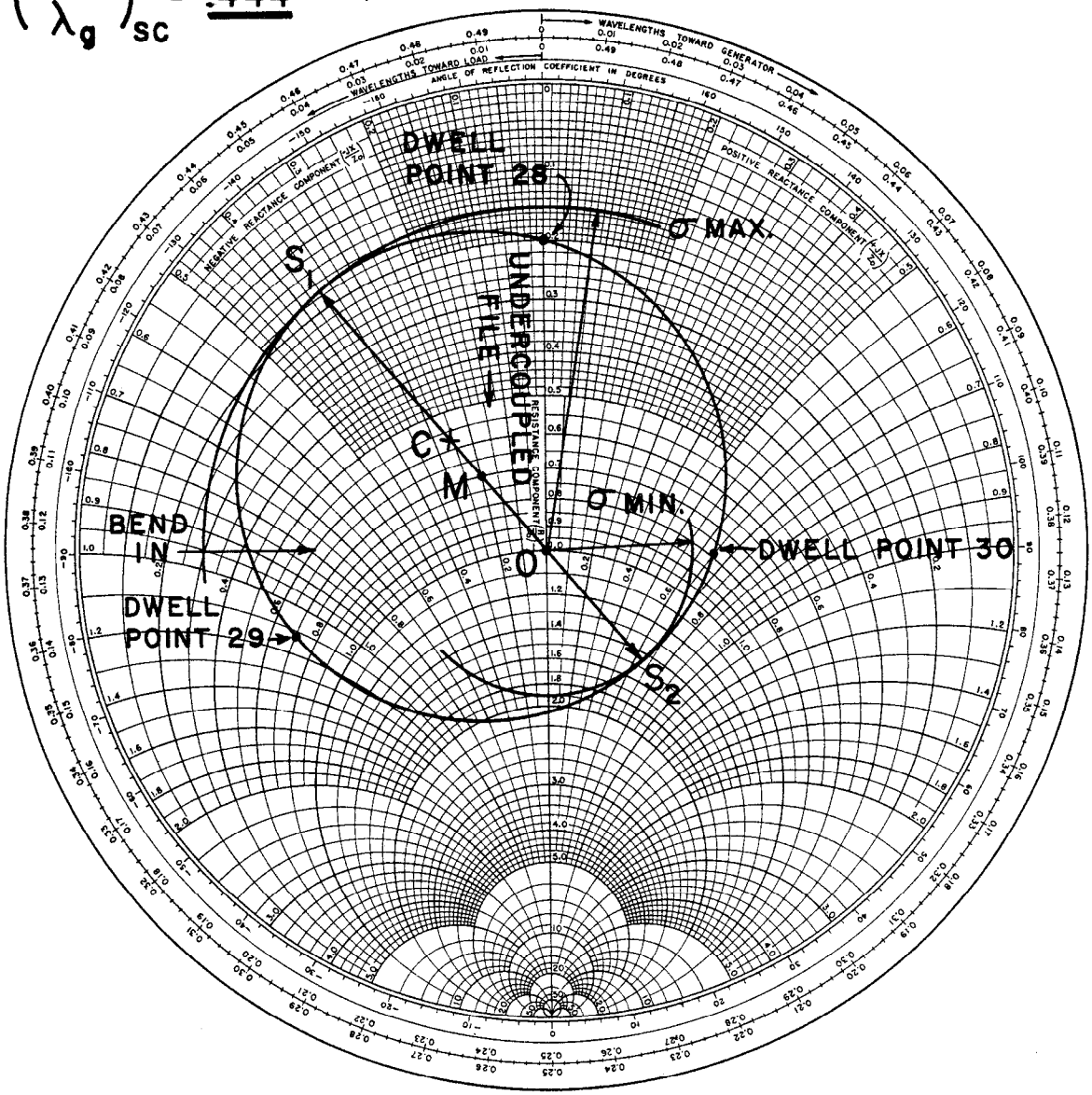

Figure 28

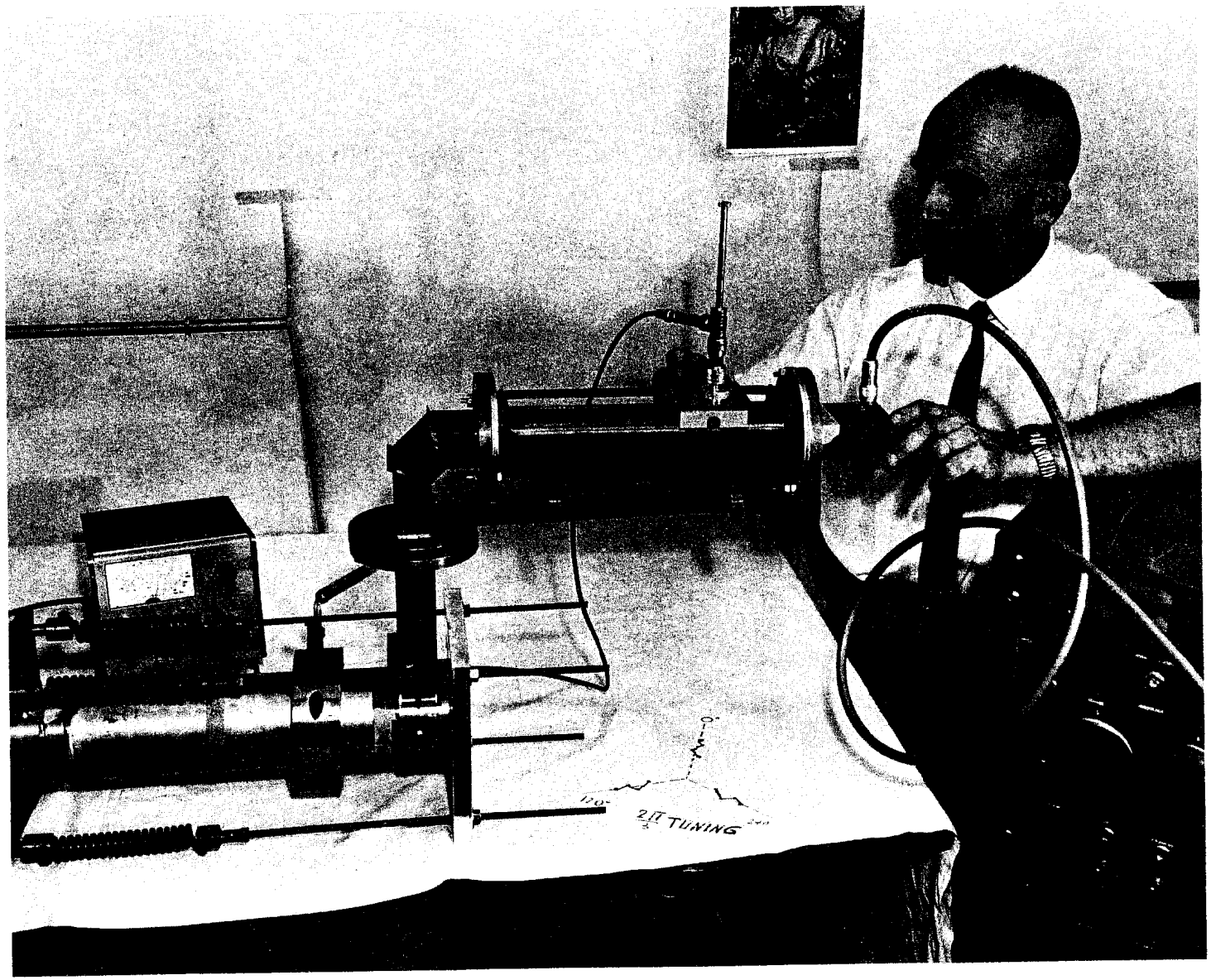

Figure 29

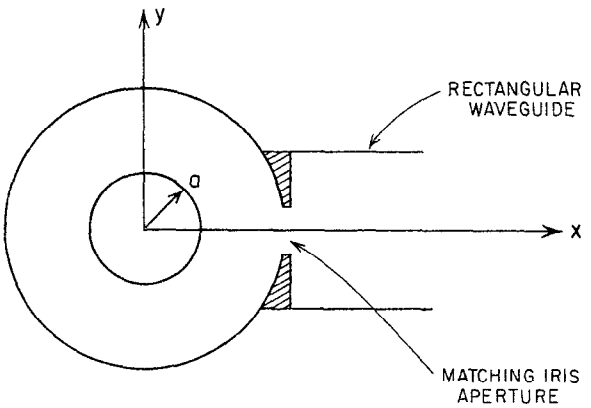

a.) CROSS-SECTION OF COUPLER CAVITY

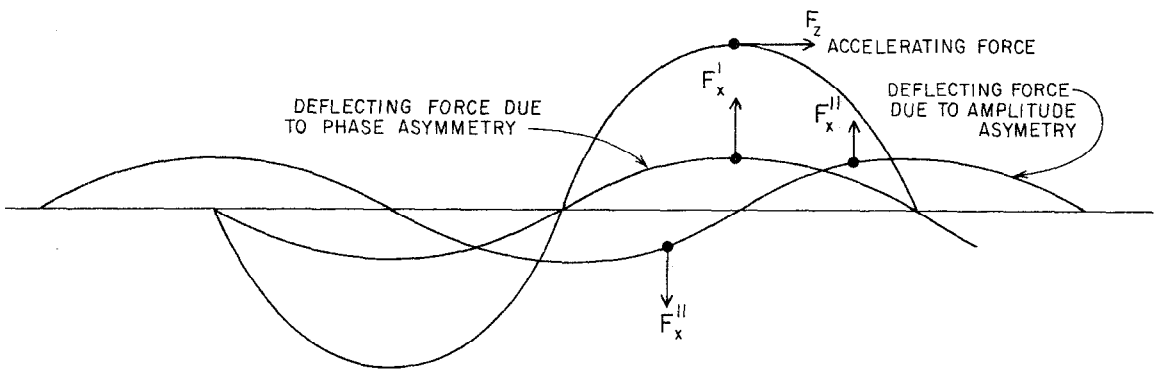

b.) FORCE COMPONENTS DUE TO AMPLITUDE AND PHASE ASSYMMETRY IN THE COUPLER CAVITIES

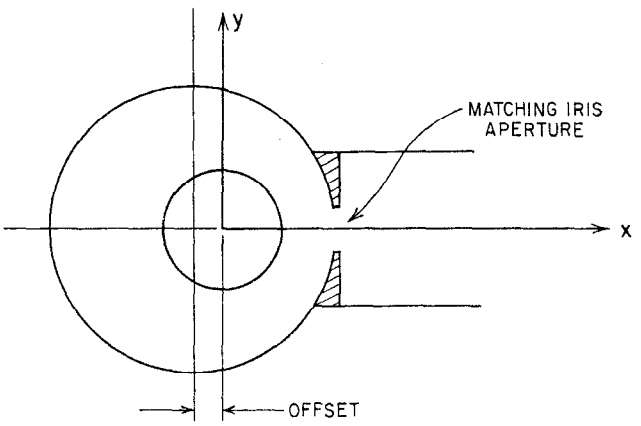

c.) COUPLER OFFSET TO CORRECT AMPLITUDE ASYMMETRY

185-1-A

FIG. 30-THE COUPLER ASYMMETRY PROBLEM

Figure 30

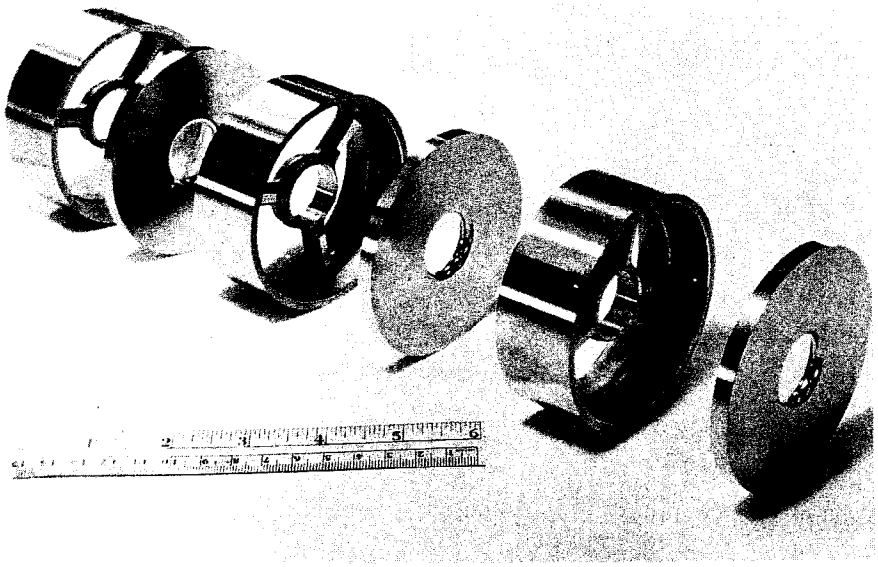

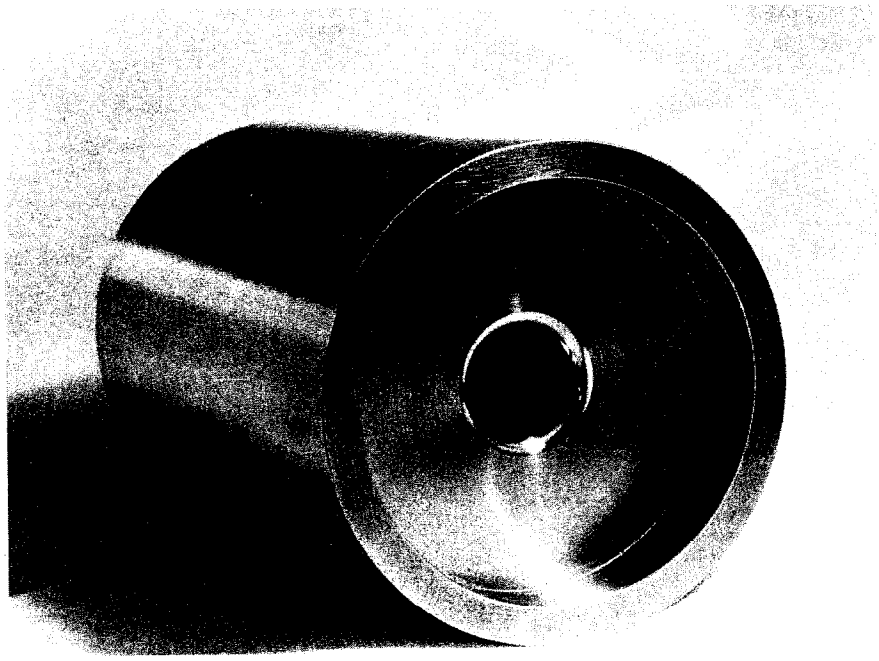

Figure 31

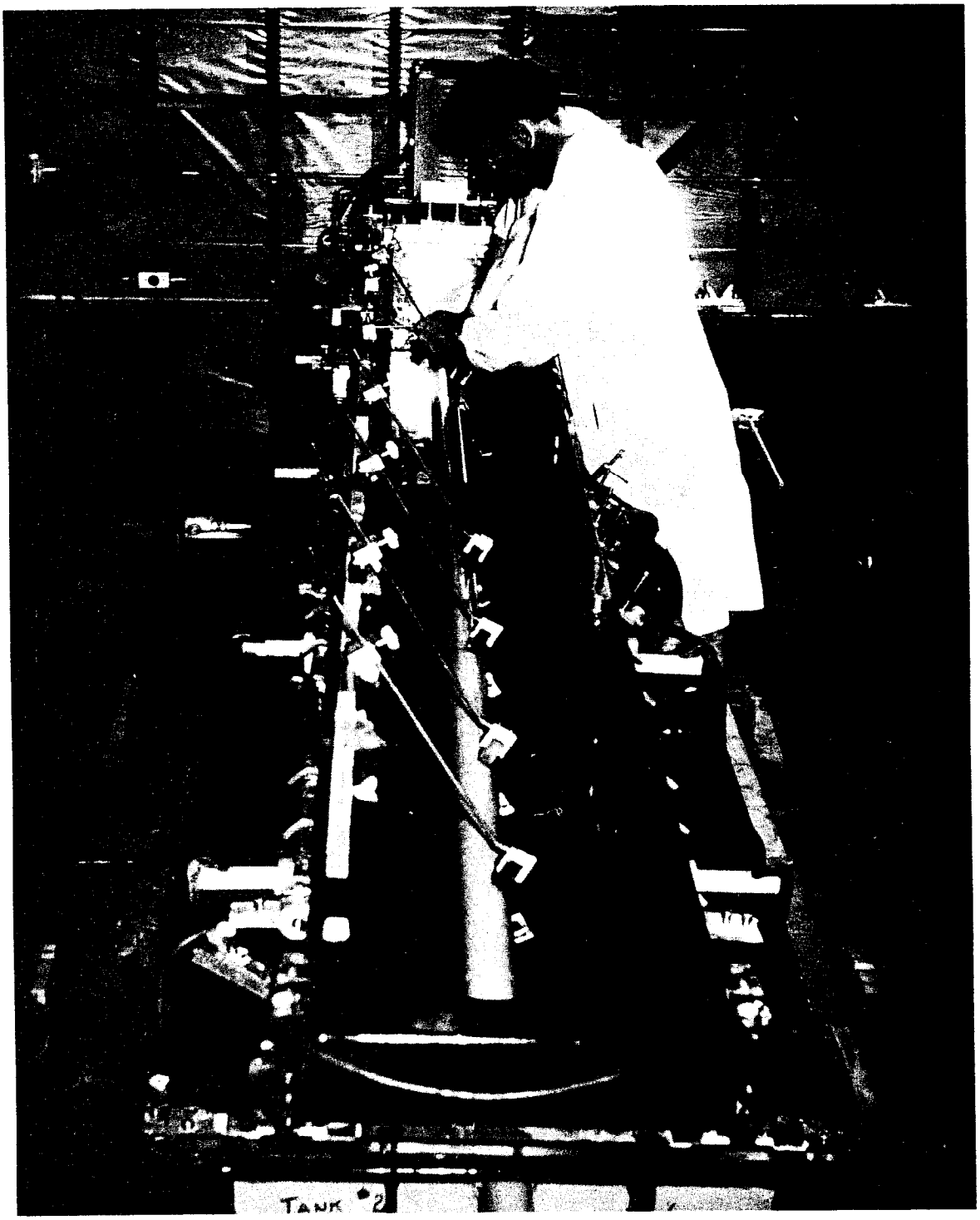

Figure 32

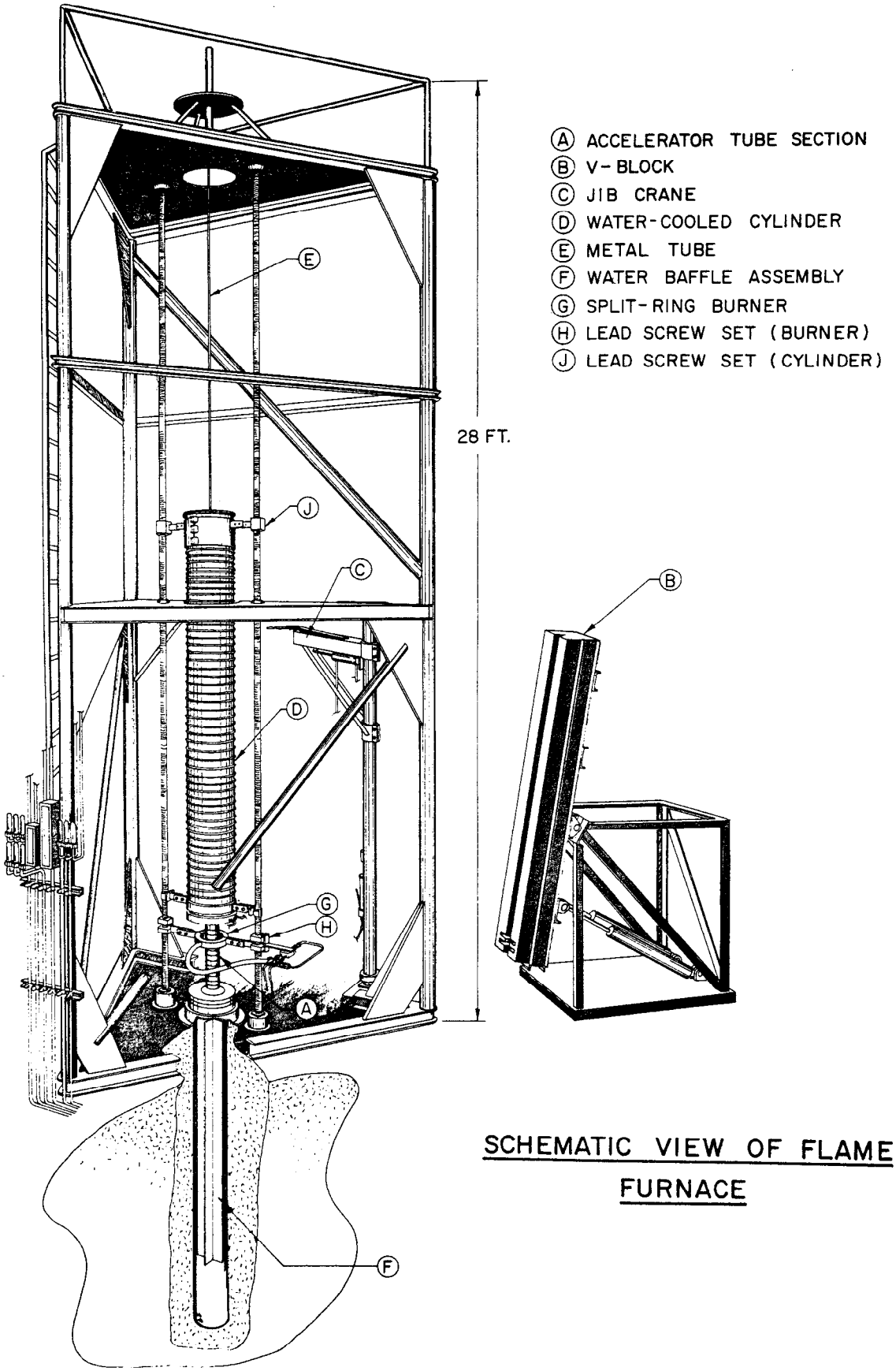

SCHEMATIC VIEW OF FLAME FURNACE

Figure 33

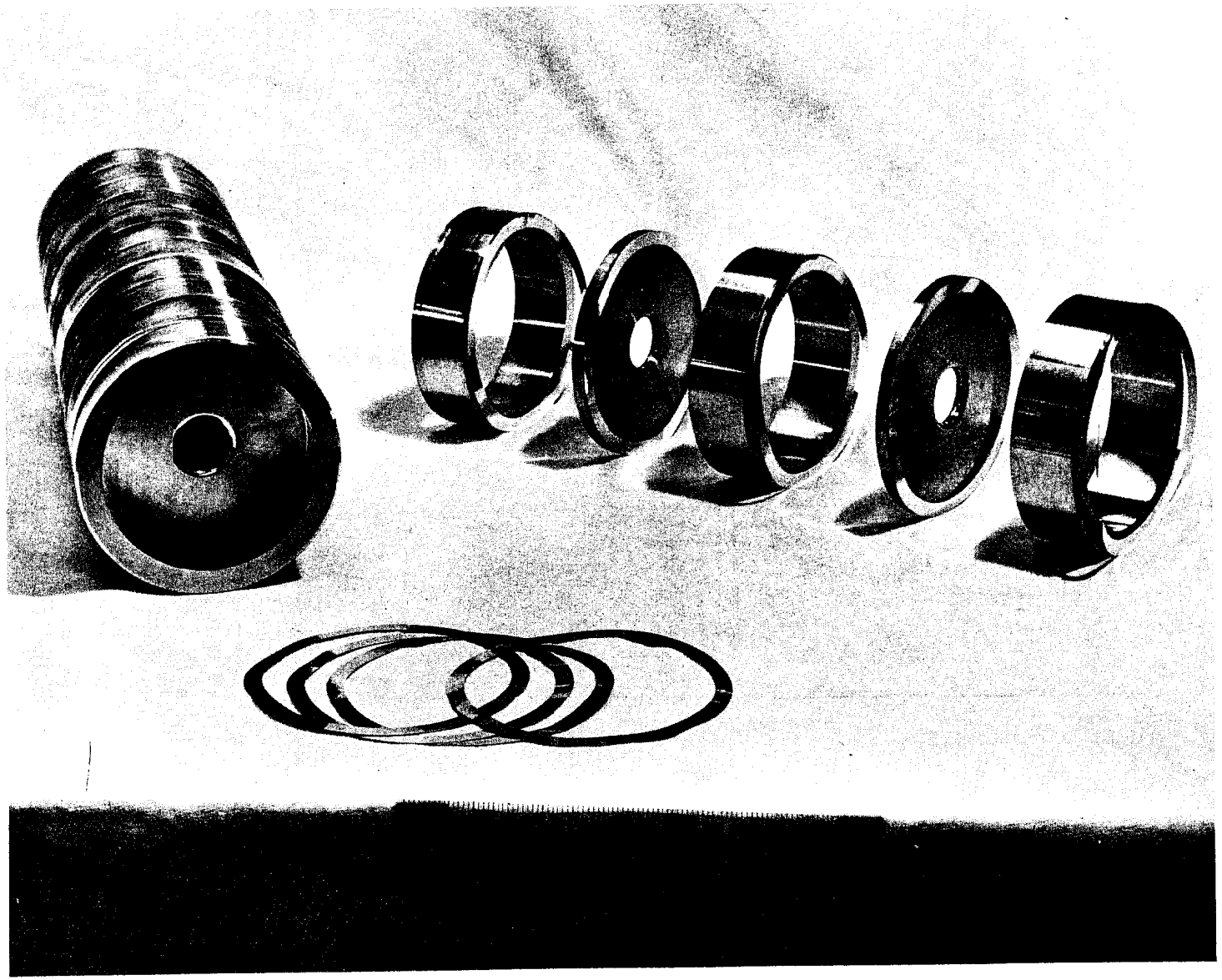

Figure 34

Figure 35

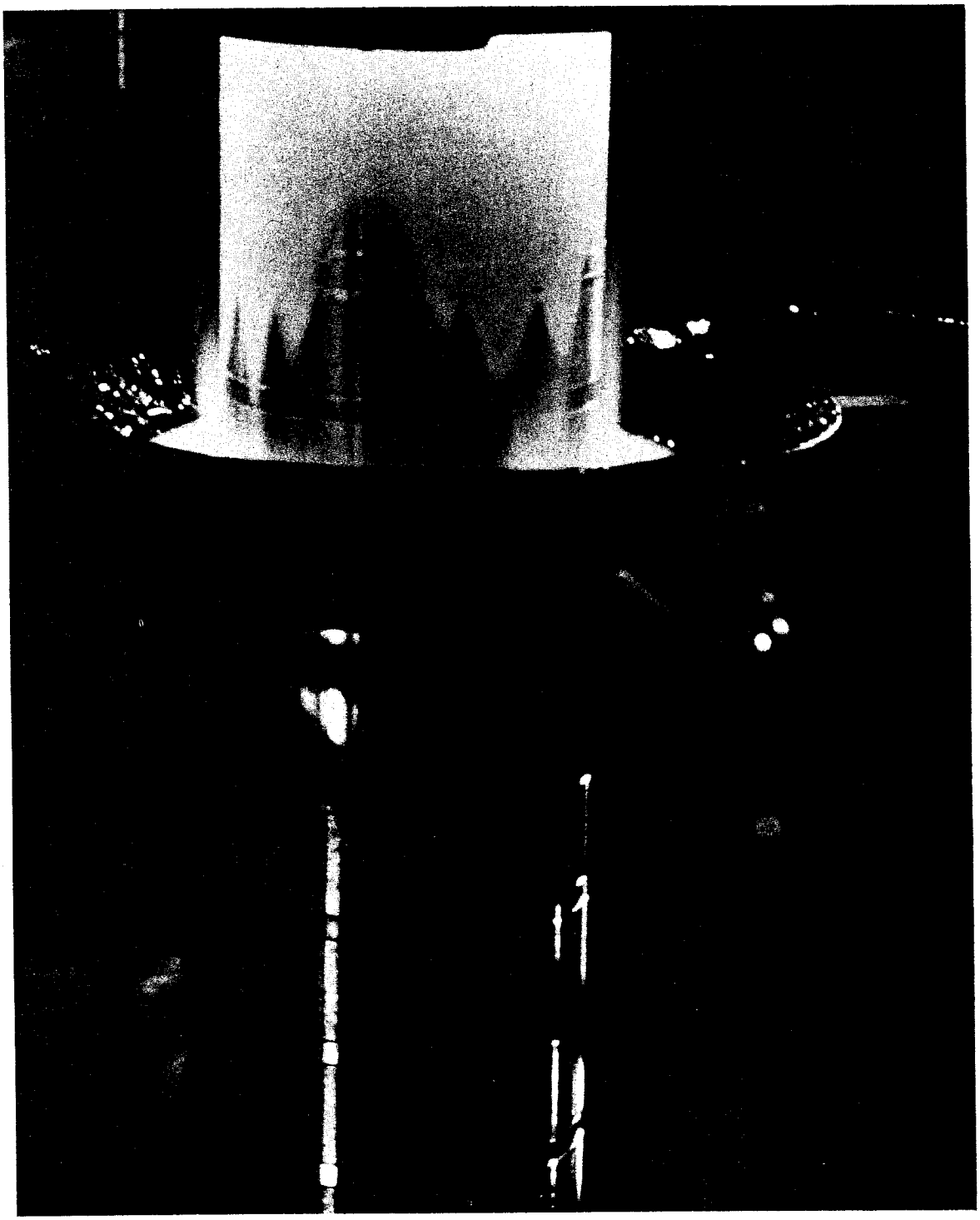

Figure 36

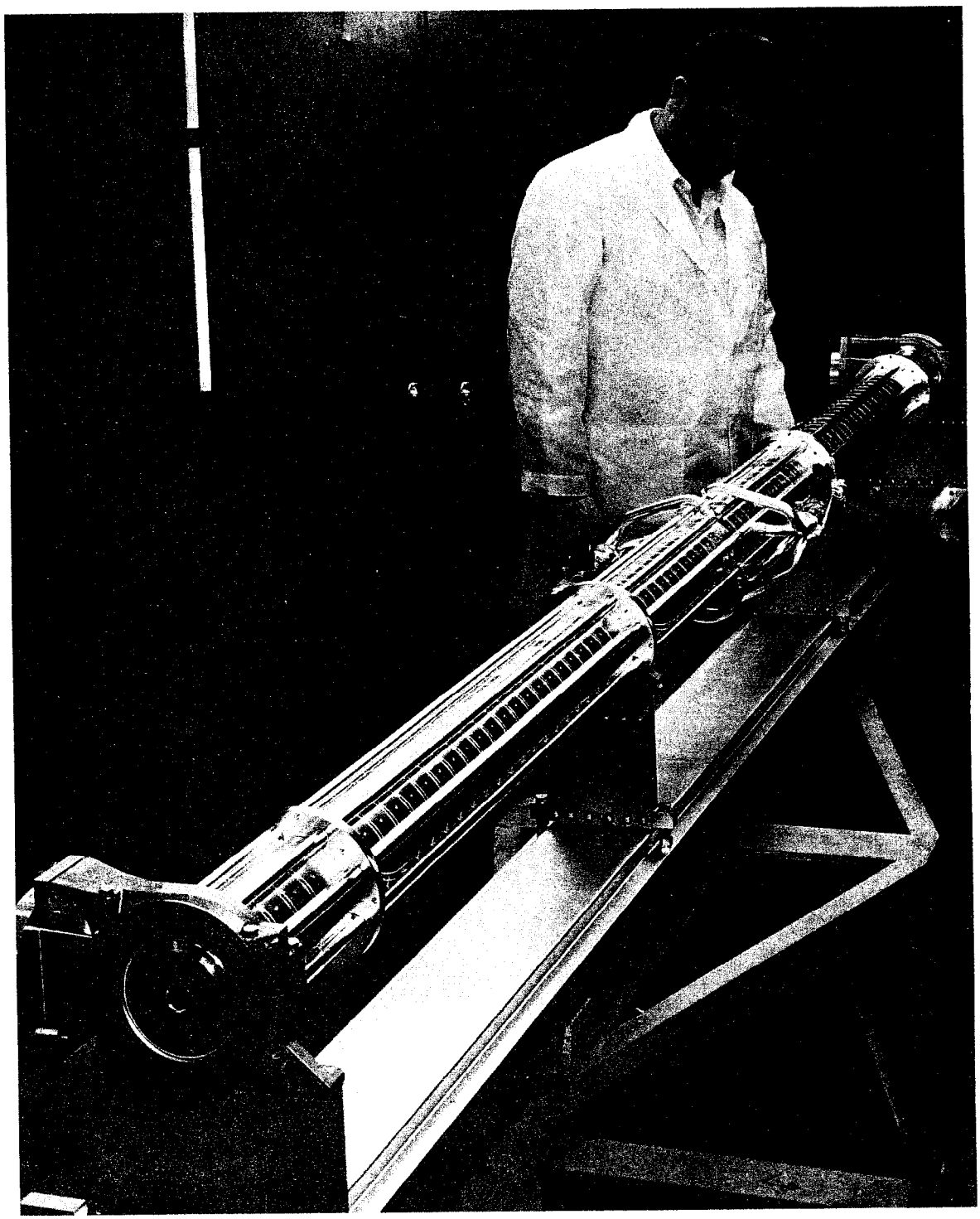

Figure 37

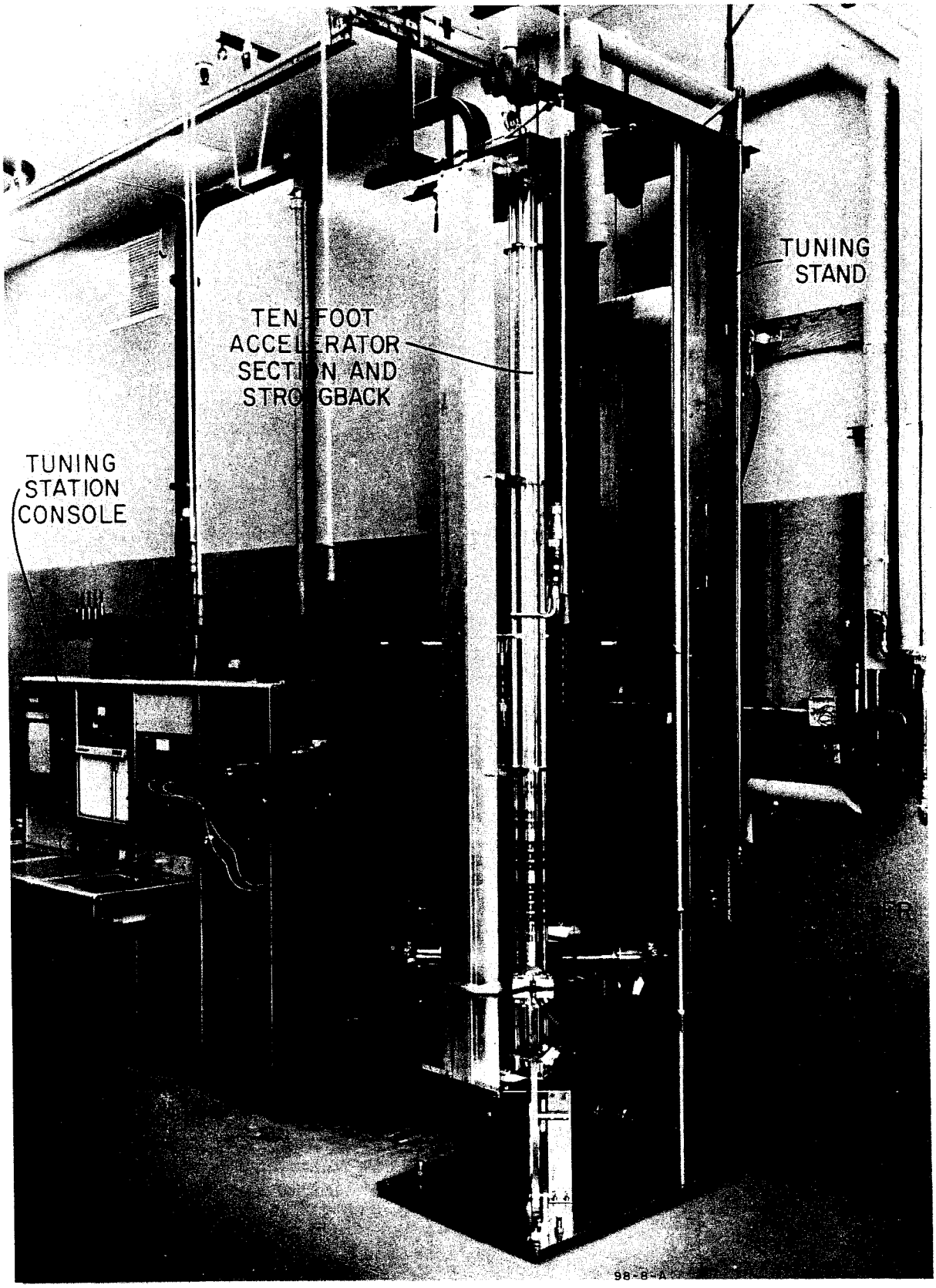
TUNING
STAND
TEN-FOOT
ACCELERATOR
SECTION AND
STRONGBACK
TUNING
STATION
CONSOLE
98-8-A

Figure 38

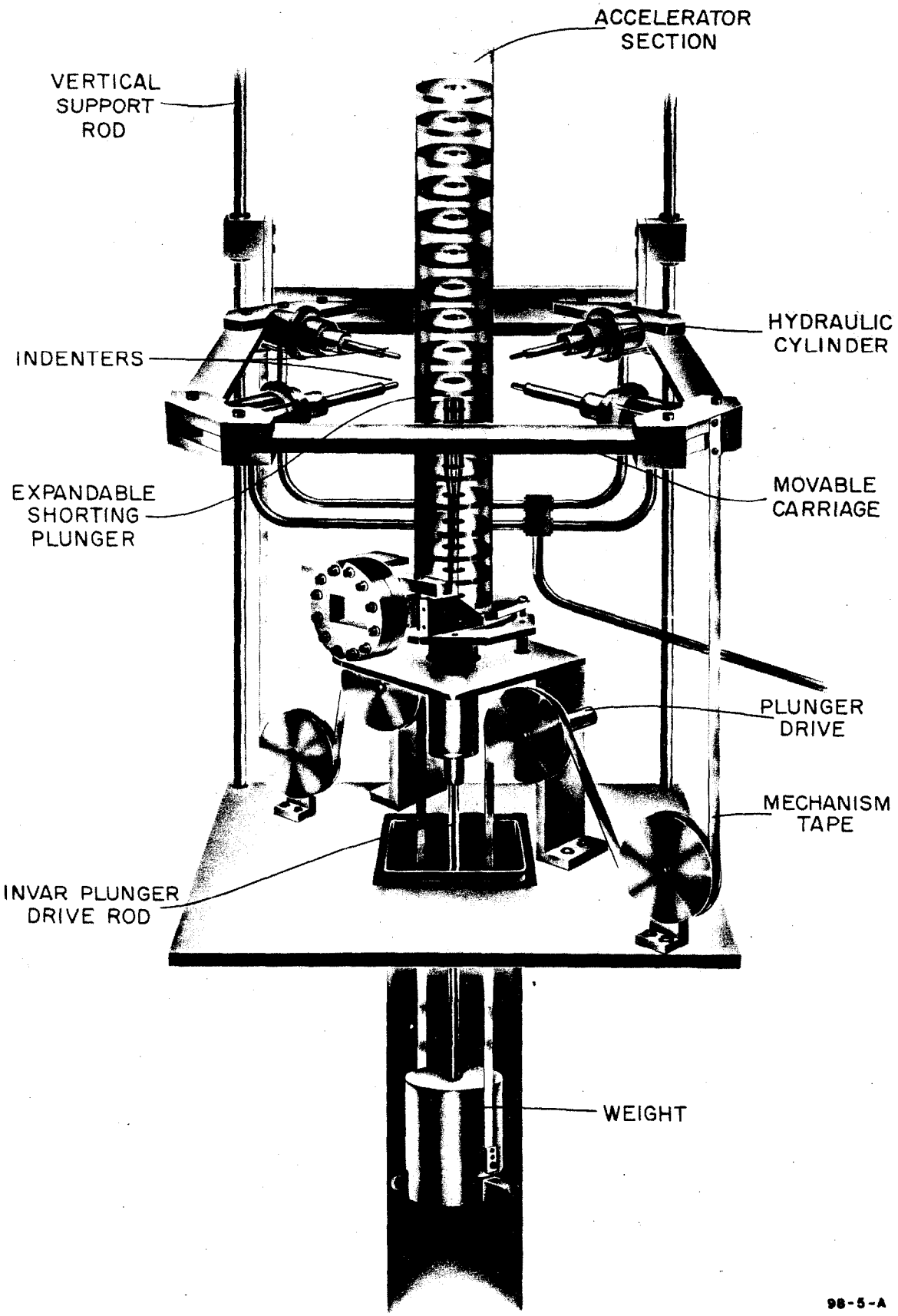
ACCELERATOR SECTION
VERTICAL SUPPORT ROD
HYDRAULIC CYLINDER
INDENTERS
EXPANDABLE SHORTING PLUNGER
MOVABLE CARRIAGE
PLUNGER DRIVE
MECHANISM TAPE
INVAR PLUNGER DRIVE ROD
WEIGHT
98-5-A

Figure 39

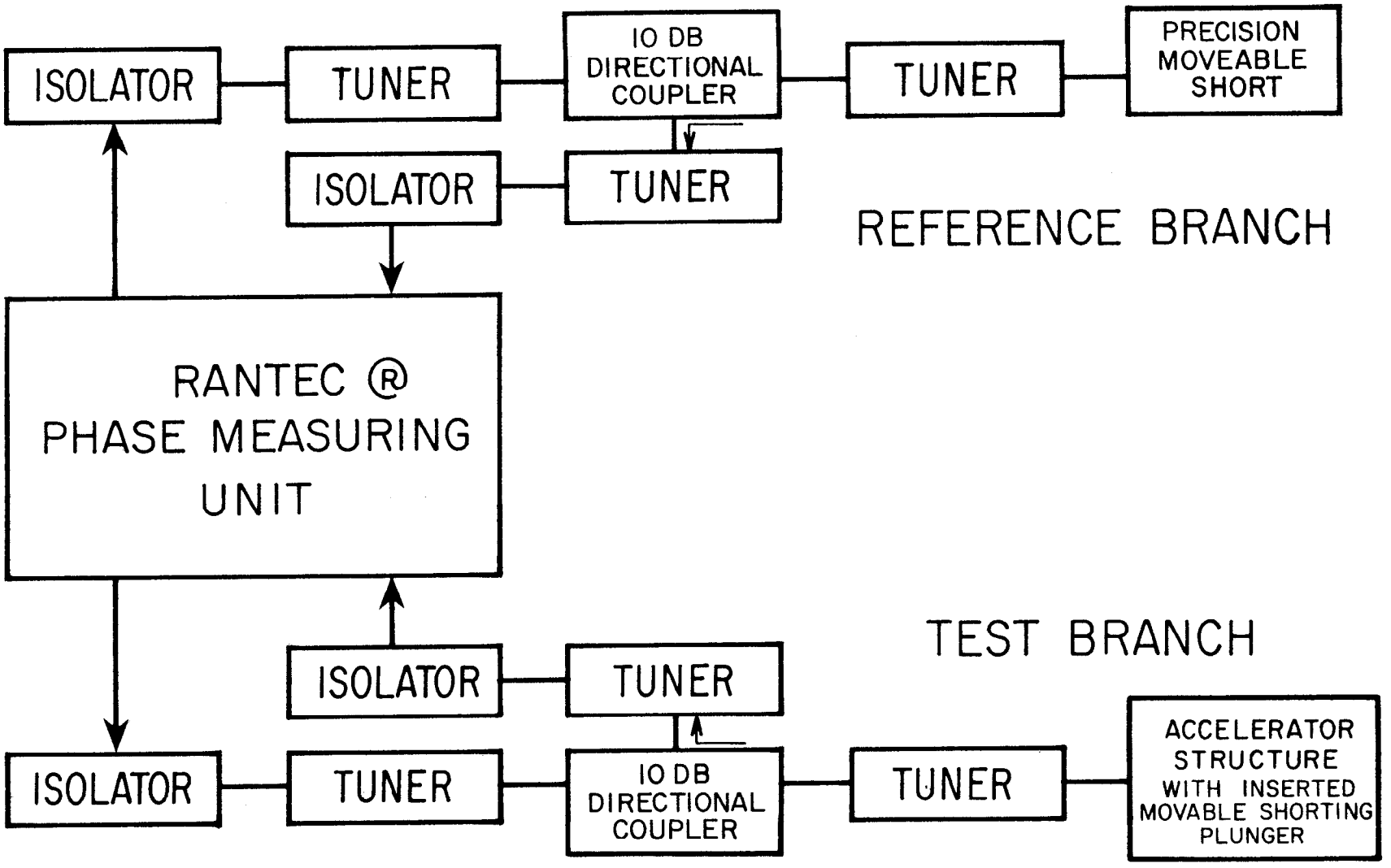

BLOCK DIAGRAM - PHASE MEASURING SYSTEM 89-8-B

Figure 40

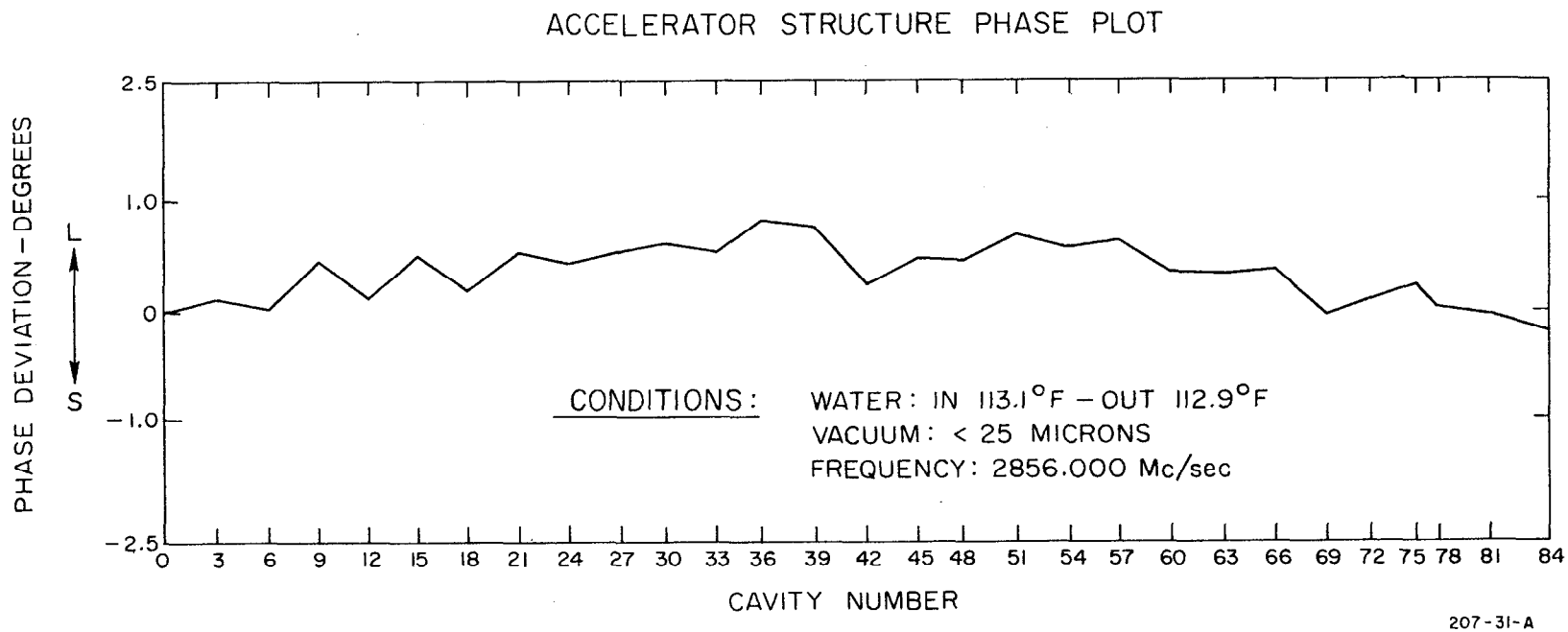
ACCELERATOR STRUCTURE PHASE PLOT
PHASE DEVIATION - DEGREES
2.5
1.0
0
-1.0
-2.5
L
S
CONDITIONS:
WATER: IN 113.1°F - OUT 112.9°F
VACUUM: < 25 MICRONS
FREQUENCY: 2856.000 Mc/sec
0 3 6 9 12 15 18 21 24 27 30 33 36 39 42 45 48 51 54 57 60 63 66 69 72 75 78 81 84
CAVITY NUMBER
207-31-A

Figure 41

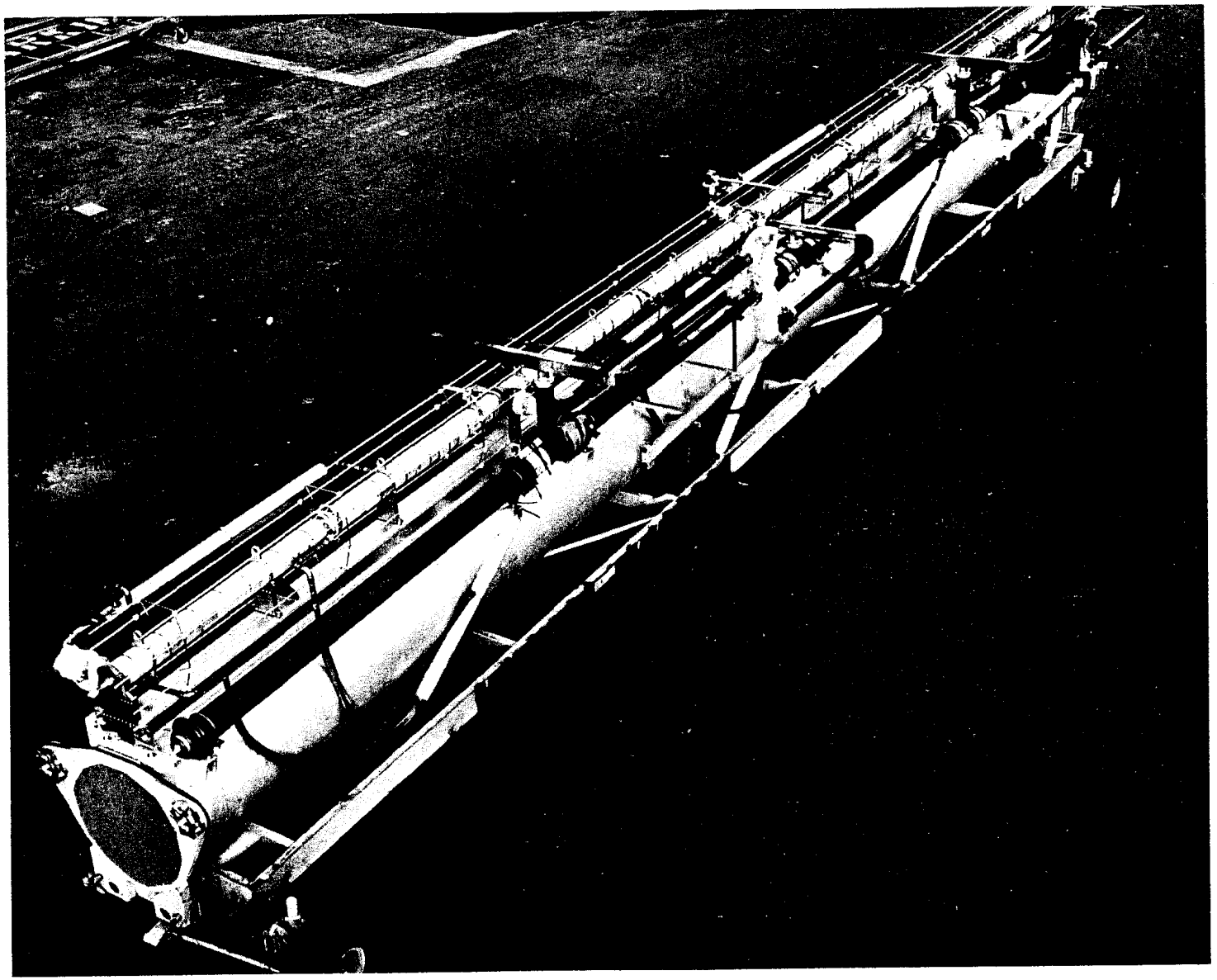

Figure 42

TABLE I

FREQUENCY DEPENDENCE OF PRINCIPAL MACHINE PARAMETERS

Parameter	Frequency Dependence	Frequency Preference		Notes
		High	Low	
Shunt impedance per unit length (r)	$f^{\frac{1}{2}}$	X		a
RF loss factor (Q)	$f^{-\frac{1}{2}}$		X	a
Filling time (t_F)	$f^{-\frac{3}{2}}$	X		a, b
Total rf peak power	$f^{-\frac{1}{2}}$	X		a, b, c
RF feed interval (ℓ)	$f^{-\frac{3}{2}}$		X	a, b
Number of rf feeds	$f^{\frac{3}{2}}$		X	a, b, d
RF peak power per feed	f^{-2}	X		a, b, c
RF energy stored in accelerator	f^{-2}	X		a, b, c
Beam loading (-dV/di)	$f^{\frac{1}{2}}$		X	a, b, d
Peak beam current at maximum conversion efficiency	$f^{-\frac{1}{2}}$		X	a, b, c, f
Diameter of beam aperture	f^{-1}		X	a
Maximum rf power available from single source	f^{-2}		X	e
Maximum permissible electric field strength	$f^{\frac{1}{2}}$	X		g
Relative frequency and dimensional tolerances	$f^{\frac{1}{2}}$	X		a, b
Absolute wavelength and dimensional tolerances	$f^{-\frac{1}{2}}$		X	a, b
Power dissipation capability of accelerator structure	f^{-1}		X	a, b, d

TABLE I - (Continued)

Notes:

a. For direct scaling of modular dimensions of accelerator structure.

b. For same rf attenuation in accelerator section between feeds.

c. For fixed electron energy and total length.

d. For fixed total length.

e. When limited by cathode emission.

f. When limited by beam loading.

g. Approximate; empirical.

TABLE II

DESIGN PARAMETERS OF 10 BEV ACCELERATOR AT 3 FREQUENCIES[a]

	Frequency		
	(L-Band) 1000 Mc/sec	(S-Band) 3000 Mc/sec	(X-Band) 9000 Mc/sec
Shunt impedance, r, megohms per meter	31	53	92
RF loss factor (Q)	2.25×10^4	1.3×10^4	0.75×10^4
Filling time, t_F (microseconds)	4.31	0.83	0.16
Total rf peak power (megawatts)	2304	1330	768
RF feed interval (feet)	52	10	1.92
Number of rf feeds	185	960	4988
RF peak power, (megawatts) per feed	12.5	1.39	0.15
RF energy (joules) stored in accelerator	5337	593	66
RF energy (joules) required for 1.67 μsec electron beam pulse length	13,778	3325	1405
Total average rf power (megawatts) at 360 pulses/sec	4.96	1.20	0.51
Beam loading (-dV/di), (BeV/ampere)	20.5	35.5	61.5
Peak beam current (milliamperes) at maximum conversion efficiency	272.1	157.1	90.7
Minimum diameter (inches) of beam aperture	2.292	0.764	0.255
Maximum rf peak power (megawatts) available from single source	216	24	2.7

TABLE II - (Continued)

	Frequency		
	(L-Band) 1000 Mc/sec	(S-Band) 3000 Mc/sec	(X-Band) 9000 Mc/sec
Maximum permissible electric field strength[b] (kilovolts/cm)	133	230	398
Maximum expanded beam energy[c] (BeV)	38.4	66.5	115.0
Relative frequency and dimensional tolerances[d]	1.11×10^{-5}	1.93×10^{-5}	3.34×10^{-5}
Absolute frequency and dimensional tolerances[d]	11 kc/sec; 0.11 mils	58 kc/sec; 0.06 mils	301 kc/sec; 0.04 mils
Average power dissipated per unit area of accelerator surface[e] (watts/cm^2)	0.20	0.14	0.18
Average temperature difference (°C) across accelerator wall[f]	0.14	0.03	0.01

a. Assumptions: $2\pi/3$ mode in constant-gradient structure; $\tau = 0.57$ nepers (rf attenuation); L = 10,000 feet (94.8% effective); 10% power loss in waveguides; 10% beam loading; direct scaling of modular dimensions.

b. Based on maximum gradient obtained to date at S-band; values for other frequencies based on scaling as $f^{\frac{1}{2}}$.

c. As limited by maximum permissible field strength.

d. For one percent loss in beam energy.

e. Based on 360 pulses per second and 1.67-μsec electron beam pulse length.

f. Based on copper wall 3, 1, and 1/3 cm thick at L, S, and X-bands respectively.

TABLE III

COMPARISON OF CONSTANT-GRADIENT AND CONSTANT-IMPEDANCE ACCELERATOR STRUCTURES

Characteristic	Constant-Gradient	Constant-Impedance	Ratio $\frac{\text{c.g.}}{\text{c.i.}}$
$\frac{E_o \ell}{V_o}$ $\left(\frac{\text{Peak elec. field}}{\text{Aver. elec. field}}\right)$	1.00	1.31	0.76
$\frac{(dP/dz)_{z=o}}{(dP/dz)_{z=\ell}}$	1.00	3.13	0.32
V_o (no-load energy)	11.17 BeV	11.02 BeV	1.01
$-dV/di$	35.53 BeV/amp	36.41 BeV/amp	0.98
V (at i = 25 mamps)	10.28 BeV	10.11 BeV	1.02
η_{max} $\left(\begin{matrix}\text{max beam-conversion} \\ \text{efficiency}\end{matrix}\right)$	0.73	0.70	1.05
$i_{\eta_{max}}$	157.1 ma	151.3 ma	1.04
v_g/c $\left(\begin{matrix}\text{normalized} \\ \text{group velocity}\end{matrix}\right)$	.0204 → .0065	0.0121	1.68 → 0.54
t_F (filling time)	0.83 μsec	0.83 μsec	1.00
U (stored energy)	593 joules	593 joules	1.00
$\Delta_{z=\ell}$ $\left(\begin{matrix}\text{phase shift for} \\ \delta f = 0.1 \text{ Mc/sec}\end{matrix}\right)$	0.52 rad	0.52 rad	1.00
$\delta V_o/V_o$ (for δf = 0.1 Mc/sec)	0.033	0.039	0.85

TABLE III - (Continued)

Assumed parameters: $\tau = 0.57$

P_{oT} = 1330 Mw (90% of which enters accelerator)

L = 10,000 ft (94.8% effective)

Number of sections = 960

f = 2856 Mc/sec

r = 53 megohms/meter

Q = 13,000

TABLE IV

CALCULATED PERFORMANCE OF CONSTANT-GRADIENT ACCELERATOR AT VARIOUS VALUES OF ATTENUATION PARAMETER τ

	τ (nepers)				
	0.4	0.57	0.8	1.0	1.2
(V_{To}) unloaded energy (BeV)	10.05	11.17	12.10	12.59	12.91
(- dV/di) beam loading derivative (BeV/amp)	26.59	35.53	45.58	52.61	58.24
(V_T) energy at 25 ma beam current (BeV)	9.38	10.28	10.96	11.28	11.46
$(\Delta V)_t$ transient energy spread (in BeV) between i=0 and i=25 ma	0.67	0.89	1.14	1.31	1.45
$\left(i_{\eta_{max}}\right)$ beam current at max conversion efficiency (ma)	188.9	157.1	132.7	119.7	110.8
$(\Delta V)_e$ energy loss in idle 10-ft section at i=25 ma (MeV)	0.66	0.88	1.13	1.30	1.44
(v_g/c) normalized group velocity[a]	.0252 → .0113	.0204 → .0065	.0174 → .0035	.0160 → .0022	.0152 → .0014
(t_F) filling time (μsec)	0.58	0.83	1.16	1.45	1.74
(- $\delta V/V$) energy loss for δf = 0.1 Mc/sec	0.018	0.033	0.056	0.077	0.098

TABLE IV -(Continued)

Assumptions: $2\pi/3$ mode, constant-gradient design

P_{oT} = 1330 Mw (90% of which enters accelerator)

L = 10,000 ft (94.8% effective)

Number of sections = 960

f = 2856 Mc/sec

r = 53 megohms/meter

Q = 13,000

---

[a] The group velocity in each 10-ft accelerator section varies linearly between the limits given in each column.

TABLE V

Characteristics of Stanford Constant-Impedance Structures

Parameters	Mark III Accelerator (1952)	Mark IV Accelerator (1960)
Operating mode	$\pi/2$	$2\pi/3$
Length (feet)	10	10
Waveguide inside diameter 2b (inches)	3.247	3.247
Disk hole diameter 2a (inches)	0.8225	0.890
Disk thickness t (inches)	0.230	0.230
Periodic length d (inches)	1.0335	1.378
Disk radius edge ρ (inches)	0.1215	0.1215
Matching iris aperture (inches)	1.042	1.014
Frequency (Mc/sec)	2856	2856
Group velocity v_g/c	0.0100	0.0122
Shunt impedance r (megohms/meter) corrected for fundamental space-harmonic amplitude	47	53
Q	10,000	13,200
Attenuation τ (nepers)	0.90	0.57